DEVELOPMENT OF A NUMERICAL PROCEDURE FOR MIXED MODE K-SOLUTIONS AND FATIGUE CRACK GROWTH IN FCC SINGLE CRYSTAL SUPERALLOYS

By

SRIKANT RANJAN

A DISSERTATION PRESENTED TO THE GRADUATE SCHOOL
OF THE UNIVERSITY OF FLORIDA IN PARTIAL FULFILLMENT
OF THE REQUIREMENTS FOR THE DEGREE OF
DOCTOR OF PHILOSOPHY

UNIVERSITY OF FLORIDA

2005

To

My parents Prof. Yamuna Prasad and Mrs. Maya Devi for always loving me.

ACKNOWLEDGMENTS

This dissertation is the result of 5 years of work whereby I have been accompanied and supported by many people. It is a pleasant aspect that I have now the opportunity to express my gratitude to all of them.

The first person I would like to thank is my supervisor, Dr. Nagaraj Arakere. I have been under his supervision since 2000 when I moved to the University of Florida. His enthusiasm and integral view on research and his mission for providing "only high-quality work and not less," has made a deep impression on me. I owe him lots of gratitude for having me shown this way of research.

I would also like to thank the other members of my PhD committee who took the effort in reading and providing me with valuable comments on earlier versions of this thesis: Dr. Ashok Kumar, Dr. Bhavani Sankar, Dr. Fereshteh Ebrahimi and Dr. John Ziegert. I thank them all.

My colleagues in the Fatigue and Tribology (FAT) LabErik Knudsen, Jeff Leismer, Shadab Siddiqui and Tae-Joong YUall gave me the feeling of being at home at work. The friendly ambience of FAT lab always kept me in a cheerful mood. The discussions and the interactions with Shadab and Jeff had a direct impact on the final form and quality of this thesis. I would like to thank Shadab for providing me tips that helped me a lot whenever I went off track. It was not possible to continue my work without his companionship and cheerful support. Erik, Jeff and Amitoj Likhari have read parts of my thesis and provided me valuable comments. Alexander Pacheco has helped me tremendously in getting the thesis in correct format. My friend and colleague since my undergrad days,

Guruditta Golani, have been of great help in the last days of thesis writing to meet all the crucial deadlines.

I feel a deep sense of gratitude for my loving father and mother who formed part of my vision and taught me to be a good human being first and then anything else. I thank my three great loving brothers, Nishant Kumar Ranjan, Prashant Agrawal and Ravikant Ranjan, for always bestowing their love on me and always believing in me. I thank my brother Prashant Agrawal for constantly encouraging me to pursue excellence and providing me emotional and financial support in my hardest time. He has been a constant source of motivation and inspiration since my childhood days. I am fortunate to have a big brother like him.

Last but not least, I would like to express my gratitude to my friend Prashant Kumar Singh from my undergrad days, who took time out of his busy schedule to provide unwavering support and help when I needed most.

TABLE OF CONTENTS

page

ACKNOWLEDGMENTS iii

LIST OF TABLES vi

LIST OF FIGURES vii

ABSTRACT xi

CHAPTER

1 INTRODUCTION 1

2 COMPUTATION OF STRESS INTENSITY FACTORS FOR SINGLE CRYSTAL : LITERATURE REVIEW 17

3 SIF EQUATION FORMULATION FOR MIXED MODE LOADING . . 23

4 MODELING AND MESHING 30

5 MIXED MODE SIF: RESULTS AND DISCUSSION 36

6 FCG GROWTH IN FCC SINGLE CRYSTAL MATERIALS 58

6.1 Isotropic materials 58
6.2 FCC single crystal materials 61

7 CONCLUSIONS 78

APPENDIX

A DISPLACEMENT FIELD EVALUATION FOR AN ANISOTROPIC ELASTIC SOLID 81

B DETAILS OF SIF EQUATION FORMULATION 95

C ANSYS PROGRAM 102

REFERENCES 121

BIOGRAPHICAL SKETCH 126

LIST OF TABLES

Table page

1–1 Direction cosines of material coordinate axes (xyz) with universal coordinate axes $(x'y'z')$ 8

1–2 Direction cosine of (x', y', z') with (x, y, z) coordinate axes, when x' axis is aligned along [213] orientation. 16

3–1 Geometrical and material properties of the two specimens analyzed . . 28

6–1 The geometry and loading condition of the three Brazilian Disk specimen tested 68

6–2 K_{rss} for 12 primary slip systems with increasing crack length for specimen 95830 75

6–3 K_{rss} for 12 primary slip systems with increasing crack length for specimen 96842 76

6–4 K_{rss} for 12 primary slip systems with increasing crack length for specimen 98C21 77

LIST OF FIGURES

Figure page

1–1 Schematic of the γ' precipitate in a γ matrix 2

1–2 Cuboidal γ' precipitates (0.35-0.6 μm) in PWA1480. 3

1–3 Temperature capability of superalloys with approximate year of introduction. 4

1–4 Aeroengine blades are nominally oriented in the $\langle 001 \rangle$ orientation. . . 4

1–5 Material coordinate system (xyz) relative to universal coordinate system $(x'y'z')$ 11

1–6 Two separated portions of a single crystal showing a model for calculating the resolved shear stress in a single-crystal specimen. 11

1–7 Slip lines and fracture plane in experimental tensile test specimen tested by Materials Science and Engineering Department, UF. . . . 12

1–8 Primary (Close-pack) and Secondary (Nonclose-pack) slip directions on the octahedral planes for an FCC crystal. 14

1–9 Cube slip planes and slip directions for an FCC crystal. 15

3–1 Crack tip nodal displacement of isotropic elastic material 24

3–2 The $\langle 101 \rangle$ and $\langle 121 \rangle$ family of slip directions are superimposed on $\{111\}$ plane showing how the hexagonal crack front is delineated by the slip directions. 27

3–3 Brazilian disk having center crack lying in $\{111\}$ slip plane and aligned along $\left[\bar{1}2\bar{1}\right]$ direction 28

3–4 Rectangular specimen 'A' meshed with solid95 element (left) and the geometrical details (right) 29

3–5 Brazilian disk (Specimen 'B') with center crack lying in (111) plane and oriented along $\left[10\bar{1}\right]$ direction 29

4–1 Brazilian disk meshed with triangular element having isotropic properties (left) and zoomed view of crack tip (right). 31

4–2 (a) 20 node isoparametric element in natural coordinate system and (b) Quarter point singular element with the $\zeta = -1$ face collapsed in local Cartesian coordinate system. 33

4–3 Arrangement of quarter-point wedge elements along segment of crack front with nodal lettering convention. 34

4–4 The symmetric meshing of BD specimen with solid95 element and enlarged picture of crack tip elements 34

5–1 K_I versus Crack Length/Width ratio for $[10\bar{1}]$ and $[\bar{1}2\bar{1}]$ orientation of Specimen 'A' at $\phi = 0^0$. 37

5–2 K_{II} versus Crack Length/Width ratio for $[10\bar{1}]$ and $[\bar{1}2\bar{1}]$ orientation of Specimen 'A' at $\phi = 0^0$. 38

5–3 K_{III} versus Crack Length/Width ratio for $[10\bar{1}]$ and $[\bar{1}2\bar{1}]$ orientation of Specimen 'A' at $\phi = 0^0$. 38

5–4 K_I versus crack angle with force for $[10\bar{1}]$ and $[\bar{1}2\bar{1}]$ orientation of Specimen 'A' at $2a/W = 0.4$. 39

5–5 K_{II} versus crack angle with force for $[10\bar{1}]$ and $[\bar{1}2\bar{1}]$ orientation of Specimen 'A' at $2a/W = 0.4$. 39

5–6 K_{III} versus crack angle with force for $[10\bar{1}]$ and $[\bar{1}2\bar{1}]$ orientation of Specimen 'A' at $2a/W = 0.4$. 40

5–7 K_I versus Crack Length/Diameter ratio for $[10\bar{1}]$ and $[\bar{1}2\bar{1}]$ orientation of Specimen 'B' at $\phi = 0^0$. 41

5–8 K_{II} versus Crack Length/Diameter ratio for $[10\bar{1}]$ and $[\bar{1}2\bar{1}]$ orientation of Specimen 'B' at $\phi = 0^0$. 42

5–9 K_{III} versus Crack Length/Diameter ratio for $[10\bar{1}]$ and $[\bar{1}2\bar{1}]$ orientation of Specimen 'B' at $\phi = 0^0$. 42

5–10 K_I versus crack angle with force for $[10\bar{1}]$ and $[\bar{1}2\bar{1}]$ orientation of Specimen 'B' at $2a/W = 0.55$. 43

5–11 K_{II} versus crack angle with force for $[10\bar{1}]$ and $[\bar{1}2\bar{1}]$ orientation of Specimen 'B' at $2a/W = 0.55$. 43

5–12 K_{III} versus crack angle with force for $[10\bar{1}]$ and $[\bar{1}2\bar{1}]$ orientation of Specimen 'B' at $2a/W = 0.55$. 44

5–13 Half meshed model of Brazilian disk specimen and the crack coordinate system 45

5–14 Variation of SIF K_I along isotropic BD specimen thickness at different Crack angle. 46

5–15 Variation of SIF K_I along orthotropic BD specimen thickness at different Crack angle. 47

5–16 Variation of SIF K_{II} along isotropic BD specimen thickness at different Crack angle. 47

5–17 Variation of SIF K_{II} along orthotropic BD specimen thickness at different Crack angle. 48

5–18 Variation of SIF K_{III} along isotropic BD specimen thickness at different Crack angle. 48

5–19 Variation of SIF K_{III} along orthotropic BD specimen thickness at different Crack angle. 49

5–20 a)Unsymmetry about mid plane for crack oriented along $\{111\}\langle 101\rangle$; b) Symmetry for crack lying along $\{111\}\langle 121\rangle$ 50

5–21 Variation of SIF K_I along BD specimen thickness at different Crack angle for $[10\bar{1}]$ orientation. 52

5–22 Variation of SIF K_I along BD specimen thickness at different Crack angle for $[\bar{1}2\bar{1}]$ orientation. 52

5–23 Variation of SIF K_{II} along BD specimen thickness at different Crack angle for $[10\bar{1}]$ orientation. 53

5–24 Variation of SIF K_{II} along BD specimen thickness at different Crack angle for $[\bar{1}2\bar{1}]$ orientation. 53

5–25 Variation of SIF K_{III} along BD specimen thickness at different Crack angle for $[10\bar{1}]$ orientation. 54

5–26 Variation of SIF K_{III} along BD specimen thickness at different Crack angle for $[\bar{1}2\bar{1}]$ orientation. 54

5–27 Variation of SIF K_I along BD specimen thickness at different Crack Length/Diameter ratio for $[10\bar{1}]$ orientation. 55

5–28 Variation of SIF K_I along BD specimen thickness at different Crack Length/Diameter ratio for $[\bar{1}2\bar{1}]$ orientation. 55

5–29 Variation of SIF K_{II} along BD specimen thickness at different Crack Length/Diameter ratio for $[10\bar{1}]$ orientation. 56

5–30 Variation of SIF K_{II} along BD specimen thickness at different Crack Length/Diameter ratio for $[\bar{1}2\bar{1}]$ orientation. 56

5–31 Variation of SIF K_{III} along BD specimen thickness at different Crack Length/Diameter ratio for $[10\bar{1}]$ orientation. 57

5–32 Variation of SIF K_{III} along BD specimen thickness at different Crack Length/Diameter ratio for $[\bar{1}2\bar{1}]$ orientation. 57

6–1 Schematic Fatigue Crack Growth Curve 59

6–2 Fatigue Crack Length versus Applied Cycles. Fracture is Indicated by the x. 61

6–3 Microscopic slip observed on two {111} slip planes inclined 52^0 and -38^0 to the starter notch 62

6–4 Details of crack tip displacements and stresses at a distance r and θ from the crack tip in the crack coordinate system 64

6–5 Burgers vector $\overrightarrow{b}$ is along slip direction $\langle 011 \rangle$ and slip plane direction is normal vector $\overrightarrow{n}$ along $\langle 111 \rangle$ 65

6–6 Fatigue crack growth rate as a function of ΔK_{rss} and ΔK for 2-D rectangular specimen. 65

6–7 Crack growth of BD specimen 95830 with no. of cycles 69

6–8 Crack growth of BD specimen 96842 with no. of cycles 69

6–9 Crack growth of BD specimen 98C21 with no. of cycles 69

6–10 Crack growth rate of BD specimen 95830 with increasing crack length 70

6–11 Crack growth rate of BD specimen 96842 with increasing crack length 70

6–12 Crack growth rate of BD specimen 98C21 with increasing crack length 70

6–13 Trace of primary slip planes on the plane normal to the crack plane . 71

6–14 Crack growth on {111} slip plane can be observed for 96842 BD specimen 73

6–15 Fatigue crack growth rate of 3 specimens 95830, 96842, 98C21, as a function of ΔK_{rms} 74

6–16 Fatigue crack growth rate of 3 specimens 95830, 96842, 98C21, as a function of ΔK_{rss} 74

A–1 Forces acting on a rectangular element with dimension $dx \times dy$ 81

Abstract of Dissertation Presented to the Graduate School
of the University of Florida in Partial Fulfillment of the
Requirements for the Degree of Doctor of Philosophy

DEVELOPMENT OF A NUMERICAL PROCEDURE FOR MIXED MODE K-SOLUTIONS AND FATIGUE CRACK GROWTH IN FCC SINGLE CRYSTAL SUPERALLOYS

By

Srikant Ranjan

August 2005

Chair: N. K. Arakere
Major Department: Mechanical and Aerospace Engineering

Fatigue-induced failures in aircraft gas turbine and rocket engine turbopump blades and vanes are a pervasive problem. Turbine blades and vanes represent perhaps the most demanding structural applications due to the combination of high operating temperature, corrosive environment, high monotonic and cyclic stresses, long expected component lifetimes and the enormous consequence of structural failure. Single crystal nickel-base superalloy turbine blades are being utilized in rocket engine turbopumps and jet engines because of their superior creep, stress rupture, melt resistance, and thermomechanical fatigue capabilities over polycrystalline alloys. These materials have orthotropic properties making the position of the crystal lattice relative to the part geometry a significant factor in the overall analysis. Computation of stress intensity factors (SIFs) and the ability to model fatigue crack growth rate at single crystal cracks subject to mixed-mode loading conditions are important parts of developing a mechanistically based life prediction for these complex alloys.

A general numerical procedure has been developed to calculate SIFs for a crack in a general anisotropic linear elastic material subject to mixed-mode loading conditions, using three-dimensional finite element analysis (FEA). The procedure does not require an apriori assumption of plane stress or plane strain conditions. The SIFs K_I, K_{II}, and K_{III} are shown to be a complex function of the coupled 3D crack tip displacement field. A comprehensive study of variation of SIFs as a function of crystallographic orientation, crack length, and mode-mixity ratios is presented, based on the 3D elastic orthotropic finite element modeling of tensile and Brazilian Disc (BD) specimens in specific crystal orientations. Variation of SIF through the thickness of the specimens is also analyzed.

The resolved shear stress intensity coefficient or effective SIF, K_{rss}, can be computed as a function of crack tip SIFs and the resolved shear stress on primary slip planes. The maximum value of K_{rss} and ΔK_{rss} was found to determine the crack growth direction and the fatigue crack growth rate respectively. The fatigue crack driving force parameter, ΔK_{rss}, forms an important multiaxial fatigue damage parameter that can be used to predict life in superalloy components.

CHAPTER 1
INTRODUCTION

A superalloy is a group of nickel-, iron-nickel-, and cobalt-base metallic alloys which can be used at high temperatures, often in excess of 0.7 of the absolute melting temperature. Exceptional creep and high temperature oxidation resistance are two of the prime design criteria of superalloys, but apart from these properties they exhibit a combination of high strength at high temperature, stress rupture resistance, toughness and metallurgical stability, useful thermal expansion characteristics and strong resistance to thermal fatigue. They exhibit exceptional corrosion resistance at room temperature. The high temperature strength of Ni-based superalloys depends on a stable, face centered cubic (FCC) matrix, combined with either precipitation strengthening and/or solid solution hardening. Iron, nickel, and cobalt are generally face centered cubic (FCC-austenitic) in crystal structure when they are the basis for superalloys. However, the normal room-temperature structures of iron and cobalt elemental metals are not FCC. Both iron and cobalt undergo transformations and become FCC at high temperatures or in the presence of other elements alloyed with iron and cobalt. Nickel, on the other hand, is FCC at all temperatures. The microstructure of an FCC superalloy consists of an austenitic (γ phase) matrix and a wide variety of secondary phase. The most common secondary phases are γ' and metal carbides. The microstructure consists of ˜60 percent by volume of γ' precipitates in a γ matrix. These alloys obtain their high-temperature strength from the presence of the γ' precipitate phase within the primary γ matrix. The γ' precipitate is a face centered cubic (FCC) structure and composed of the intermetallic compound Ni_3Al, with Al atoms occupying the corners and Ni the faces of the unit cell. The γ' precipitate is

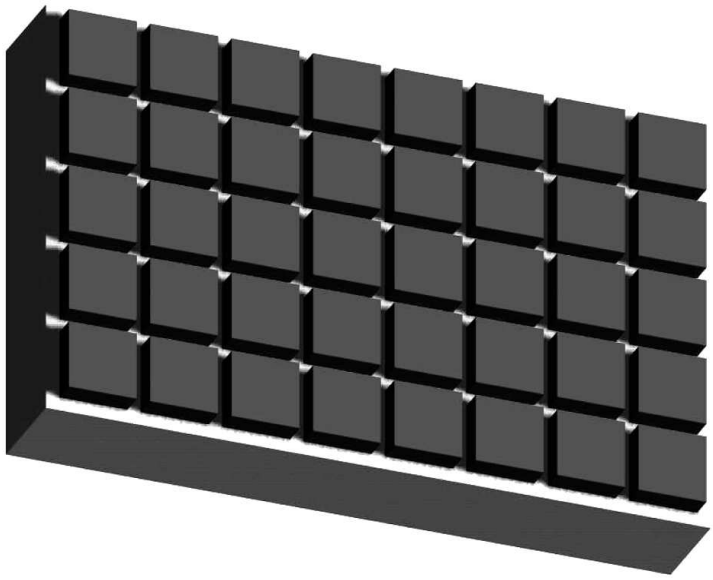

Figure 1–1: Schematic of the γ' precipitate in a γ matrix

suspended within the γ matrix, which is also of FCC structure and comprised of Ni with cobalt, chromium, tungsten, and tantalum in solution. Typically the γ phase consists of the elements from groups V, VI and VII of the periodic table. The role of γ' phase within the solid solution strengthened alloy is to increase the resistance to dislocation motion. The magnitude of the strengthening effect of γ' is governed by the degree of $\gamma/\ \gamma'$ mismatch. The greater the mismatch, the higher is the strength increment (Fig. 1–1 shows a schematic diagram of the γ' phase within the γ matrix [1] and Fig. 1–2 on page 3 shows a picture of cuboidal γ' precipitate in γ matrix [2]). Hence shearing of the precipitate is required in order for a dislocation to move through the γ matrix. Shearing of the γ' precipitate relative to the γ matrix requires significantly higher energy, resulting in a stronger material.

Nickel base single crystal superalloys are precipitation strengthened cast monograin superalloys based on the Ni-Cr-Al system. These alloys exhibit better high temperature properties than polycrystalline wrought or cast alloys (Fig. 1–3 on page 4). In high temperature application grain boundaries are typically the weak link, which provide passages for diffusion and oxidation, which results in

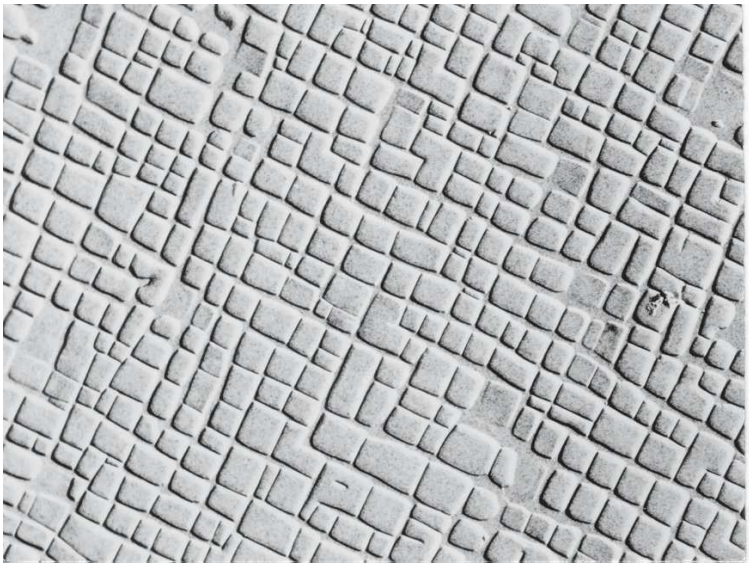

Figure 1–2: Cuboidal γ' precipitates (0.35-0.6 μm) in PWA1480.

failures at this location. Grain boundary strengtheners are added to the alloy chemistry to increase capability, which results in lowering the melting point of the alloy.

Removal of grain boundaries and grain boundary strengthening elements raise the incipient melting temperature of the alloy by 150^o F and result in improved high temperature fatigue and creep capabilities [4]. This increase in melt temperature permits higher heat treatment temperature that in turn yields improved creep capability. Unlike the more commonly used polycrystalline alloys, these single crystal superalloys are orthotropic and have highly directional material properties with exceptional thermo mechanical fatigue properties at high temperature. The most common primary growth direction for the nickel-base superalloys is the $\langle 001 \rangle$ direction. This is not only the most easily grown but also is the direction with the most desirable combined strength properties. This is advantageous because many parts are cast, or grown, rather than machined from a larger single crystal sample with a specific orientation.

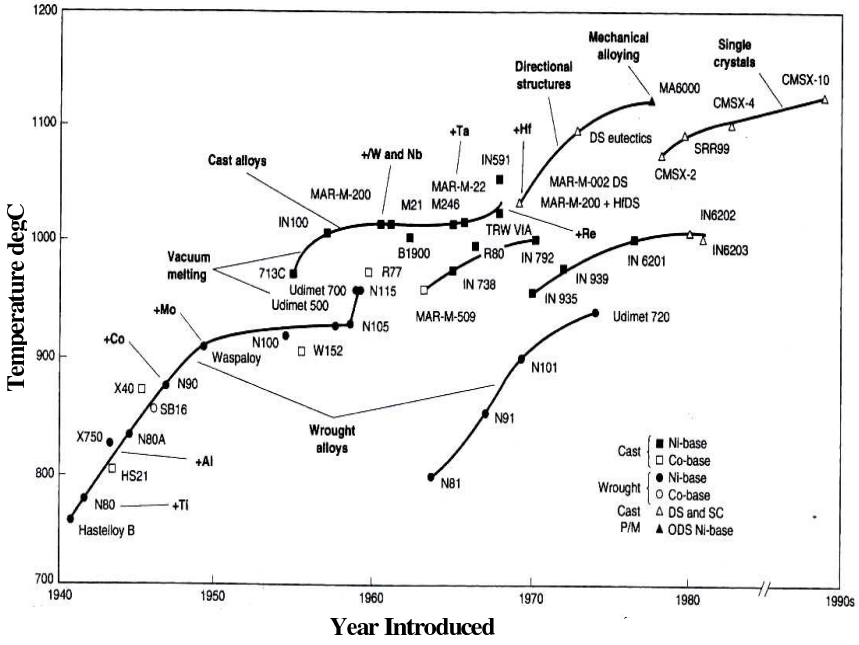

Figure 1–3: Temperature capability of superalloys with approximate year of introduction. [3]

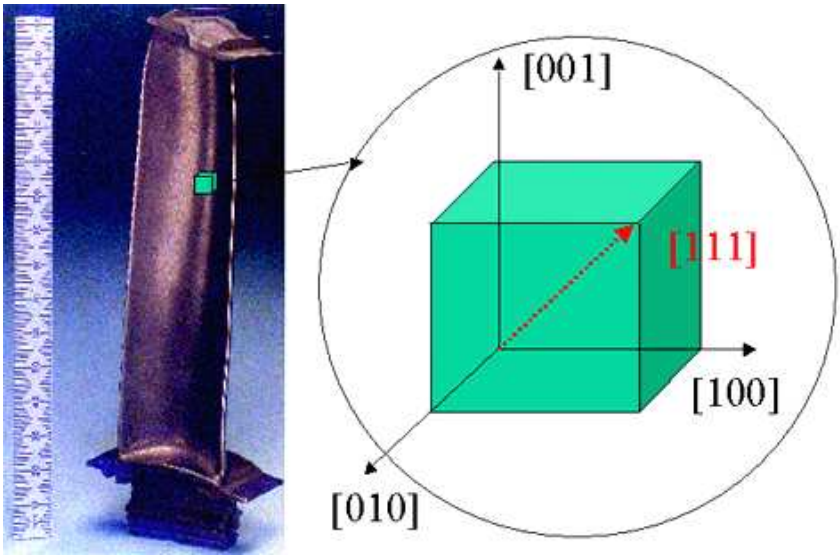

Figure 1–4: Aeroengine blades are nominally oriented in the ⟨001⟩ orientation.[5]

Currently the primary direction (growth direction) can be controlled relatively well, but still has an allowable deviation of 15^o in any direction. Although it is possible to reduce this deviation by simply discarding those parts with larger variations, the cost in wasted materials would be too great and would result in a significant percentage of scraped parts. The material properties vary greatly as the primary direction deviates from the $< 001 >$ orientation and it is important to quantify the effect of other orientations on material properties. The blades used in aeroengines are nominally oriented in the $< 001 >$ orientation (Fig. 1–4 on page 4) as this orientation has the best combination of mechanical properties. However in practice, due to the difficulties encountered in casting and due to cost considerations, blades that are oriented away from the $< 001 >$ orientation by up to 15^o are used. Also in the operating environment the blades are subjected to loading in a variety of orientations due to the hot impinging gases causing bending and torsion. The formation of hotspots leads to thermal gradients, which also contribute to multiaxial loading. The secondary orientation can also be controlled during casting; however most manufacturers choose to ignore this control to achieve greater productivity. The material can be examined after casting to determine secondary orientation, and if a particular secondary orientation has beneficial material properties for the specific application, the part can be further manufactured by cutting from the cast piece.

The Deformation Mechanisms of crystalline materials can be described as below:

Elastic Deformation of Polycrystalline (Isotropic) Metals: Most engineering structural components are fine grained polycrystalline metals, with isotropic material properties. The elastic deformation of these materials follows Hooke's law, given as

$$\{\epsilon\} = [a_{ij}]\{\sigma\} \tag{1.1}$$

$[a_{ij}]$ is the matrix of 36 elastic coefficients, of which only 21 are independent, since $[a_{ij}] = [a_{ji}]$. Depending on the the material structure, the crystalline material displays different forms of geometric symmetry. There are 32 forms of geometric symmetry of crystals, which can be further divided into seven crystal systems called syngony: 1) triclinic, 2) monoclinic, 3) rhombic, 4) tetragonal, 5) trigonal, 6) hexagonal, and 7) cubic [6]. For an isotropic material the mechanical properties (E, ν, G) are the same at each point of the material because it can have only two independent elastic constants as

$$a_{11} = a_{22} = a_{33} \qquad a_{12} = a_{13} = a_{23} \qquad a_{44} = a_{55} = a_{66} = 2(a_{11} - a_{12}) \tag{1.2}$$

and the rest of the coefficients of deformations are zero.

$$[a_{ij}] = \begin{bmatrix} a_{11} & a_{12} & a_{12} & 0 & 0 & 0 \\ a_{12} & a_{11} & a_{12} & 0 & 0 & 0 \\ a_{12} & a_{12} & a_{11} & 0 & 0 & 0 \\ 0 & 0 & 0 & a_{44} & 0 & 0 \\ 0 & 0 & 0 & 0 & a_{44} & 0 \\ 0 & 0 & 0 & 0 & 0 & a_{44} \end{bmatrix} \tag{1.3}$$

An isotropic material subjected to multiaxial loading, under mechanical equilibrium, has three principal stresses. These principal stresses act on orthogonal planes, which are free of shear stresses. The Von Mises and Tresca criterions are two of the most widely used yield criteria for ductile isotropic materials.

Anisotropic Elastic Deformation of FCC Single Crystal: The generalized Hooke's law for a homogeneous anisotropic elastic body in a cartesian coordinate system (x, y, z with origin at point O, Fig. 1–5 on page 11) is given by equation (1.4) [6]

$$\{\epsilon\} = [a_{ij}]\{\sigma\} \tag{1.4}$$

The elastic properties of FCC crystals exhibit cubic syngony; i.e., it has three orthogonal planes of elastic symmetry at every point, which is called orthogonally-anisotropic or, for brevity, orthotropic. Therefore cubic symmetry can be described with three independent constants designated as the elastic modulus, shear modulus, and Poisson's ratio [4] and hence $[a_{ij}]$ can be expressed as shown in equation (1.3), in the material coordinate system (FCC crystal axes are parallel to x, y and z coordinate axes) and the coefficient of deformation is given as

$$a_{11} = \frac{1}{E_{xx}},\ a_{44} = \frac{1}{G_{yx}},\ a_{12} = -\frac{\nu_{yx}}{E_{xx}} = -\frac{\nu_{xy}}{E_{yy}} \tag{1.5}$$

The elastic constants in the generalized Hooke's law of an anisotropic body, $[a_{ij}]$, vary with the direction of the coordinate axes. For orientations other than the (x, y, z) axes, the $[a_{ij}]$ matrix varies with the crystal orientation. In the case of an isotropic body the constants are invariant in any orthogonal coordinate system. Consider a Cartesian coordinate system (x', y', z') that has rotated about the origin O of (x, y, z). The elastic constant matrix $\left[a'_{ij}\right]$ in the (x', y', z') coordinate system that relates $\{\epsilon'\}$ and $\{\sigma'\}$ is

$$\{\epsilon'\} = [a'_{ij}]\{\sigma'\} \tag{1.6}$$

where $\left[a'_{ij}\right]$ is given by the following transformation

$$[a'_{ij}] = [Q]^T [a_{ij}] [Q] = \sum_{m=1}^{6} \sum_{n=1}^{6} a_{mn} Q_{mi} Q_{mj} \qquad (i, j = 1, 2, ..., 6) \tag{1.7}$$

where $[Q]$ is the transformation matrix, which is a function of the direction cosines between the(x, y, z) and (x', y', z') coordinate axes (Fig. 1–5 on page 11, Table 1–1 on page 8). Here α, β and γ are the direction cosines of the material coordinate system relative to the universal coordinate system (specimen coordinate system).

$$[Q] = \begin{bmatrix} \alpha_1^2 & \alpha_2^2 & \alpha_3^2 & 2\alpha_2\alpha_3 & 2\alpha_3\alpha_1 & 2\alpha_1\alpha_2 \\ \beta_1^2 & \beta_2^2 & \beta_3^2 & 2\beta_2\beta_3 & 2\beta_3\beta_1 & 2\beta_1\beta_2 \\ \gamma_1^2 & \gamma_2^2 & \gamma_3^2 & 2\gamma_2\gamma_3 & 2\gamma_3\gamma_1 & 2\gamma_1\gamma_2 \\ \beta_1\gamma_1 & \beta_2\gamma_2 & \beta_3\gamma_3 & \beta_2\gamma_3 + \beta_3\gamma_2 & \beta_1\gamma_3 + \beta_3\gamma_1 & \beta_1\gamma_2 + \beta_2\gamma_1 \\ \gamma_1\alpha_1 & \gamma_2\alpha_2 & \gamma_3\alpha_3 & \gamma_2\alpha_3 + \gamma_3\alpha_2 & \gamma_1\alpha_3 + \gamma_3\alpha_1 & \gamma_1\alpha_2 + \gamma_2\alpha_1 \\ \alpha_1\beta_1 & \alpha_2\beta_2 & \alpha_3\beta_3 & \alpha_2\beta_3 + \alpha_3\beta_2 & \alpha_1\beta_3 + \alpha_3\beta_1 & \alpha_1\beta_2 + \alpha_2\beta_1 \end{bmatrix} \tag{1.8}$$

Table 1–1: Direction cosines of material coordinate axes (xyz) with universal coordinate axes $(x'y'z')$

	x	y	z
x'	α_1	α_2	α_3
y'	β_1	β_2	β_3
z'	γ_1	γ_2	γ_3

Also the transformation of the stress and strain tensors between the material and specimen coordinate systems is necessary for implementing the failure theories. The components of stresses and strains in the (x', y', z') system in terms of the (x, y, z) system are given by

$$\begin{aligned} \{\sigma'\} &= [Q']\{\sigma\}; \qquad \{\epsilon'\} = [Q'_\epsilon]\{\epsilon\} \\ \{\sigma\} &= [Q']^{-1}\{\sigma'\} = [Q]\{\sigma'\} \\ \{\epsilon\} &= [Q'_\epsilon]^{-1}\{\epsilon'\} = [Q_\epsilon]\{\epsilon'\} \end{aligned} \tag{1.9}$$

where

$$[Q_\epsilon] = \begin{bmatrix} \alpha_1^2 & \alpha_2^2 & \alpha_3^2 & \alpha_2\alpha_3 & \alpha_3\alpha_1 & \alpha_1\alpha_2 \\ \beta_1^2 & \beta_2^2 & \beta_3^2 & \beta_2\beta_3 & \beta_3\beta_1 & \beta_1\beta_2 \\ \gamma_1^2 & \gamma_2^2 & \gamma_3^2 & \gamma_2\gamma_3 & \gamma_3\gamma_1 & \gamma_1\gamma_2 \\ 2\beta_1\gamma_1 & 2\beta_2\gamma_2 & 2\beta_3\gamma_3 & \beta_2\gamma_3+\beta_3\gamma_2 & \beta_1\gamma_3+\beta_3\gamma_1 & \beta_1\gamma_2+\beta_2\gamma_1 \\ 2\gamma_1\alpha_1 & 2\gamma_2\alpha_2 & 2\gamma_3\alpha_3 & \gamma_2\alpha_3+\gamma_3\alpha_2 & \gamma_1\alpha_3+\gamma_3\alpha_1 & \gamma_1\alpha_2+\gamma_2\alpha_1 \\ 2\alpha_1\beta_1 & 2\alpha_2\beta_2 & 2\alpha_3\beta_3 & \alpha_2\beta_3+\alpha_3\beta_2 & \alpha_1\beta_3+\alpha_3\beta_1 & \alpha_1\beta_2+\alpha_2\beta_1 \end{bmatrix} \tag{1.10}$$

The transformation matrix $[Q]$ is orthogonal and hence $[Q]^{-1} = [Q]^T = [Q']$. Now the resolved shear stresses on the 12 primary octahedral slip systems (Table 1–2 on page 16, Fig. 1–8 on page 14), denoted by $\tau_1, \tau_2, \ldots, \tau_{12}$ can be readily obtained using the transformation given by equation (1.13) [4]. Only the primary octahedral slip systems get activated at room temperature whereas high temperature is required for the activation of the other slip systems.

Inelastic Deformation of FCC Single Crystals: Slip and twinning are two main factors responsible for inelastic deformation in metals. The main reason for deformation of crystalline metals is the propagation of dislocations through the metal's lattice when temperatures are less than 0.5 of the absolute melting temperature.

At higher temperatures, deformation occurs by dislocation climb (which is a diffusion controlled process). Twinning, a rotation of atoms in the lattice structure, is not as important as strains produced by this mechanism are very small as compared to slip and climb. On an atomic scale, plastic deformation involves the net movement of large numbers of atoms in response to an applied stress. Actual strength to deform a metal is much lower than that predicted for theoretically perfect crystals. This difference is explained by

dislocations. Plastic deformation corresponds to the motion of large numbers of dislocations. The process by which plastic deformation is produced by dislocation motion is called slip. Slip in metal crystals often occurs on planes of high atomic density in closely packed directions because these planes generally correspond to the lowest possible energy for slip. The plane on which the motion occurs is called slip plane. There is a preferred plane (slip plane) and a preferred direction within that plane (slip direction). The combination of slip plane and slip direction is called a slip system. The preferred slip plane is that with the greatest planar density. The preferred slip direction is that with the greatest linear density.

Slip mechanism. In a single crystal specimen, the extant of slip depends on the magnitude of the shearing stress. Magnitude of the resolved stress depends on the magnitude of the applied force, its orientation relative to the slip plane and slip direction. Therefore the stress-strain behavior of a material, which is a function of the number of activated slip systems, varies with orientation. A slip line or step is observed in experiments involving polished single crystals specimens as shown in Fig. 1–7 on page 12. The slip planes of highest atomic densities are the first to get activated on an FCC single crystal specimen and are called the primary octahedral slip systems.

In Fig. 1–6 on page 11, F is the applied force, A is the cross-sectional area of the specimen, ϕ is the angle between the tensile axis and the normal to the slip plane and λ is the angle between the slip direction and the tensile axis. The resolved shear stress along the slip direction can be calculated as

$$\tau_R = \sigma . \cos\phi . \cos\lambda \tag{1.11}$$

The favored slip system has the largest resolved shear stress called critical resolved shear stress. It has been observed experimentally that a single crystal will

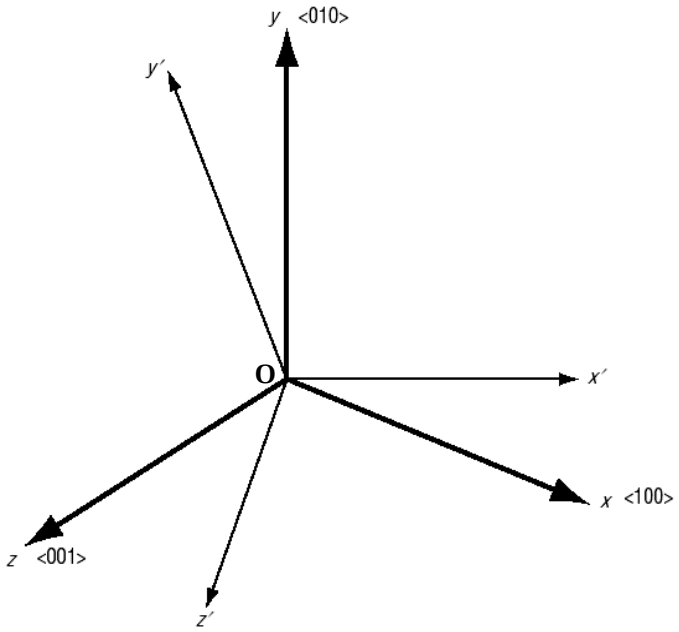

Figure 1–5: Material coordinate system (xyz) relative to universal coordinate system ($x'y'z'$)

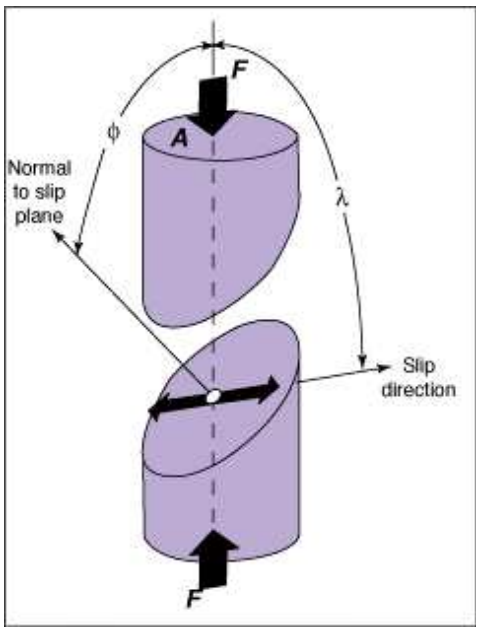

Figure 1–6: Two separated portions of a single crystal showing a model for calculating the resolved shear stress in a single-crystal specimen. [7]

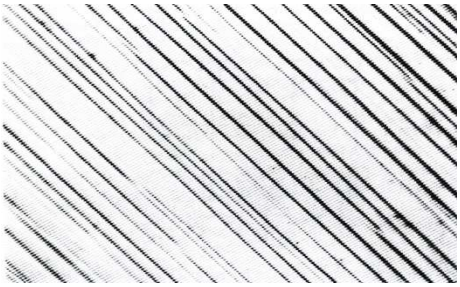

Figure 1–7: Slip Lines and Fracture Plane in experimental tensile test specimen tested by Materials Science and Engineering Department, UF. [8]

slip when the resolved shear stress on the slip plane reaches the critical resolved shear stress for that material. To calculate the stress needed to exceed this level (τ_{CRSS}) is calculated by

$$\sigma = \frac{\tau_{CRSS}}{\cos\phi.\cos\lambda}$$

σ will be a minimum when $\phi = \lambda = 45^o$

Therefore when a load is applied slip systems get activated based on Schmid factor, m. where

$$m = \cos\phi.\cos\lambda \tag{1.12}$$

This behavior is known as Schmid's law.

The value of critical resolved shear stress depends chiefly on the material composition and temperature. It is also a function of applied load and direction, crystal structure and specimen geometry. During the application of a load to an FCC single crystal specimen, the first planes to get activated are the planes of high atomic densities and called the primary octahedral slip systems. Each octahedral plane has six slip directions associated with it. Three of these are termed easy slip or primary slip directions and the other three are secondary slip directions. Thus, there are 12 primary and 12 secondary slip directions associated with the four octahedral planes (Fig. 1–8 on page 14). In addition, there are six possible slip directions in the three cube planes, as shown in Fig. 1–9 on page 15. There are 30 possible slip systems in an FCC crystal (Table 1–2 on page 16).

The resolved shear stress on the 12 primary slip systems, based on kinematic relations, can be shown to be

$$\begin{Bmatrix} \tau^1 \\ \tau^2 \\ \tau^3 \\ \tau^4 \\ \tau^5 \\ \tau^6 \\ \tau^7 \\ \tau^8 \\ \tau^9 \\ \tau^{10} \\ \tau^{11} \\ \tau^{12} \end{Bmatrix} = \frac{1}{\sqrt{6}} \begin{bmatrix} 1 & 0 & -1 & 1 & 0 & -1 \\ 0 & -1 & 1 & -1 & 1 & 0 \\ 1 & -1 & 0 & 0 & 1 & -1 \\ -1 & 0 & 1 & 1 & 0 & -1 \\ -1 & 1 & 0 & 0 & -1 & -1 \\ 0 & 1 & -1 & -1 & -1 & 0 \\ 1 & -1 & 0 & 0 & -1 & -1 \\ 0 & 1 & -1 & -1 & 1 & 0 \\ 1 & 0 & -1 & -1 & 0 & -1 \\ 0 & -1 & 1 & -1 & -1 & 0 \\ -1 & 0 & 1 & -1 & 0 & -1 \\ -1 & 1 & 0 & 0 & 1 & -1 \end{bmatrix} \begin{Bmatrix} \sigma_{xx} \\ \sigma_{yy} \\ \sigma_{zz} \\ \sigma_{xy} \\ \sigma_{zx} \\ \sigma_{yz} \end{Bmatrix} \tag{1.13}$$

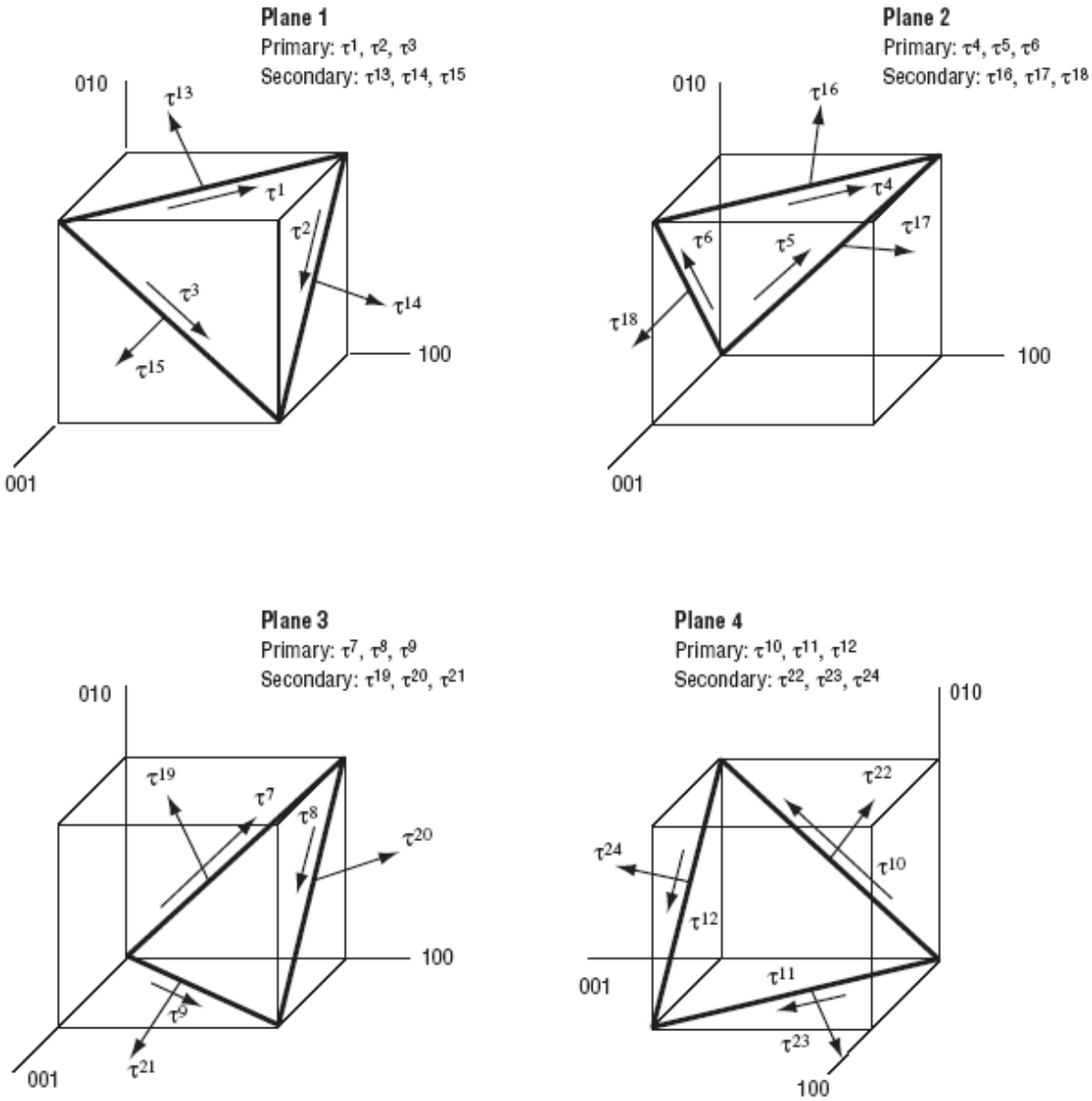

Figure 1–8: Primary (Close-pack) and Secondary (Nonclose-pack) slip directions on the octahedral planes for an FCC crystal.[9]

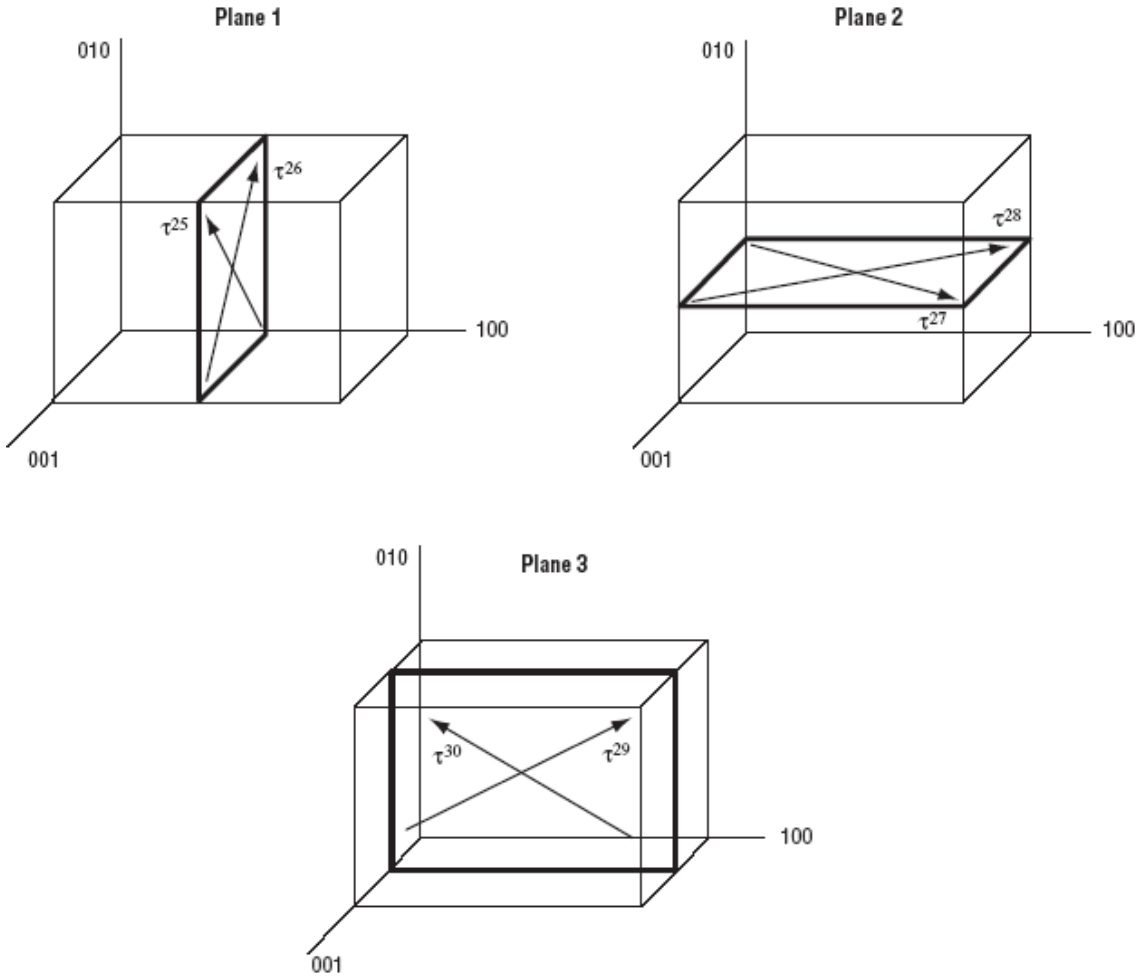

Figure 1–9: Cube slip planes and slip directions for an FCC crystal. [9]

Table 1–2: Direction cosine of (x', y', z') with (x, y, z) coordinate axes, when x' axis is aligned along [213] orientation.

Slip Number	Slip Plane	Slip Direction
	Octahedral Slip a/2{111}⟨110⟩	Primary Slip Directions
1	(111)	$[10\bar{1}]$
2	(111)	$[0\bar{1}1]$
3	(111)	$[1\bar{1}0]$
4	$(\bar{1}1\bar{1})$	$[10\bar{1}]$
5	$(\bar{1}1\bar{1})$	[110]
6	$(\bar{1}1\bar{1})$	[011]
7	$(1\bar{1}\bar{1})$	[110]
8	$(1\bar{1}\bar{1})$	$[0\bar{1}1]$
9	$(1\bar{1}\bar{1})$	[101]
10	$(\bar{1}\bar{1}1)$	[011]
11	$(\bar{1}\bar{1}1)$	[101]
12	$(\bar{1}\bar{1}1)$	$[1\bar{1}0]$
	Octahedral Slip a/2{111}⟨112⟩	Secondary Slip Directions
13	(111)	$[\bar{1}2\bar{1}]$
14	(111)	$[2\bar{1}\bar{1}]$
15	(111)	$[\bar{1}\bar{1}2]$
16	$(\bar{1}1\bar{1})$	[121]
17	$(\bar{1}1\bar{1})$	$[1\bar{1}\bar{2}]$
18	$(\bar{1}1\bar{1})$	$[\bar{2}\bar{1}1]$
19	$(1\bar{1}\bar{1})$	$[\bar{1}1\bar{2}]$
20	$(1\bar{1}\bar{1})$	[211]
21	$(1\bar{1}\bar{1})$	$[\bar{1}2\bar{1}]$
22	$(\bar{1}\bar{1}1)$	$[\bar{2}1\bar{1}]$
23	$(\bar{1}\bar{1}1)$	$[1\bar{2}\bar{1}]$
24	$(\bar{1}\bar{1}1)$	[112]
	Cubic Slip a/2{100}⟨110⟩	Cube Slip Directions
25	(100)	[011]
26	(100)	$[01\bar{1}]$
27	(010)	[101]
28	(010)	$[10\bar{1}]$
29	(001)	[110]
30	(001)	$[\bar{1}10]$

CHAPTER 2
COMPUTATION OF STRESS INTENSITY FACTORS FOR SINGLE CRYSTAL : LITERATURE REVIEW

Stress intensity factor (SIF) about a crack tip plays a significant role in the propagation of the crack. The SIF is a measure of intensity near the crack tip under linear elastic conditions. The knowledge of SIF is necessary to predict the growth of a fatigue crack or to determine the residual strength of a cracked structure. This factor characterizes the intensity of the stress field in the neighborhood of the crack tip and depends substantially on specimen geometry, material properties, external loads and crack size. In cases with idealized geometry and loads the SIF can be found in handbooks for isotropic elastic materials. In the case of more complex structures the SIF has to be computed by numerical methods.

Isotropic materials have uniform material properties in all directions, whereas anisotropic materials are directional in nature (i.e., they have different material properties in different directions). Because of this property SIF is direction invariant for isotropic materials while SIF varies in anisotropic materials due to change in material coordinate system, while keeping all the other parameters same.

A study of the effect of anisotropy and inhomogeneity on the SIF using the FEA was done by Kamaya and Kitamura [10]. It was found that in a polycrystal specimen, the SIF is influenced by the crystal orientation at the crack tip and the deformation constraint due to adjacent crystals only for very small cracks; whereas for anisotropic single crystal the SIF strongly depends on the crystal orientation, and the magnitude deviates from that in the isotropic body for any size crack. But

as crack size increases in the polycrystal materials, SIF tends to converge to values seen in homogeneous/isotropic bodies.

Many methods have been proposed, to calculate SIFs for cracks subjected to mixed-mode loading conditions in isotropic elastic solids. Some commonly used methods are J integral [11, 12], virtual crack extension [13, 14], modified crack closure integral and displacement extrapolation methods [15] etc. None of these proposed methods are able to provide the complete solution for all the three modes (Mode *I*, *II* and *III*) of SIF for anisotropic material.

Atkinson et al. [16] presented the idea of calculating mixed mode SIF using Fredholm equation transformation. They used a center cracked Brazilian disc (BD) test specimen made of isotropic material. The mode mixity ratio for the BD specimen is a function of the crack angle with respect to the load vector. Results were presented for varied crack angles and hence mode mixity ratios. Small crack approximation was also taken and the results were found to be in accordance with Awaji and Sato [17], but it did not incorporate anisotropy in the model and was limited to Mode *I* and *II* SIFs.

Su and Sun [18] studied various kinds of 2-D anisotropic cracks to evaluate SIF under mixed-mode loading condition. Fractal finite element method (FFEM) [19] was used to calculate Mode I and II SIFs for 2-D anisotropic plate. The variation of the SIFs with material properties and orientations of a crack was presented. It was shown that SIFs were not sensitive to the variation of shear modulus. Hwu and Liang [20] used remote boundary data to calculate SIFs for 2-D anisotropic material. It eliminated the error in SIF calculation, caused by abrupt change in the stresses near crack tips, by finding equivalent formulation for SIF by using only remote boundary responses (displacements, stresses and strains), cooperating with the necessary geometric data. A special boundary element was developed which removed the requirement of meshing around the crack boundary. Through

this boundary element, all the internal stresses and strains could be expressed in terms of displacements and tractions on the boundaries excluding the hole, crack and inclusion boundaries. These results could be applied to any kind of linear anisotropic materials but was restricted to the 2-D problems which included generalized plane stress, generalized plane strain and anti-plane problems.

Denda and Marante [21] developed a crack tip singular element (CTSE) for the general anisotropic solids in 2-D with the built in $\sqrt{r}$ and $1/\sqrt{r}$ singular stress behavior at its tip, which provided the SIF as an integral part of the main solution, no post processing was required. It was an ideal fracture analysis tool for 2-D multiple curvilinear cracks in general anisotropic solids, but as it was based on plane strain assumption, it could not be incorporated into a generalized 3-D anisotropic model. The solution provided by Heppler and Hansen [22] for combined mode (I and II) SIFs in case of planar, rectilinear, anisotropic structures using a 12 node singular finite element was accurate, but was restricted to a 2-D model. Likewise, Sosa and Eischen [12] calculated SIF for a plate containing a through crack subjected to bending loads using the J integral. Two-D eight node element was selected for this purpose where $K_{II} = K_{III} = 0$. Mews and Kuhn [23] used the Green's function approach to calculate mixed mode SIF without any crack discretization in an isotropic plate, which used an asymptotic displacement field at the crack tip. They calculated SIFs for plate having multiple cracks, for various inclinations, and found SIFs very close to that of Shih et al. [24]. Ishikava [14] presented the idea of the strain energy release rate (virtual crack extension method) to calculate SIF for mode I and II, and described SIF calculation based on only one use of virtual crack extension.

Huang and Kardomateas [25] described the continuous dislocation technique to calculate mixed-mode stress intensity factors in an anisotropic infinite strip. This method was limited in its use to Mode I and II SIFs, and it was found to be

most suitable for cracks of relatively small dimensions. The method was verified by calculating SIFs for isotropic material and comparing the results with readily available formulas given in Tada et al. [26], which resulted in excellent agreement. Sun et al. [27] used the boundary element method (BEM) to analyze cracked anisotropic bodies under anti-plane shear. The new boundary formulation used dislocation density as an unknown on the crack surface, and K_{III} was determined near the crack tip. The equation and method could be directly used for anti-plane problems with cracks of any geometric shapes. It did not give a complete solution under mixed-mode loading conditions, but it did give an idea about the behavior of K_{III} under anti-plane shear loading.

Shih et al. [24] have calculated SIFs for 2-D isotropic materials using quarter point element nodal displacements at the crack tip based on Finite Element Method (FEM). The Modes *I*, *II* and *III* have been decoupled because of the isotropic nature of the material. Sih et al. [28] defined SIFs as a function of stress at the crack tip. Following the work of Shih et al., Ingraffea and Manu [29] showed how to compute SIF from 3-D quarter point nodal displacement, for cracked isotropic elastic bodies for all three modes. They used a quarter point isoparametric element, which has been accurate in computing SIF [30]. Saouma and Sikiotis [31] introduced anisotropy in the above model [29] and proposed a method to calculate SIF for 3-D anisotropic elastic material based on the model of Shih et al. The computed SIFs, when compared with 2-D anisotropic bodies with known exact solutions yielded an error of 6-12% for K_I and K_{II}. However the orientation of the elastic constants was not incorporated. The expression of K_{III} was not correct as it resulted in almost zero value, irrespective of the geometry, orientation and the load applied to an anisotropic component.

Dhondt [32] analyzed two methods, interaction integral method (IINT) and the quarter point element stress method (QPES), to calculate SIF for single edge

notch specimen (SEN) and a slant crack in a 3 point bending (3PB) specimen for isotropic material. For the regular mesh in the SEN specimen both methods yielded similar results. For the irregular mesh in the 3PB specimen the QPES methods seemed to be more robust and accurate. Later Guido [33] presented a method to calculate SIF for anisotropic material using the finite difference method along an arbitrary crack. Although the model was more robust to irregular meshes in comparison to interaction integral method, this method was limited to single edge specimen and corner crack specimen.

Tweed et al. [34] used the specific case of an edge crack of an anisotropic elastic half space under generalized plane strain conditions to determine the stress intensity factors using integral transform techniques. Pan and Yuan [35] used single domain BEM to calculated mixed mode SIFs for both bounded and unbounded 3-D anisotropic cracked solids. Denda [36] used BEM to determine mixed mode SIFs (K_I, K_{II} and K_{III}) of 3-D anisotropic material with multiple cracks. It addressed the issue of coupling effect of the three modes of fracture controlled by Mode *I*, *II* and *III* SIFs. Though very accurate, these formulations were based on the plane strain assumption.

Although a substantial body of literature describes computation of SIF, a generalized numerical solution to calculate SIF for 3-D anisotropic material is unavailable. The objective of the present work is to model a 3-D orthotropic specimen having a through crack and to calculate the SIFs for all three modes assuming linear elastic properties at the crack tip. A mathematical model has been developed to calculate mixed mode SIF for FCC single crystal orthotropic material for different orientations, which is also applicable to generalized anisotropic material. Looking at the crack tip nodal displacements it is possible to calculate stress intensity factor for any crystallographic orientation of the material. It was observed that the material orthotropy results in coupled crack tip (x, y,

z) displacements, leading to the interdependence of SIFs for Modes *I*, *II*, and *III*. Results are presented for a center-cracked BD specimen, with two specific crystallographic orientations. The crack plane for the first specimen is (111) and the crack direction is $\left[10\bar{1}\right]$. For the second specimen the crack plane is again (111), while the crack direction is $\left[\bar{1}2\bar{1}\right]$. There are important reasons for choosing these two specific BD specimen configurations. These two crack directions typically represent the fastest and the slowest crystallographic crack growth rates, respectively, on the $\{111\}$ family of octahedral planes, and hence have important implications on estimating fatigue crack growth life for single crystal components [2, 37]. Even if cracks nucleate on other planes, because of local influence from intrinsic defects such as micropores, carbide particles and undissolved eutectics, they tend to migrate to the octahedral planes, in the primary slip directions ($\langle 101 \rangle$ family of directions), since they represent the paths of least resistance for crack propagation [2]. Results presented show that SIF values are consistently higher for the $\langle 101 \rangle$ crack direction, compared to the $\langle 121 \rangle$ direction, for same crack angles and loads.

CHAPTER 3
SIF EQUATION FORMULATION FOR MIXED MODE LOADING

The stress intensity solution, for all the three modes for isotropic materials, using crack tip nodal displacements method is given by [38]:

$$\begin{aligned} K_I &= \frac{\mu}{\kappa+1}\sqrt{\frac{2\pi}{L}}\ [4(v^B - v^D) + v^E - v^C] \\ K_{II} &= \frac{\mu}{\kappa+1}\sqrt{\frac{2\pi}{L}}\ [4(u^B - u^D) + u^E - u^C] \\ K_{III} &= \frac{\mu}{\kappa+1}\sqrt{\frac{2\pi}{L}}\ [4(w^B - w^D) + w^E - w^C] \end{aligned} \tag{3.1}$$

Here u, v and w are the displacements of the nodes B, C, D and E at the crack tip along x, y and z directions respectively. L is the length of the element at the crack tip normal to the crack front (Fig. 3–1 on page 24).

These equations show that all three stress intensity factors K_I, K_{II} and K_{III} are decoupled. For anisotropic materials it is not possible to use the same equation, as their material properties are direction dependent. Because of this directional dependence the stress intensity factor for the same material changes according to the orientation of the crack plane with material orientation.

As has been discussed earlier, an orthotropic material has three independent elastic constants, E, ν and G. The elastic constants in material coordinate system get transformed to specimen coordinate system by equation (1.7). The interdependence of displacements in anisotropic materials due to shear coupling results in coupled stress intensity factors.

Anisotropy was incorporated in the 3-D model to calculate SIF for mixed-mode loading. It can be shown that mixed mode stress intensity factors can be

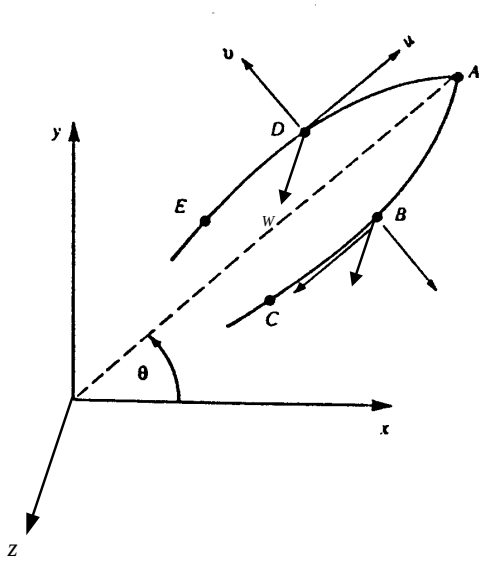

Figure 3–1: Crack tip nodal displacement of isotropic elastic material for calculation of Stress Intensity Factors of Mode I, II and III

computed by equation (3.2) [28] [29][1] .

$$\begin{Bmatrix} K_I \\ K_{II} \\ K_{III} \end{Bmatrix} = [B]^{-1}[A]\sqrt{\frac{\pi}{2L_1}} \tag{3.2}$$

Where L_1 is the element length along the crack face and $\{A\}$ is given as

$$\{A\} = \begin{Bmatrix} 2u_B - u_C + 2u_E - u_F + u_D + \frac{1}{2}\eta(-4u_B + u_C + 4u_E - u_F) + \\ \frac{1}{2}\eta^2(u_F + u_C - 2u_D) \\ 2v_B - v_C + 2v_E - v_F + v_D + \frac{1}{2}\eta(-4v_B + v_C + 4v_E - v_F) + \\ \frac{1}{2}\eta^2(v_F + v_C - 2v_D) \\ 2w_B - w_C + 2w_E - w_F + w_D + \frac{1}{2}\eta(-4w_B + w_C + 4w_E - w_F) + \\ \frac{1}{2}\eta^2(w_F + w_C - 2w_D) \end{Bmatrix} \tag{3.3}$$

[1] The details of the equation are given in Appendix B

Here u, v and w are the nodal displacements of nodes B, C, D, E and F at the crack tip relative to B', C', D', E', and F' as shown in Fig. 4–3 on page 34.

η is the natural co-ordinate system value defined as

$$\eta = -(\frac{2z}{L_2} + 1) \tag{3.4}$$

L_2 is the length of the element along the crack front (Fig. 4–2 on page 33) and $[B]^{-1}$ is defined as

$$[B]^{-1} = \begin{bmatrix} Re[\frac{i}{\mu_1-\mu_2}(q_2-q_1)]\frac{1}{D} & Re[\frac{-i}{\mu_1-\mu_2}(p_2-p_1)]\frac{1}{D} & 0 \\ Re[\frac{-i}{\mu_1-\mu_2}(\mu_1 q_2-\mu_2 q_1)]\frac{1}{D} & Re[\frac{i}{\mu_1-\mu_2}(\mu_1 p_2-\mu_2 p_1)]\frac{1}{D} & 0 \\ 0 & 0 & \sqrt{c_{44}c_{55}-c_{45}^2} \end{bmatrix} \tag{3.5}$$

As it is apparent from the $[B]^{-1}$ matrix that K_I and K_{II} are only coupled SIFs (function of u and v) and K_{III} is function of w only.

D is the determinant of the equation

$$D = \begin{vmatrix} Re[\frac{i}{\mu_1-\mu_2}(\mu_1 p_2-\mu_2 p_1)] & Re[\frac{i}{\mu_1-\mu_2}(p_2-p_1)] \\ Re[\frac{i}{\mu_1-\mu_2}(\mu_1 q_2-\mu_2 q_1)] & Re[\frac{i}{\mu_1-\mu_2}(q_2-q_1)] \end{vmatrix} \tag{3.6}$$

μ_1 and μ_2 are the roots of the fourth order characteristic equation

$$a_{11}\mu^4 - 2a_{16}\mu^3 + (2a_{12}+a_{66})\mu^2 - 2a_{26}\mu + a_{22} = 0 \tag{3.7}$$

and given by

$\mu_j = \alpha_j + i\beta_j$and $\beta_j > 0$ (as μ_j can be only a complex no.[6][2])

[2] The fourth order equation formulation was followed from the work of Lekhnitskii [6], refer to Appendix A.

$$\begin{aligned} p_j &= a_{11}\mu_j^2 + a_{12} - a_{16}\mu_j \\ q_j &= a_{12}\mu_j + \frac{a_{22}}{\mu_j} - a_{26} \end{aligned} \tag{3.8}$$

For Plane stress,

$$a_{11} = \frac{1}{E_{11}}; \qquad a_{22} = \frac{1}{E_{22}}; \qquad a_{21} = a_{12} = -\frac{\nu_{12}}{E_{11}}; \qquad a_{66} = \frac{1}{G_{12}} \tag{3.9}$$

For Plane strain,

$$a_{ij} = a_{ij} - \frac{a_{i3}a_{j3}}{a_{33}} \tag{3.10}$$

Equation (3.2) is used to calculate the SIF at the crack tip by displacement method; one of the most used methods to get the value accurately. Finite Element Method was used to calculate the displacements at the crack tip. The commercial software, ANSYS, was used for FEA modeling. The crack tip nodal displacements were then extracted from FEA model and fed to the analytical equations explained above to calculate all the three modes of SIFs.

Single Crystal Specimen Geometries Used for Mixed-Mode Loading. Two specimen geometries were used to investigate the effects of mode mixity at the crack tip. One was a rectangular tension specimen (Fig. 3–4 on page 29) with a center crack loaded such that the crack lied in the {111} plane. The crack directions used were ⟨101⟩ and ⟨121⟩ family of directions.

The second specimen modeled is a round Brazilian disk (BD) specimen, loaded in compression. This specimen with center crack has a mode mixity at the crack tip, which varies as function of the crack angle 'ϕ', shown in Fig. 3–5 on page 29. The crack lies on the {111} plane and crack directions used are ⟨101⟩ and ⟨121⟩ family of directions. These specimen and crack orientations have been checked very carefully, based on experimentally observed fatigue crack growth rates (FCGR) [39]. At low temperature ($< 427^0C$), the dominant mode of FCG in FCC single crystal superalloys is crystallographic crack propagation on octahedral planes

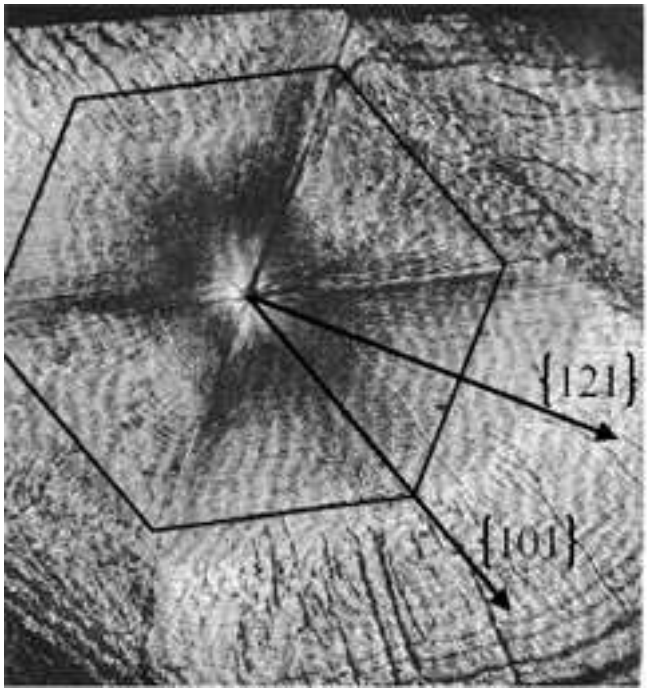

Figure 3–2: The ⟨101⟩ and ⟨121⟩ family of slip directions are superimposed on {111} plane showing how the hexagonal crack front is delineated by the slip directions.[37]

[37]. Extensive FCGR studies have shown that the fastest crack growth rates are observed for cracks propagating on the {111} plane, in the ⟨101⟩ family of directions. A slower FCGR has been observed with the crack on the {111} plane, in the ⟨121⟩ family of directions. Hence the FCGR on the {111} plane, in these two directions typically provide the fastest and the slowest crystallographic crack propagation rates. This variation in FCGR in the ⟨101⟩ and ⟨121⟩ directions, on the {111} is illustrated in dramatic fashion in Fig. 3–2 on page 27. A penny shaped crack on the {111} plane evolved into a hexagonal crack front, because of different crack growth in the ⟨101⟩ and ⟨121⟩ directions. These six fastest crack growth directions (hexagonal corners) were found to be ⟨101⟩ family of slip directions on {111} plane.

Details of the two specimens analyzed are presented in Table 3–1 on page 28. Where,

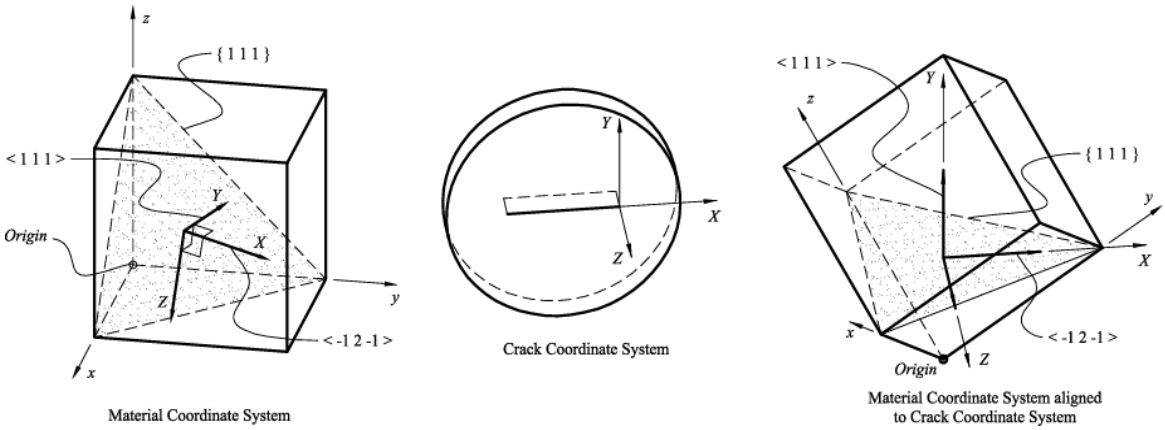

Figure 3–3: Brazilian disk having center crack lying in {111} slip plane and aligned along $\left[\bar{1}2\bar{1}\right]$ direction

Table 3–1: Geometrical and material properties of the two specimens analyzed

Rectangular Specimen - 'A' (Fig. 3–4)				Brazilian Disk - B (Fig. 3–5)			
E	106.2GPa	H	20.32cm	E	106.2GPa	W	2.794cm
G	108.2GPa	W	5.08cm	G	108.2GPa	t	0.254cm
ν	0.4009	t	1.016cm	ν	0.4009	$2a/W$	0.2-0.8
F	4.448KN	$2a/W$	0.1-0.9	F	4.448KN		

$W \rightarrow$ Width or Diameter of the specimen,

$H \rightarrow$ Height of the Specimen,

$t \rightarrow$ Thickness of the specimen,

$F \rightarrow$ Uniaxial load applied,

$\phi \rightarrow$ Angle of inclination between crack and load applied.

Fig. 3–3 on page 28 shows that the crack plane lies on (111) plane and is directed along $\left\langle\bar{1}2\bar{1}\right\rangle$ direction. This slip system has been explained with the help of octahedral slip planes.

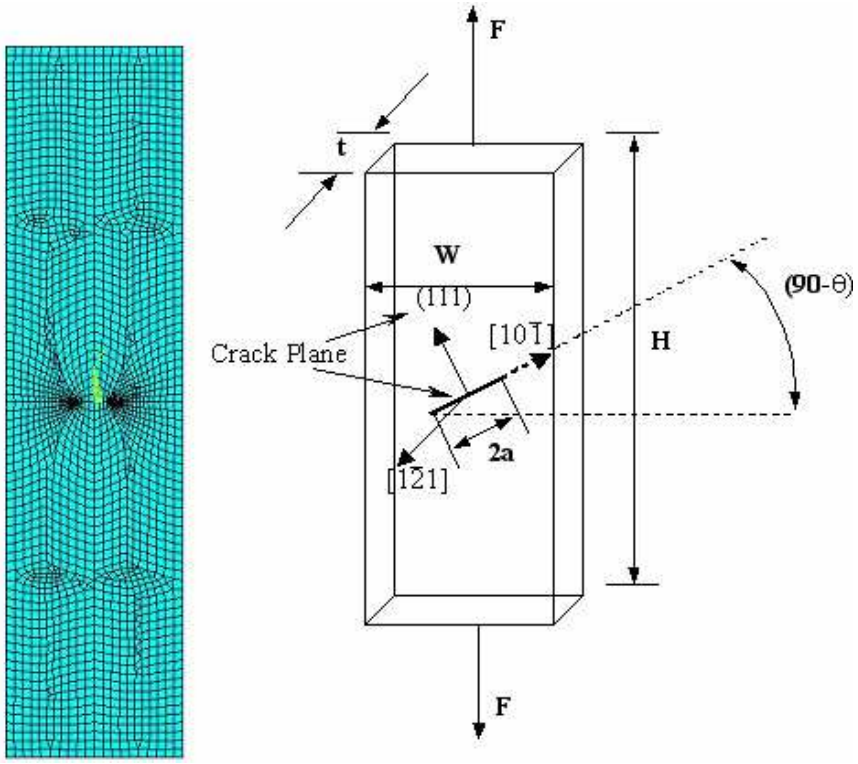

Figure 3–4: Rectangular specimen 'A' meshed with solid95 element (left) and the geometrical details (right)

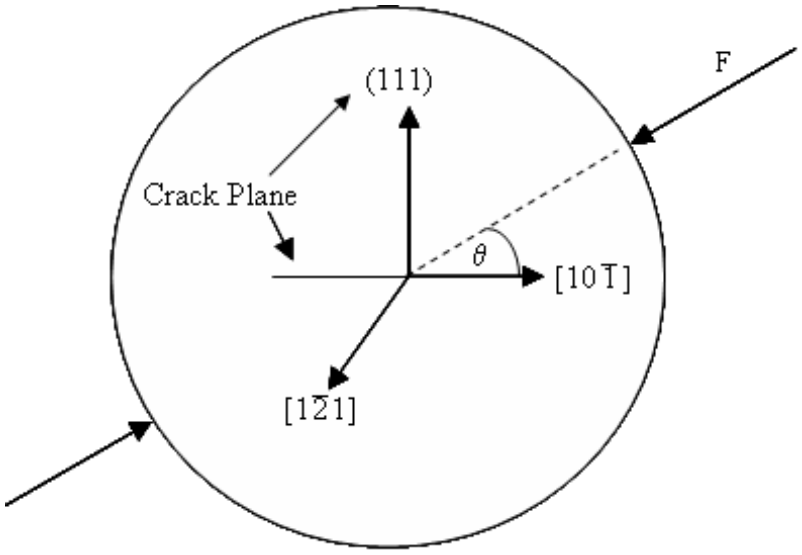

Figure 3–5: Brazilian disk (Specimen 'B') with center crack lying in (111) plane and oriented along $\left[10\bar{1}\right]$ direction

CHAPTER 4
MODELING AND MESHING

In order to study the effect of orthotropy on SIFs, specimens with geometries mentioned in Table 3–1 on page 28 were modeled, meshed and analyzed for different crack lengths, crack angles, material properties and crystal orientations. A rectangular specimen with isotropic properties and without any crack was modeled, and its accuracy was ascertained. A far field stress was calculated analytically and was found to be matched with meshed FEA result. The same model was used with a through thickness center crack and SIF at the crack tip was calculated and verified with standard table.

A Brazilian disk with center crack having isotropic properties was modeled and compared with the SIFs extracted from FEA model. The values were verified with the available tabulated values for the isotropic Brazilian disk. Equation (3.1) was used to calculate the SIFs to verify the equation used by FEM software. As expected, the FEA results were found to be in excellent agreement with published results [26]. The Brazilian disk was selected because of its ability to vary mode mixity at the crack tip by varying load angle 'ϕ'.

The next modeling was done using the orthotropic rectangular specimen with single edge crack and through thickness center crack. The orthotropic stress intensity factors calculated through analytical method were also compared with isotropic results obtained by FEA software. The difference between these results are discussed. Likewise the orthotropic Brazilian disk, with center crack, was modeled and a comprehensive parametric analysis was performed.

The analysis was done for the following cases:

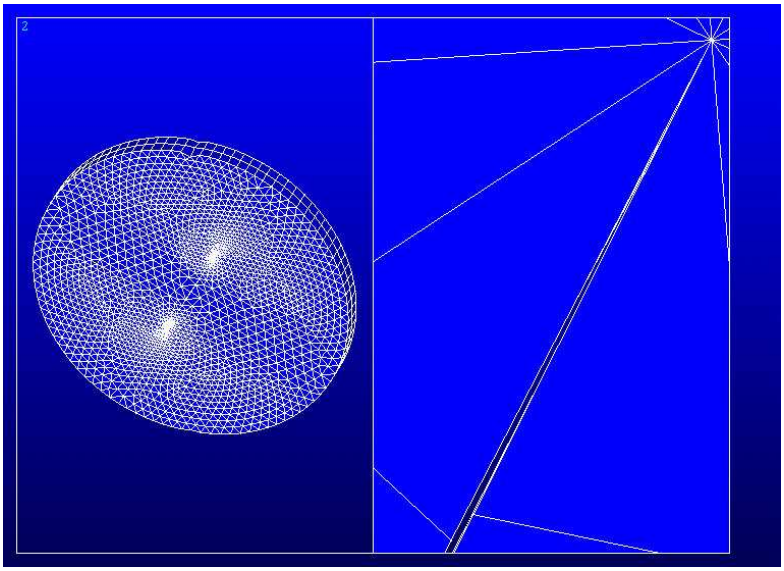

Figure 4–1: Brazilian disk meshed with triangular element having isotropic properties (left) and zoomed view of crack tip (right).

- The model was checked for errors using isotropic $\left(G = \frac{E}{2(1+\nu)}\right)$ and orthotropic $\left(G \neq \frac{E}{2(1+\nu)}\right)$ material properties while keeping all other parameters same;
- The crack length was changed from minimum to maximum in 10 steps;
- The crack angle with the applied force direction was changed from 0^0 to 90^0;
- The material coordinate systems used were $\{111\}\langle 101\rangle$ and $\{111\}\langle 121\rangle$. $\{111\}$ being the crack plane and $\langle 101\rangle$, $\langle 121\rangle$ being the crack growth directions on $\{111\}$ plane (Figs. 3–5 on page 29, 3–3 on page 28).

After defining the geometry of the material in FEA software, free meshing was done on one of the surfaces (front or back), and was swept through the thickness. The mesh density was optimized to save time and effort (Fig. 3–4 on page 29). The crack tip element size was also varied to check the accuracy of the result. Once standardized, the same model was used for various other analyses. The FEA model was meshed using solid95 element (Fig. 4–1), which is a quadratic isoparametric brick element with 8 corner nodes and 12 midside nodes (Fig. 4–2 on page 33). The details of this element have been discussed in the following section.

Crack Tip Element. A number of special crack tip finite elements have been developed applicable to the displacement method, also the hybrid method has been used in developing special crack tip elements. These special crack tip elements contain a singularity off the strain field at the crack tip equal to the theoretical singularity. For two-dimensional geometry the 8-node quadratic isoparametric element can be made to simulate the $1/\sqrt{r}$ singularity in stress. That is done by placing the mid-side nodal coordinates on any side (connected to the crack tip) at the quarter point adjacent to the crack tip [40]. Lynn and Ingraffea [41] have shown computation of SIF for isotropic material with high accuracy can be achieved by placing mid-side nodes between quarter and mid-point of the elements at the crack tip. This information further led to the development of the transition element, which resulted in improved SIF calculations when the ratio of the quarter point element and crack length is decreased.

Quadratic isoparametric elements with 20 nodes have proven to be excellent elements for the calculation of SIF for elastic crack problems [31], when the mid-side nodes are put near the crack tip at the quarter point. Also this element has inverse square root ($\frac{1}{\sqrt{r}}$) singularity, which provides a stress field in agreement with the theoretical stress singularity of linear fracture mechanics. While meshing the model, the size of the element was of significant importance. Tarasovs [42] has shown the effect of quarter point singular and transition element's size on several SIF computation techniques. It was determined that computed SIF was not sensitive to the singular element internal angle and size except for the quarter point displacement technique and the displacement correlation technique. Therefore finer mesh around the crack tip gives better results for the quarter point displacement method.

Two-dimensional triangular elements [30], formed by collapsing one side of rectangular elements, give better results for stress intensity factor. Also, it has

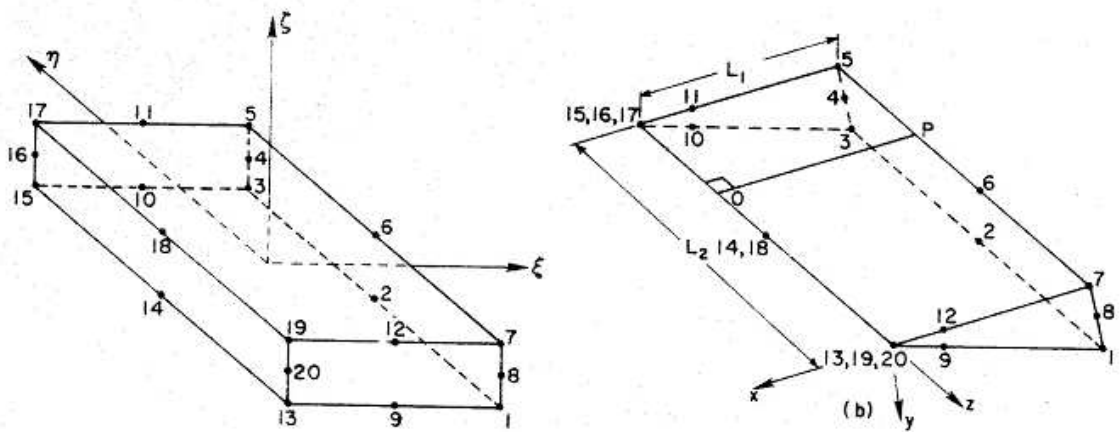

Figure 4–2: (a) 20 node isoparametric element in natural coordinate system and (b) Quarter point singular element with the $\zeta = -1$ face collapsed in local Cartesian coordinate system. [31]

been found that rectangular quadratic isoparametric elements (and brick elements) have singular stiffness (singular total strain energy) at the crack tip [30]. For the three-dimensional case, 20-node isoparametric elements were used. 20-node brick elements collapse and form wedge shaped elements at the crack tip. One of the element faces collapses at the crack tip to form the wedge shape as shown in the Fig. 4–2. Fig. 4–2(a) shows a 20 node isoparametric element in universal coordinate system, and Fig. 4–2(b) depicts its quarter point singular version with the $\xi = -1$ face collapsed in local Cartesian coordinate system.

This element is the best crack tip element for FEA solution of mixed mode SIF analysis of orthotropic materials [24] [42]. Around the crack tip the size of the elements should be very small to reduce the error in calculating SIFs. A typical example of crack tip element length (L_1) is $0.002in$. The enlarged figure of the meshing around the crack tip can be seen in Fig. 4–4 on page 34. All the nodes had to be aligned along the material coordinate system to get the desired result.

Two different orientations $\langle 101 \rangle$ and $\langle 121 \rangle$ (on $\{111\}$ plane) were used to analyze the effect on SIF. The crack lies on the $\{111\}$ plane (Fig. 3–1 on page 24), and the crack direction was aligned along family of either $\langle 101 \rangle$ or $\langle 121 \rangle$ directions.

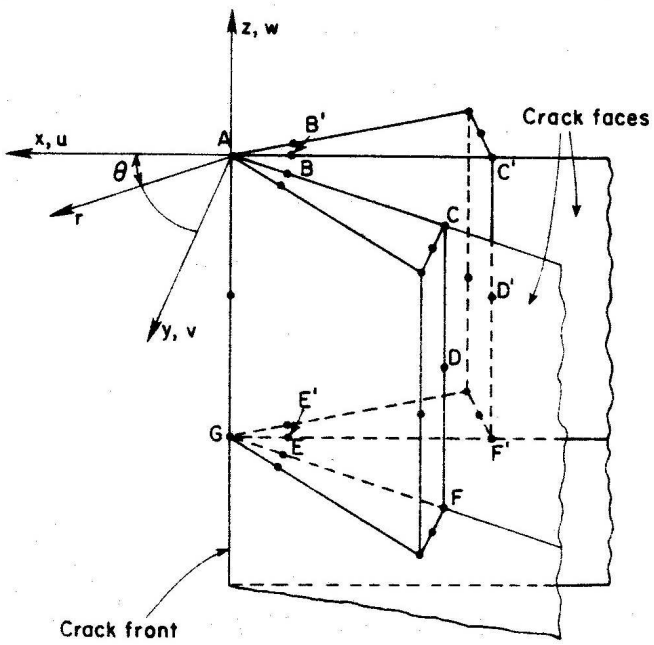

Figure 4–3: Arrangement of quarter-point wedge elements along segment of crack front with nodal lettering convention.[31]

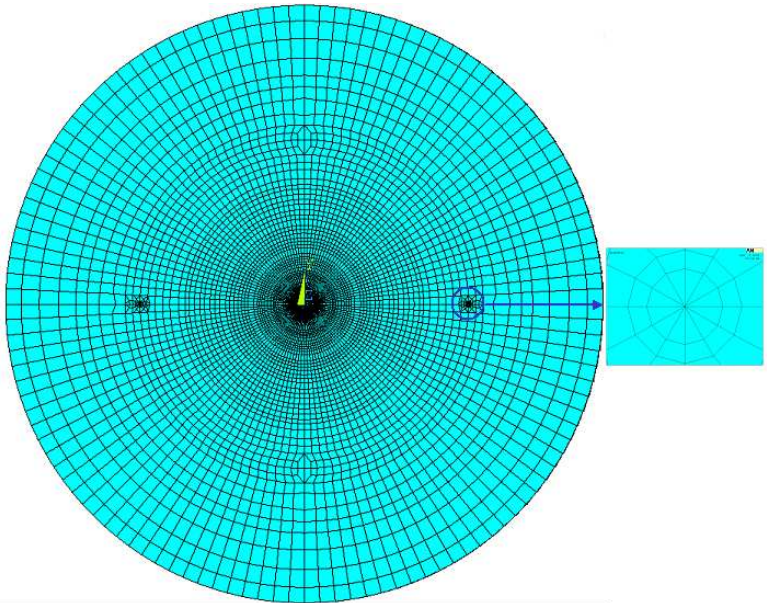

Figure 4–4: The symmetric meshing of BD specimen with solid95 element and enlarged picture of crack tip elements

The resolved shear stress in the direction of $\langle 101 \rangle$ is maximum and in the direction of $\langle 121 \rangle$ is minimum on the $\{111\}$ plane as the Schmid's factor is maximum along $\langle 101 \rangle$ and minimum along $\langle 121 \rangle$ direction. Since the maximum and minimum resolved shear stress occur along the $\langle 101 \rangle$ and $\langle 121 \rangle$ directions respectively, these directions are a family of primary or 'easy slip' directions and secondary or 'hard slip' directions, on the $\{111\}$ plane.

CHAPTER 5
MIXED MODE SIF: RESULTS AND DISCUSSION

Calculation of SIF for anisotropic materials is a crucial step in order to predict the FCG behavior of single crystal superalloys. The numerical procedure developed here is not merely specific to the FCC single crystal. It can also be used for computing the SIF for any generalized anisotropic material subject to mixed mode loading. The displacements, calculated using FEA, were applied to the SIF model developed for the anisotropic material (in our case, orthotropic material). It is evident from equations (3.2) and (3.3), that the calculated SIFs are a function of the crack tip nodal displacements, which are a function of the stresses developed around the crack tip, which in turn are a function of the applied force, geometry of the specimen and the orientation of the material coordinate system with respect to the crack coordinate system.

The length of the rectangular specimen (Specimen 'A') was sufficiently long in comparison to the thickness and width of the specimen, thus yielding a uniform far field stress. Therefore, a plane strain assumption was used in equation (3.10) in order to calculate the SIF at the mid plane of the rectangular specimen. The validity of the model was first checked with isotropic material properties. The analytical model resulted in K_I, K_{II} and K_{III} values, which were identical to the FEA results based on isotropic assumptions.

After verifying the model, the effect of change in ratio (from 10% to 80%) of crack length and width ($2a/W$) was examined on SIFs for specimen 'A' (Fig. 3–4 on page 29). The normalized values of SIFs have not been used because the Fracture toughness, K_c, for the given material is not characterized unambiguously, as a function of orientation. For both of the above mentioned orientations, a

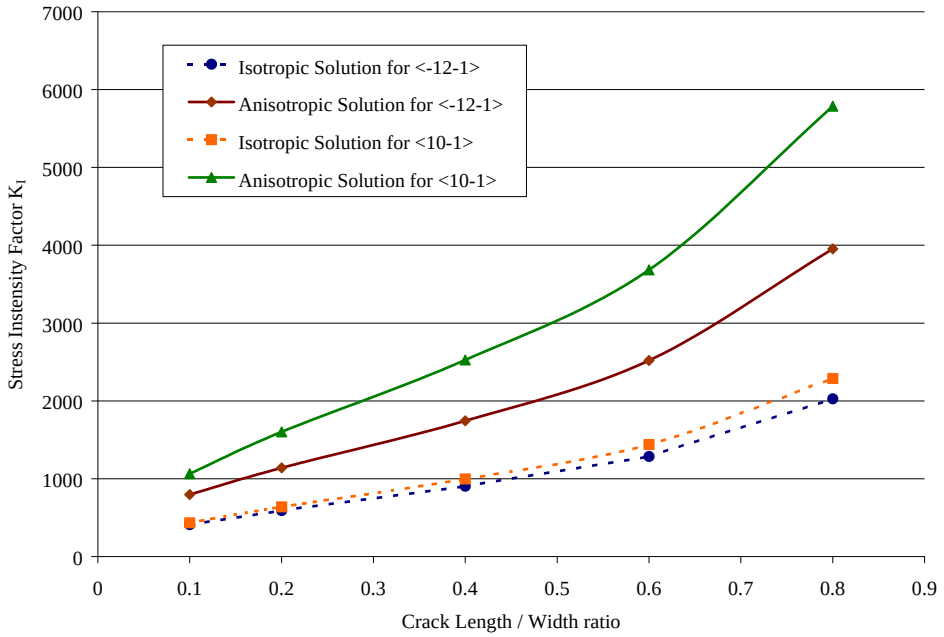

Figure 5–1: K_I versus Crack Length/Width ratio for $\left[10\bar{1}\right]$ and $\left[\bar{1}2\bar{1}\right]$ orientation of Specimen 'A' at $\phi = 0^0$.

gradual increase in K_I was observed with an increase in the $2a/W$ ratio. Also the values of K_I for the $\left[10\bar{1}\right]$ orientation were always found to be greater than the corresponding values for the $\left[\bar{1}2\bar{1}\right]$ orientation (Fig. 5–1 on page 37), at the same far field stress. The same trend was also observed for K_{II}, though the values were very small for both the orientations (Fig. 5–2 on page 38). This is because the loading is normal to the (111) plane, thus inducing zero shear in the plane of the crack. Therefore K_{II} is expected to be very small and within the numerical calculation error. The values of K_{III} for the $\left[10\bar{1}\right]$ orientation are negative (Fig. 5–3 on page 38) because the relative displacement of the two crack faces along the z-direction (Fig. 4–3 on page 34) was negative. This is simply a consequence of sign convention definition. However, the magnitude of the SIF for $\left[10\bar{1}\right]$ is found to be greater than for $\left[\bar{1}2\bar{1}\right]$. This validates that the $\langle 101 \rangle$ family of slip directions are primary or easy slip directions as compared to those of $\langle 121 \rangle$.

The change in SIFs with the crack angle 'ϕ' was analyzed for both orientations. K_I decreases for both orientations with increasing crack angle as is evident

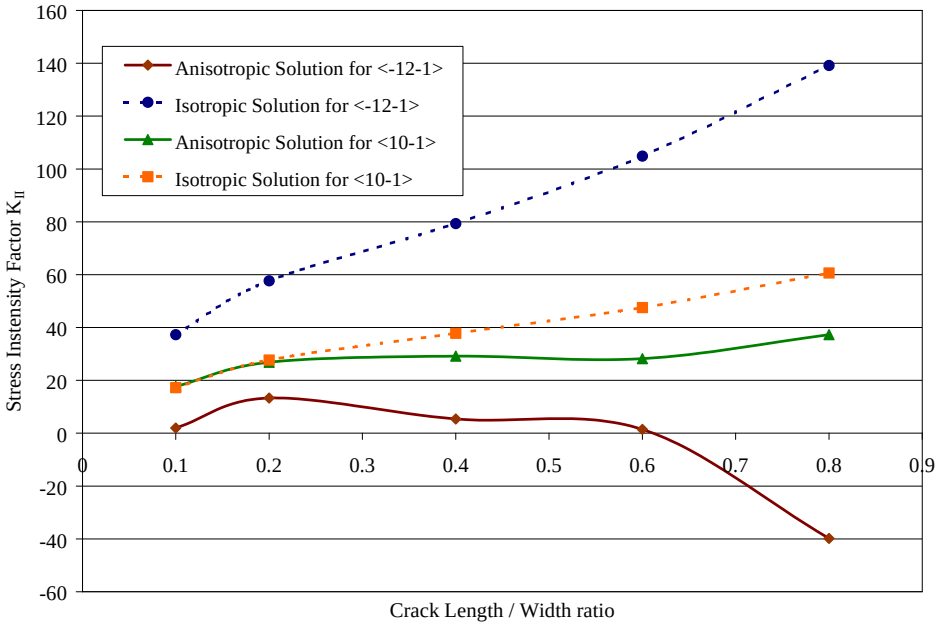

Figure 5–2: K_{II} versus Crack Length/Width ratio for $[10\bar{1}]$ and $[\bar{1}2\bar{1}]$ orientation of Specimen 'A' at $\phi = 0^0$.

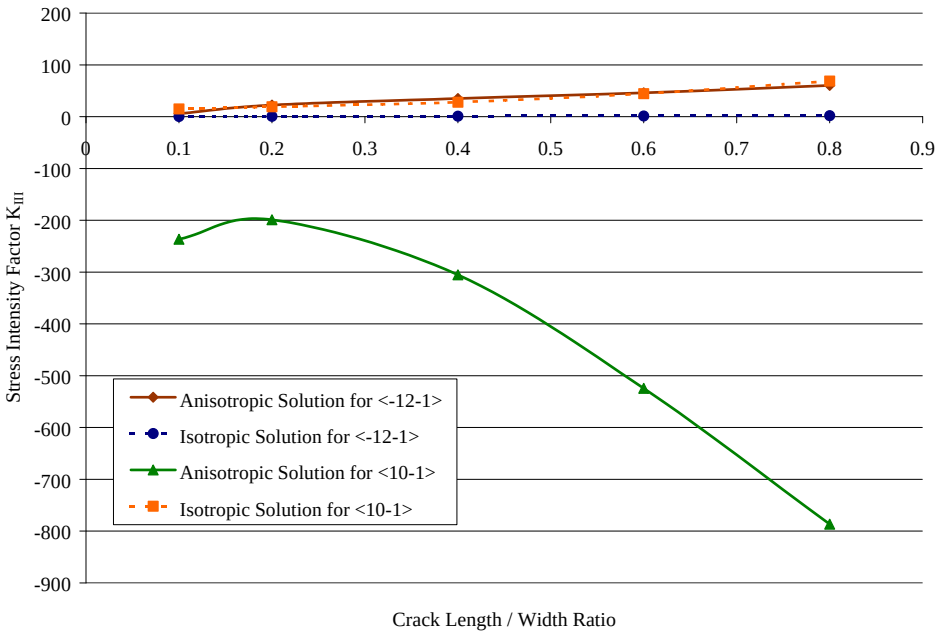

Figure 5–3: K_{III} versus Crack Length/Width ratio for $[10\bar{1}]$ and $[\bar{1}2\bar{1}]$ orientation of Specimen 'A' at $\phi = 0^0$.

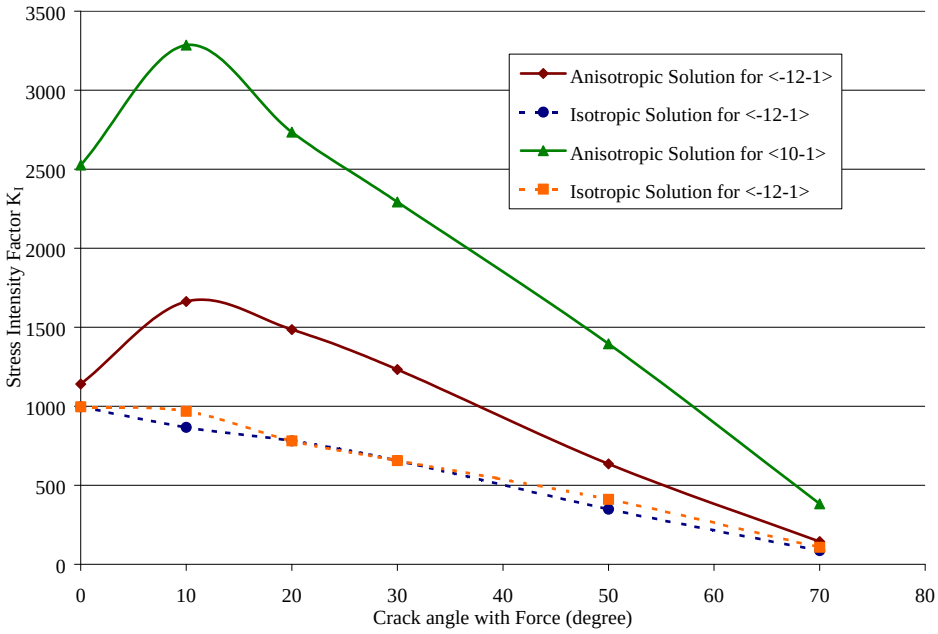

Figure 5–4: K_I versus crack angle with force for $[10\bar{1}]$ and $[\bar{1}2\bar{1}]$ orientation of Specimen 'A' at $2a/W = 0.4$.

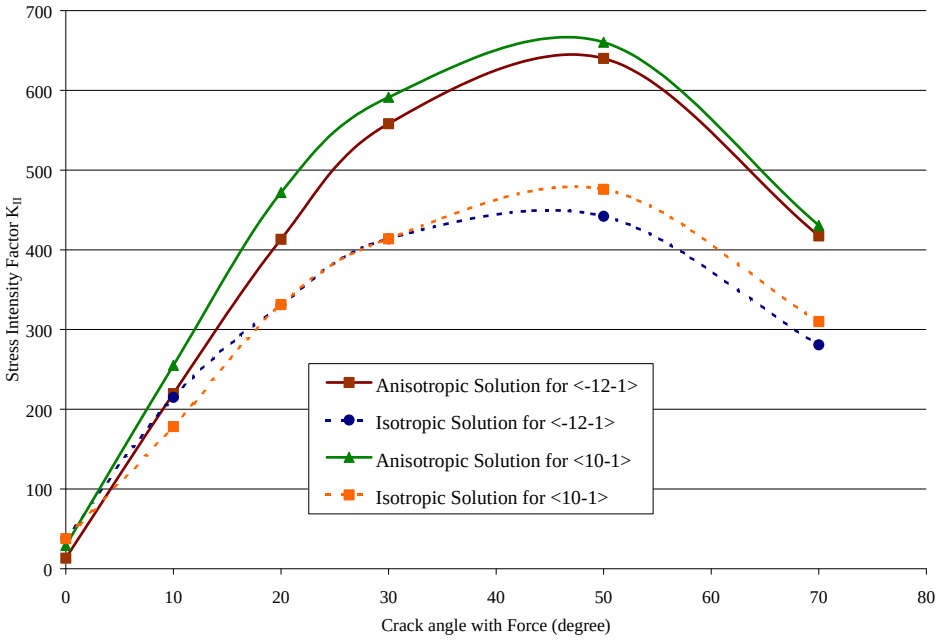

Figure 5–5: K_{II} versus crack angle with force for $[10\bar{1}]$ and $[\bar{1}2\bar{1}]$ orientation of Specimen 'A' at $2a/W = 0.4$.

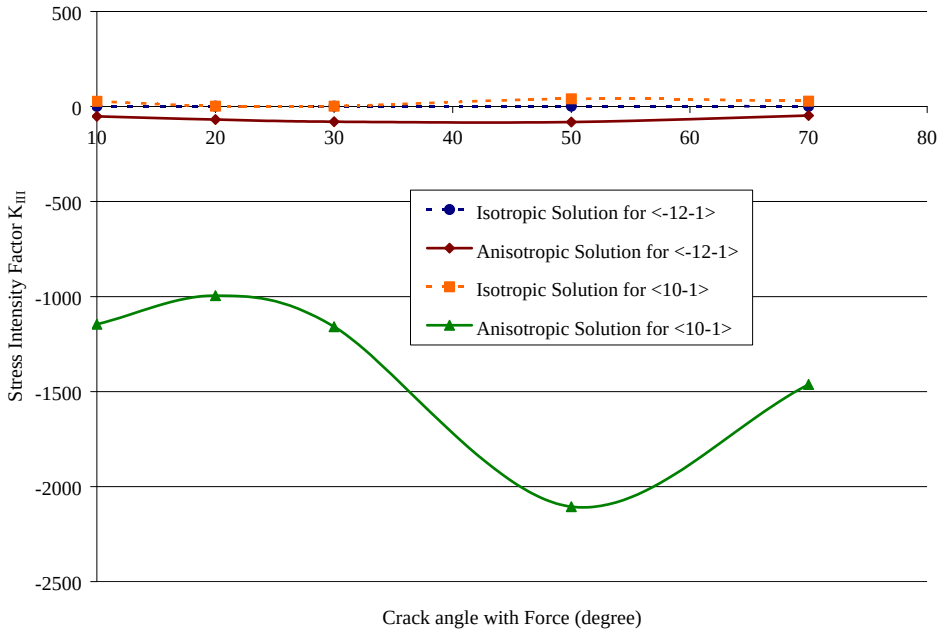

Figure 5–6: K_{III} versus crack angle with force for $[10\bar{1}]$ and $[\bar{1}2\bar{1}]$ orientation of Specimen 'A' at $2a/W = 0.4$.

from the plots (Fig. 5–4 on page 39), but the value of K_I is always greater for $[10\bar{1}]$ than that for the $[\bar{1}2\bar{1}]$ orientation. For isotropic material, K_I becomes zero upon crack closure at a certain angle. For an orthotropic material, it can be seen that K_I is still nonzero due to the coupling of the nodal displacements. The value of K_{II} initially increases with an increase in ϕ due to an increase in shear stress, which after reaching a maximum value starts decreasing (Fig. 5–5 on page 39). The value of K_{III} for the $[10\bar{1}]$ orientation is negative (Fig. 5–6 on page 40) as the relative nodal displacements of the crack faces along the z-direction were negative. However, it was observed that the magnitude of K_{III} for $[10\bar{1}]$ was always greater than for the $[\bar{1}2\bar{1}]$ orientation.

From the Brazilian Disk specimen (Specimen 'B'), it can be seen that the magnitude of SIF for the $[10\bar{1}]$ orientation is always greater than the corresponding values of the $[\bar{1}2\bar{1}]$ orientation, thus enabling a crack to move faster on the $[10\bar{1}]$ plane than on the $[\bar{1}2\bar{1}]$ plane (Figs. 5–7, 5–8 on page 42, 5–9, 5–10 on page 43, 5–11, 5–12 on page 44), under fatigue loading for same $\triangle K$ values. Even though

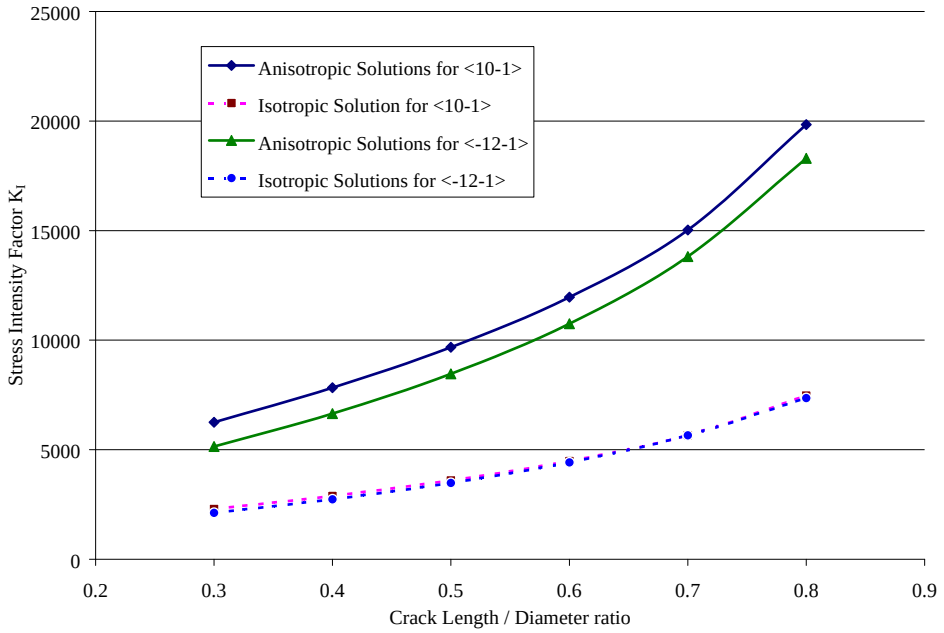

Figure 5–7: K_I versus Crack Length/Diameter ratio for $[10\bar{1}]$ and $[\bar{1}2\bar{1}]$ orientation of Specimen 'B' at $\phi = 0^0$.

the magnitude of K_{II} for the $[\bar{1}2\bar{1}]$ orientation is greater than that for the $[10\bar{1}]$ orientation, it may not affect the effective SIF very much, as the magnitude of K_{III} for the $[10\bar{1}]$ orientation is far greater than that for the $[\bar{1}2\bar{1}]$ orientation.

The values of K_I for the $[10\bar{1}]$ orientation rapidly decrease as compared to the $[\bar{1}2\bar{1}]$ orientation and reach crack closure angle at around 18^0, whereas the crack closure angle is 30^0 for the $[\bar{1}2\bar{1}]$ orientation. The magnitude of K_{II} for $[\bar{1}2\bar{1}]$ is always greater than that for the $[10\bar{1}]$ orientation, but the difference is far less in comparison to the magnitude of K_{III} for the $[\bar{1}2\bar{1}]$ and $[10\bar{1}]$ orientations. Following the work of Sauma and Sikiotis [31], the calculated values for K_{III} were found to be negligible and after much analysis and rederiving of relevant equations, the equation given by Sauma and Sikiotis was found to be wrongly formulated. On the other hand, equation (3.5) correctly gave rise to all the three modes of SIFs. As a result of the coupling of displacements at the crack tip due to anisotropy, non-negligible values of K_{III} were found, and they varied with respect to the applied force, crack length and crack angle.

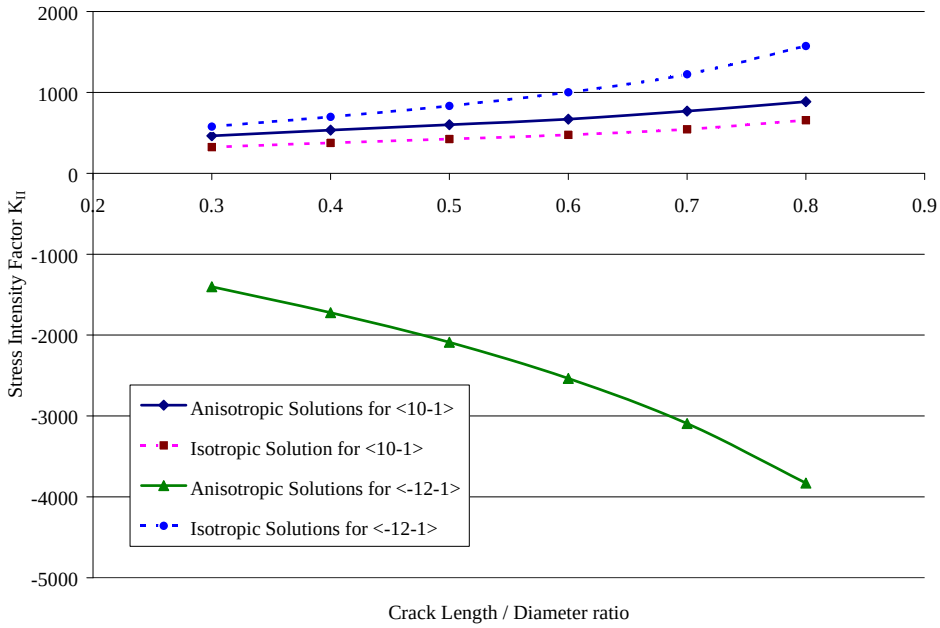

Figure 5–8: K_{II} versus Crack Length/Diameter ratio for $[10\bar{1}]$ and $[\bar{1}2\bar{1}]$ orientation of Specimen 'B' at $\phi = 0^0$.

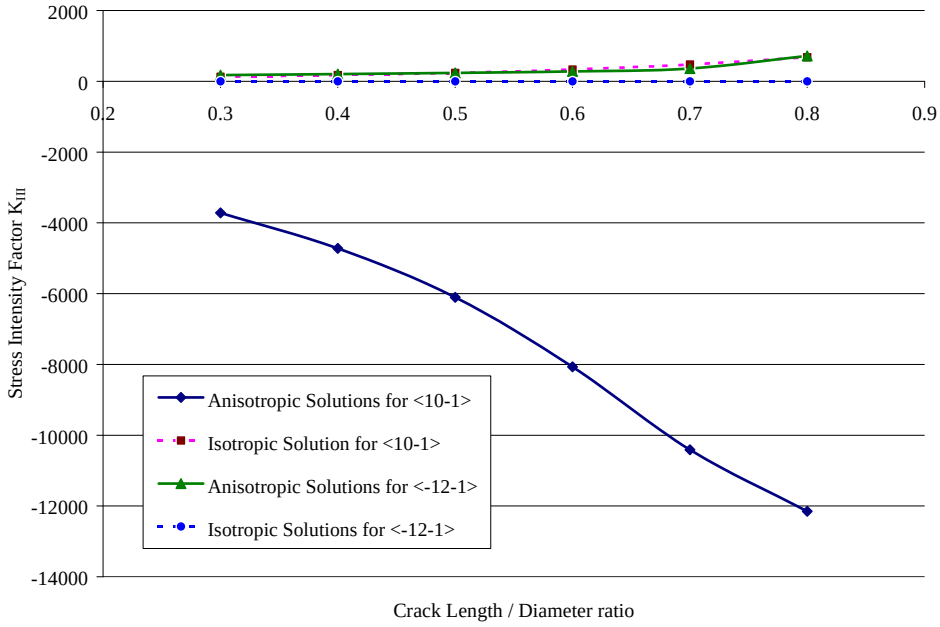

Figure 5–9: K_{III} versus Crack Length/Diameter ratio for $[10\bar{1}]$ and $[\bar{1}2\bar{1}]$ orientation of Specimen 'B' at $\phi = 0^0$.

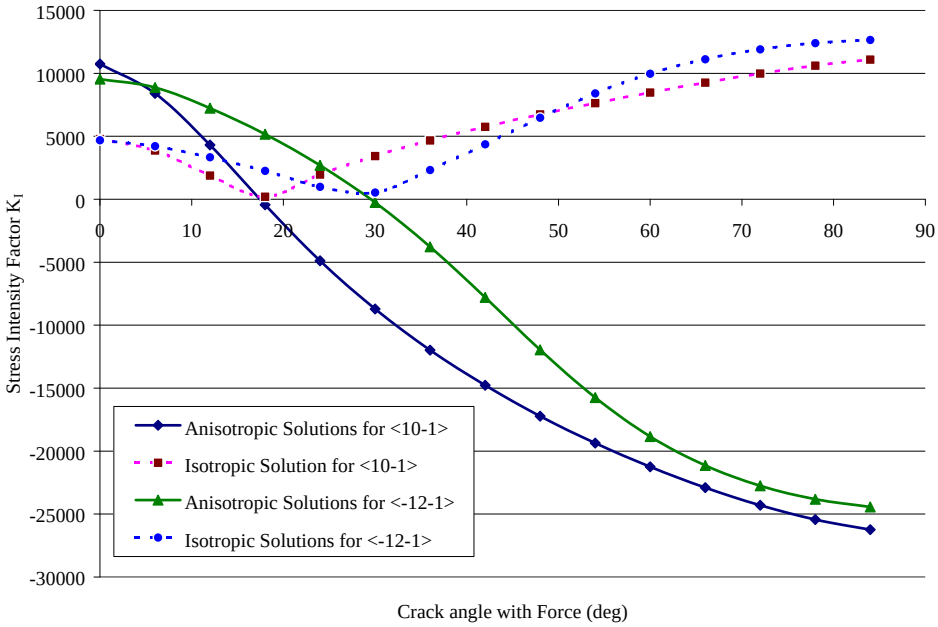

Figure 5–10: K_I versus crack angle with force for $[10\bar{1}]$ and $[\bar{1}2\bar{1}]$ orientation of Specimen 'B' at $2a/W = 0.55$.

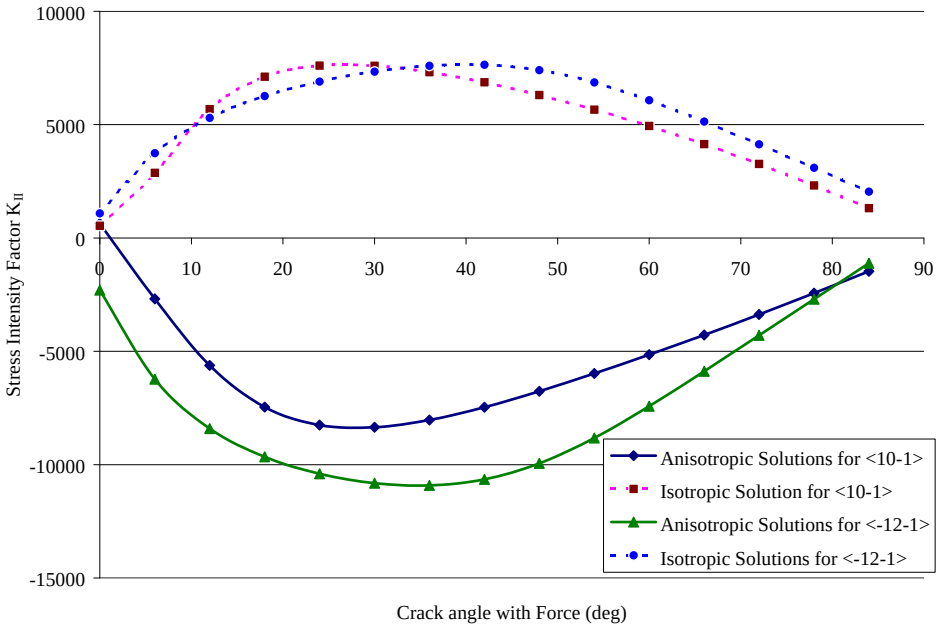

Figure 5–11: K_{II} versus crack angle with force for $[10\bar{1}]$ and $[\bar{1}2\bar{1}]$ orientation of Specimen 'B' at $2a/W = 0.55$.

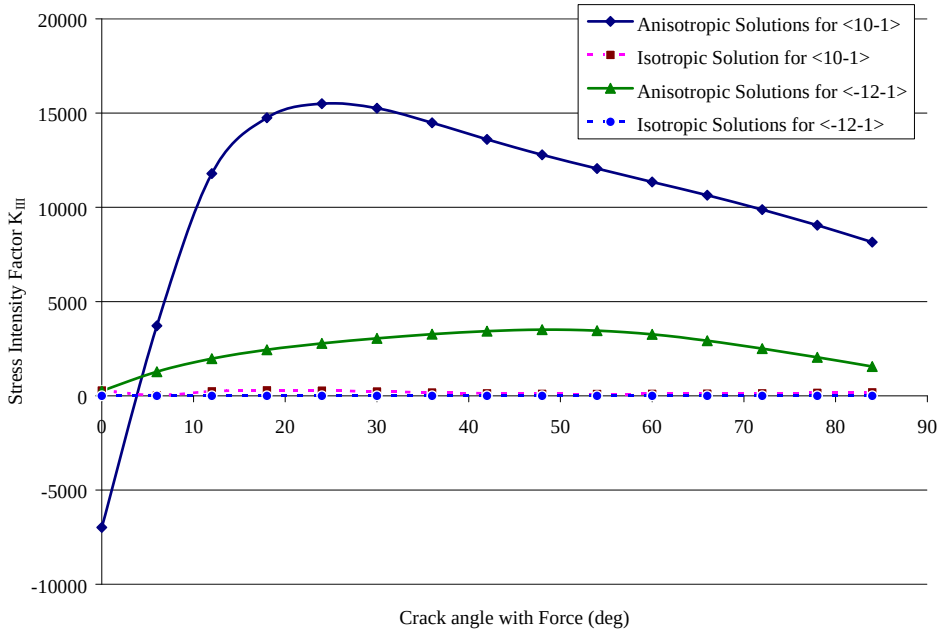

Figure 5–12: K_{III} versus crack angle with force for $[10\bar{1}]$ and $[\bar{1}2\bar{1}]$ orientation of Specimen 'B' at $2a/W = 0.55$.

The BD specimen SIFs (K_I, K_{II} and K_{III}) were further analyzed along the thickness for the $[10\bar{1}]$ and $[\bar{1}2\bar{1}]$ crack orientations with change in crack length and crack angle. They were calculated at 5 different points along the thickness at the crack front as shown in the Fig. 5–13 on page 45. A plane stress assumption was made at the surface of the BD specimen (Plane 1 & 5) and a plane strain assumption was made at all the interior points (Plane 2, 3 & 4).

In order to check the difference in SIF of isotropic BD specimen and orthotropic BD specimen with change in load angle with crack, under similar loading condition and specimen geometry, two models were analyzed. The orthotropic BD specimen analyzed had the material coordinate system aligned with specimen coordinate system. Therefore a symmetry was expected in the SIF values across the thickness (Figs. 5–15 on page 47, 5–17 on page 48, 5–19 on page 49). For isotropic material, properties of pure nickel was used. The trends of K_I, K_{II} and K_{III}, because of change in force angle with crack, for orthotropic BD specimen and isotropic BD specimen were found to be similar, but the magnitude of SIFs

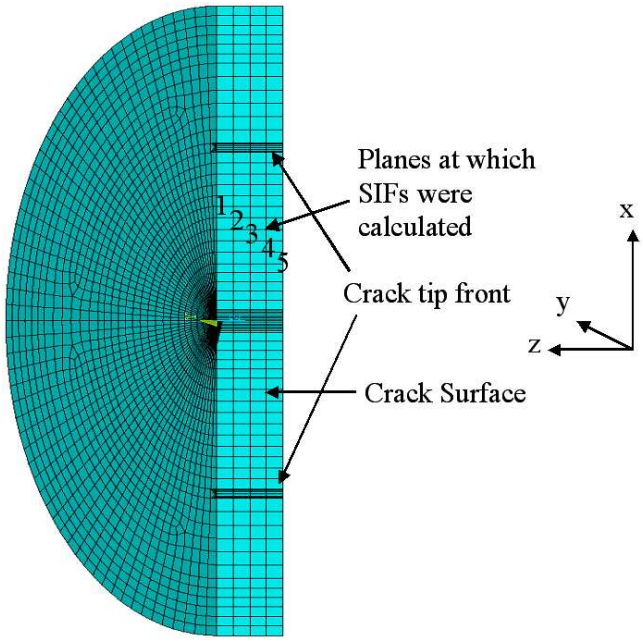

Figure 5–13: Half meshed model of Brazilian disk specimen and the crack coordinate system

for both the specimen were significantly different, because of the material properties. The crack closure angle was the same ($\sim 20^0$, Figs. 5–14, 5–15 on page 47). Negative K_I was found because no contact elements were used at the crack interface. After reaching the crack closure angle, further increase in force angle lead to penetration of crack faces, resulting in negative K_I. At the edges, K_I was less than that towards mid-plane (Figs. 5–14, 5–15 on page 47). $K_{I,max}$ was found to be 12 Kpsi$\sqrt{in}$ for orthotropic BD specimen, whereas it was less than 10 Kpsi$\sqrt{in}$ for isotropic BD specimen. The values of K_{II} can be seen to be negative because of the sign convention followed at the crack tip coordinate system (Fig. 5–13 on page 45, 6–4 on page 64). The absolute value of K_{II} reached maximum at $\sim 30^0$ for both the specimens(Figs. 5–16, 5–17 on page 48), then starts slowly decreasing towards zero. The absolute $K_{II,max}$ was 18 Kpsi$\sqrt{in}$ for orthotropic BD specimen, whereas it was 14 Kpsi$\sqrt{in}$ for isotropic BD specimen. The variation of K_{II} across the thickness was more distinguished for the orthotropic case than for the isotropic specimen (Fig. 5–16, 5–17 on page 48). Higher K_{III} values were observed for the

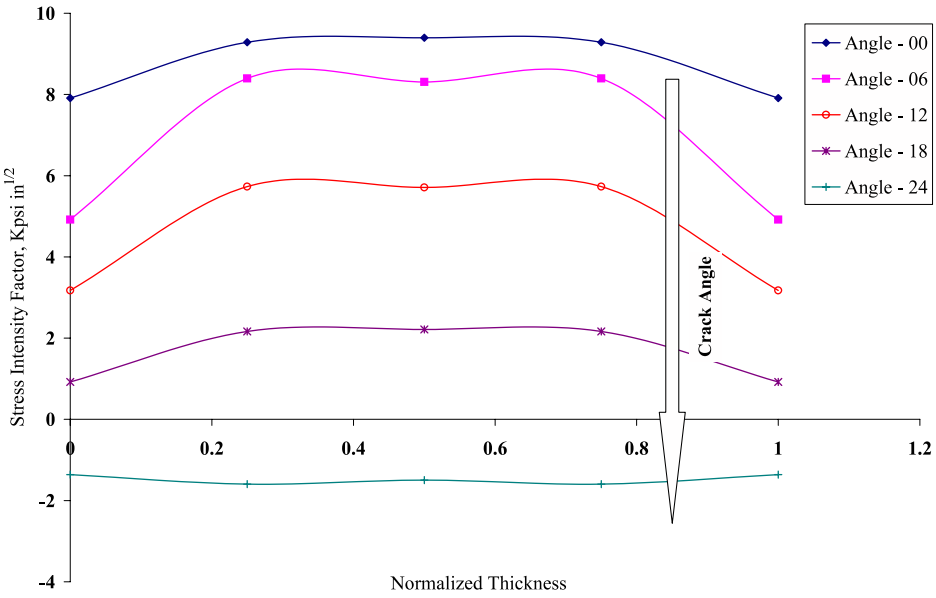

Figure 5–14: Variation of SIF K_I along isotropic BD specimen thickness at different Crack angle.

orthotropic specimen than for isotropic specimen (Figs. 5–18, 5–19 on page 49). For load aligned with crack plane, K_{III} was found to be zero across the thickness. Since K_{III} is a function of out of plane relative displacements (normal to the disk plane) of nodes at the crack tip and because of perfect symmetry in loading and geometry of the material, it ought to zero. But as the force angle was introduced, because of poisson's effect, there were small out of plane relative displacements on both sides of the mid plane of the disk (plane 3, Fig. 5–13 on page 45), which was equal and opposite to each other. The absolute value of K_{III} reaches maximum between 30^0-36^0 and it is $\sim 15Kpsi\sqrt{in}$ for isotropic and $\sim 22Kpsi\sqrt{in}$ for orthotropic specimen. Among all the SIFs K_{III} is more dominant at the crack edges at higher force angles, whereas it is zero at the midplane for all the angles (Figs. 5–18, 5–19 on page 49). The average value of K_{III} is zero across the thickness for both specimen.

From Figs. 5–21, 5–22 on page 52, it can be seen that K_I decreases with an increase in crack angle and crack closure angle (where K_I is almost zero) was

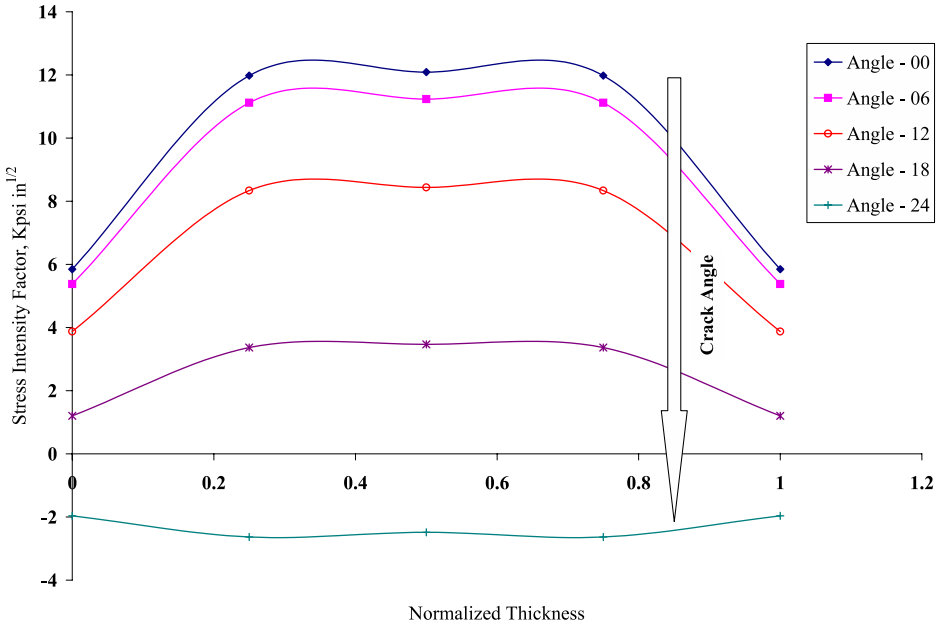

Figure 5–15: Variation of SIF K_I along orthotropic BD specimen thickness at different Crack angle.

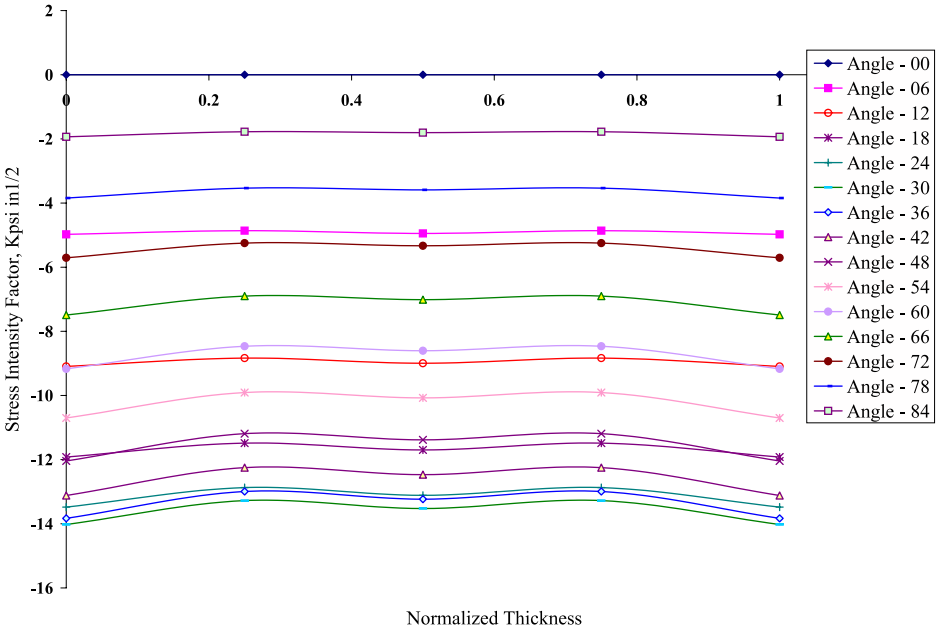

Figure 5–16: Variation of SIF K_{II} along isotropic BD specimen thickness at different Crack angle.

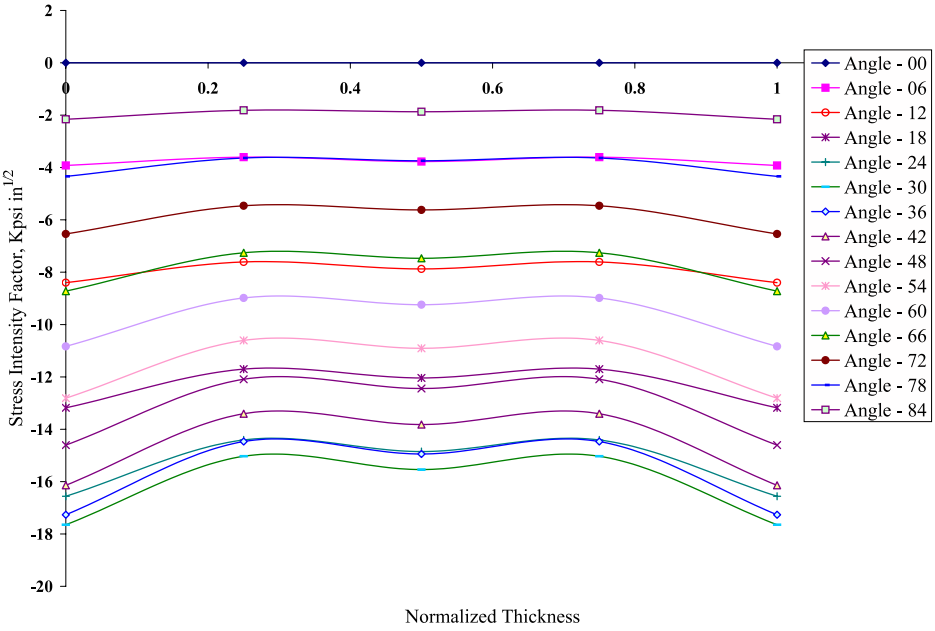

Figure 5–17: Variation of SIF K_{II} along orthotropic BD specimen thickness at different Crack angle.

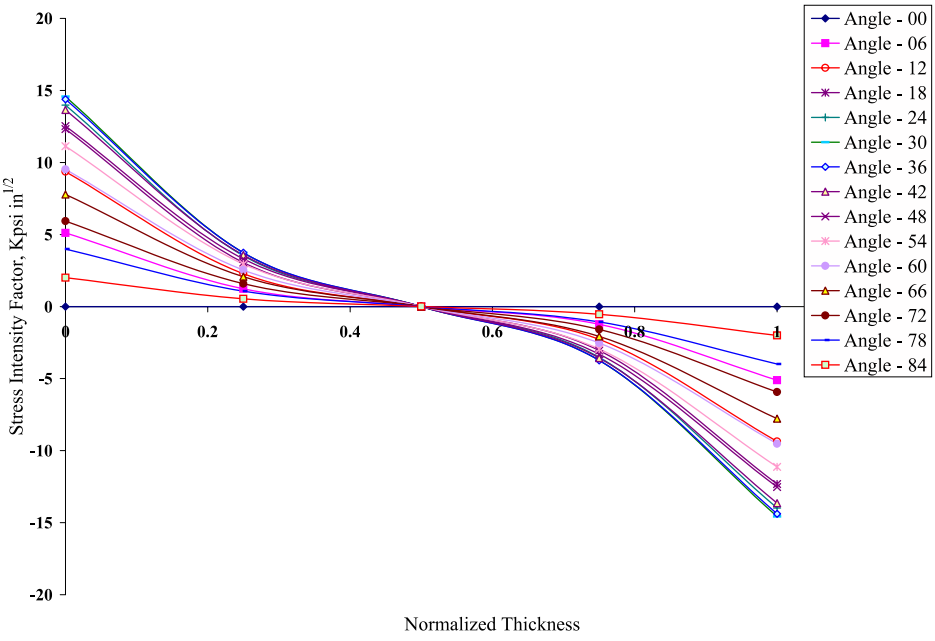

Figure 5–18: Variation of SIF K_{III} along isotropic BD specimen thickness at different Crack angle.

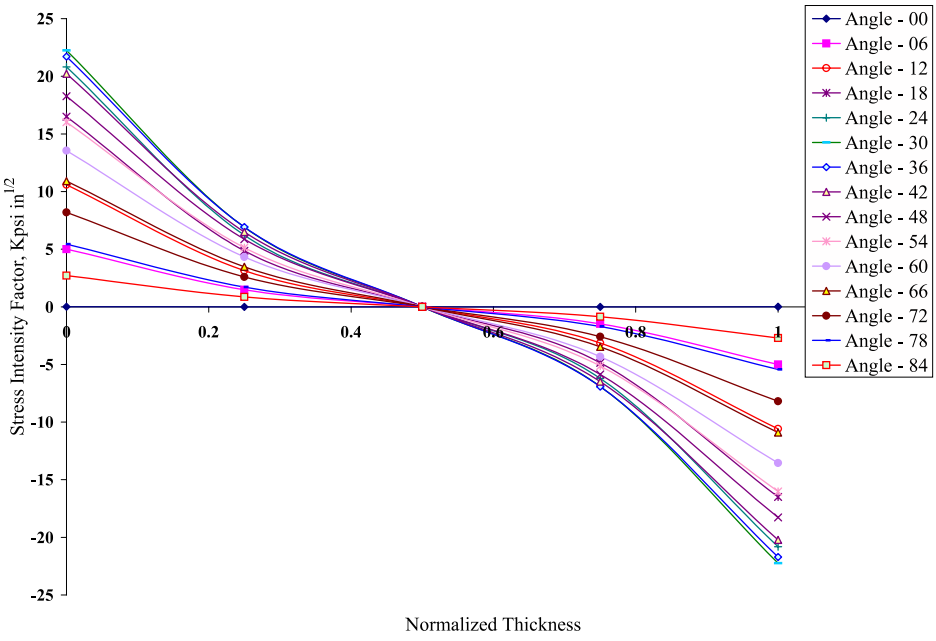

Figure 5–19: Variation of SIF K_{III} along orthotropic BD specimen thickness at different Crack angle.

reached at $\sim 18^0$ for the $[10\bar{1}]$ orientation, whereas it was $\sim 30^0$ for the $[\bar{1}2\bar{1}]$ orientation, as was observed by Fig. 5–10 on page 43. K_I can be seen symmetric for $[\bar{1}2\bar{1}]$ orientation across the thickness, whereas it is not for the case of $[10\bar{1}]$ orientation. In general K_I inside the surface, (plane 2, 3, 4, Fig. 5–13 on page 45) is always greater than those at the crack edges (plane 1, 5, Fig. 5–13). The absolute value of K_{II} increases and becomes maximum at an angle $\sim 24^0$ for the $[10\bar{1}]$ orientation, whereas for the $[\bar{1}2\bar{1}]$ orientation it is $\sim 36^0$ (Figs. 5–23, 5–24 on page 53), as also illustrated in Fig. 5–11 on page 43. K_{II} then starts slowly decreasing with further increases in crack angle, as was observed in Fig. 5–11. It can be seen that at one of the faces (Plane 1, thickness = 0; Fig. 5–21 on page 52), absolute values of K_I are always greater than those at the other face (Plane 5, thickness = 1) of the BD specimen for the $[10\bar{1}]$ orientation. But absolute values of K_{II} (Fig. 5–23 on page 53) are always greater at Plane 5, than those at Plane 1 for the $[10\bar{1}]$ orientation. It is interesting to observe that SIFs (Figs. 5–22 on page 52, 5–24 on page 53, 5–26 on page 54)(K_I, K_{II} and K_{III}) are symmetric

about the mid plane for the $\left[\bar{1}2\bar{1}\right]$ orientation. This is due to symmetry observed for the crack lying along $\langle 121\rangle$ direction than for that lying along $\langle 101\rangle$ direction on $\{111\}$ plane as shown in Fig. 5–20. But unlike the orthotropic specimen aligned

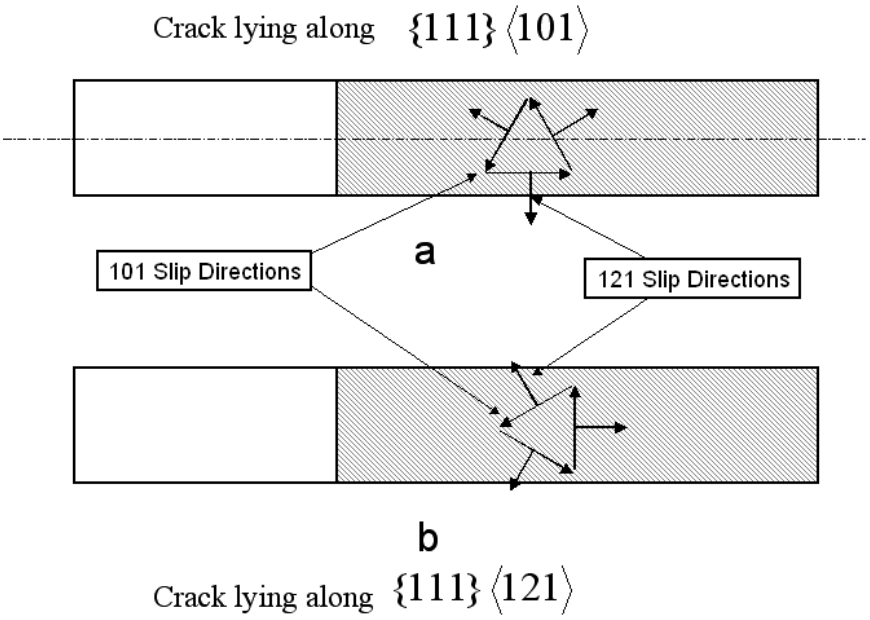

Figure 5–20: a)Unsymmetry about mid plane for crack oriented along $\{111\}\langle 101\rangle$; b) Symmetry for crack lying along $\{111\}\langle 121\rangle$

to specimen coordinate system, crack closure happens much later ($\sim 30^0$). The variation of K_I across the thickness is small. In Fig. 5–26 on page 54 K_{III} shows a response similar to isotropic BD specimen (Fig. 5–18 on page 48) as the value of maximum K_{III} is almost the same ($\sim 14.5Kpsi\sqrt{in}$). But where K_{III} is maximum at an angle $\sim 36^0$ for the isotropic specimen, it is at an angle of $\sim 48^0$ for the $\left[\bar{1}2\bar{1}\right]$ orientated BD specimen, as can be clearly seen in Fig. 5–12 on page 44. The values of K_{III} (Fig. 5–25 on page 54) for the $\left[10\bar{1}\right]$ orientation at one of the faces (Plane 1, thickness = 0) is always greater than those at the other face (Plane 5, thickness = 1) and reaches maximum at an angle 30^0-36^0, same as isotropic and orthotropic specimen, but the value is far greater ($\sim 65Kpsi\sqrt{in}$) as compared to isotropic ($\sim 15Kpsi\sqrt{in}$) or orthotropic ($\sim 22Kpsi\sqrt{in}$) specimen. The max value of K_{III}

shown in Fig. 5–12 on page 44 is at $\sim 25^0$, because the values were calculated at an offset to the midplane, which can be verified from the offset value taken from Fig. 5–25 on page 54.

With increase in crack length/diameter ratio, at 0^0 crack angle, the value of K_I, for $\left[10\bar{1}\right]$ and $\left[\bar{1}2\bar{1}\right]$ orientations, increases throughout the thickness (Figs. 5–27, 5–28 on page 55 and 5–7 on page 41). The profile of K_I is more distinguished with increase in crack length in Fig. 5–27 on page 55, whereas in Fig. 5–28 on page 55, K_I is almost uniform across the thickness of the specimen. But with increase in crack length, K_I at the crack edges becomes more than K_I values inside the specimen, unique to $\left[\bar{1}2\bar{1}\right]$ orientation. The value of K_{II} on the other hand increases for the $\left[10\bar{1}\right]$ orientation (Fig. 5–29 on page 56) and decreases for $\left[\bar{1}2\bar{1}\right]$ orientation (Fig. 5–30 on page 56) with increase in crack length/diameter ratio as illustrated in Fig. 5–8 on page 42. Where K_{II} is symmetric for the $\left[10\bar{1}\right]$ orientation, it decreases across thickness for the $\left[10\bar{1}\right]$ orientation and becomes negative. Also, it is interesting to observe that the value of K_{II} does not change at thickness$\sim$ 0.9 with change in crack length. K_{III} for the $\left[10\bar{1}\right]$ orientation (Fig. 5–31 on page 57) was found to be continuously decreasing, except at thickness = 1, with increase in crack length/diameter ratio (can be clearly seen in Fig. 5–9 on page 42). For the $\left[\bar{1}2\bar{1}\right]$ orientation (Fig. 5–32 on page 57), K_{III} is symmetric across the thickness all the time (because of the symmetry about the mid plane, as shown in Fig. 5–20 on page 50) and it increases in value with increase in crack length/width ratio. At the midplane it is always zero, which means that there is no out of plane displacement at the midplane.

Using the above analysis we can find the profile of the crack growth inside a specimen, which can be crucial for the life assessment of an anisotropic material.

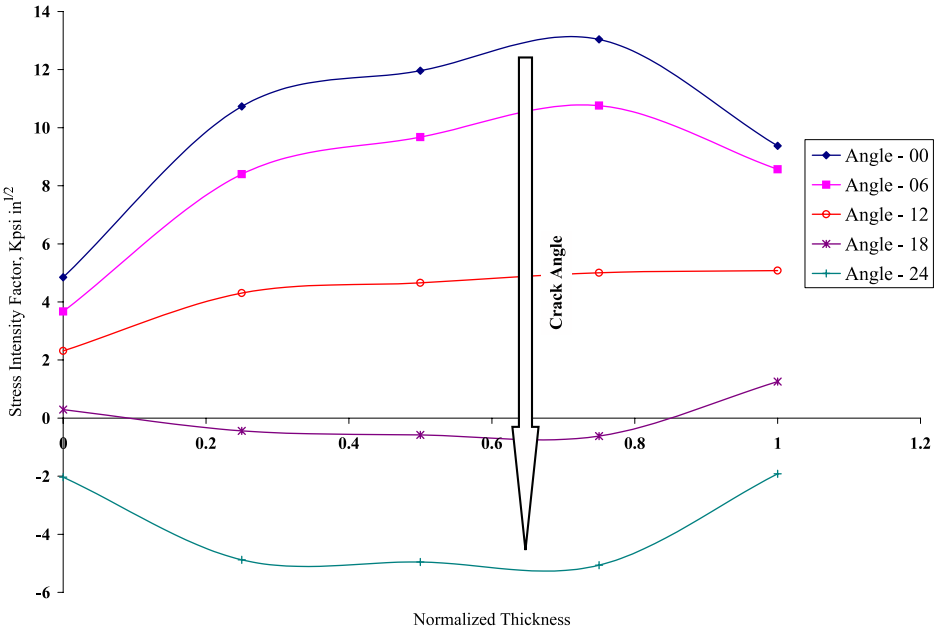

Figure 5–21: Variation of SIF K_I along BD specimen thickness at different Crack angle for $[10\bar{1}]$ orientation.

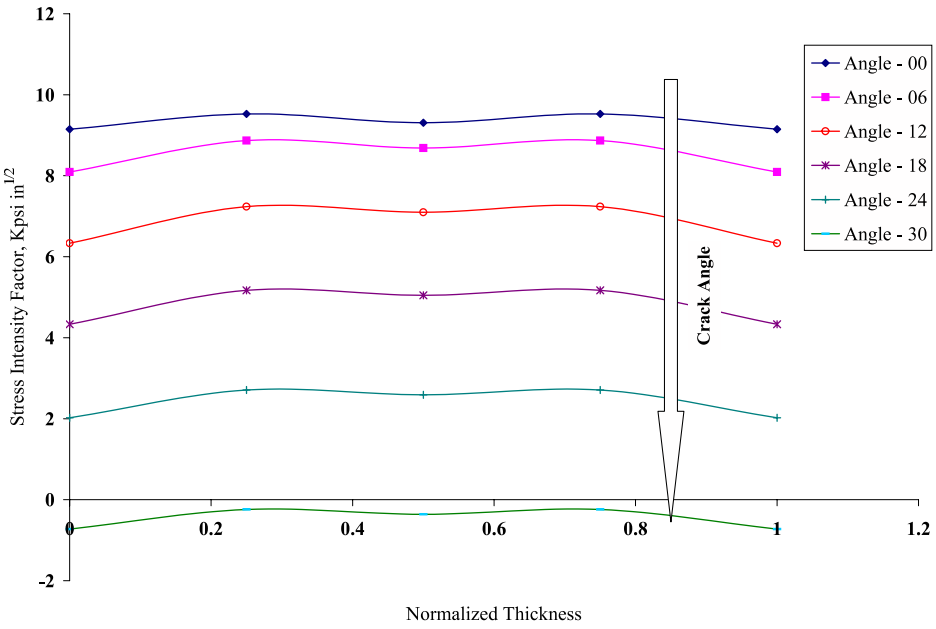

Figure 5–22: Variation of SIF K_I along BD specimen thickness at different Crack angle for $[\bar{1}2\bar{1}]$ orientation.

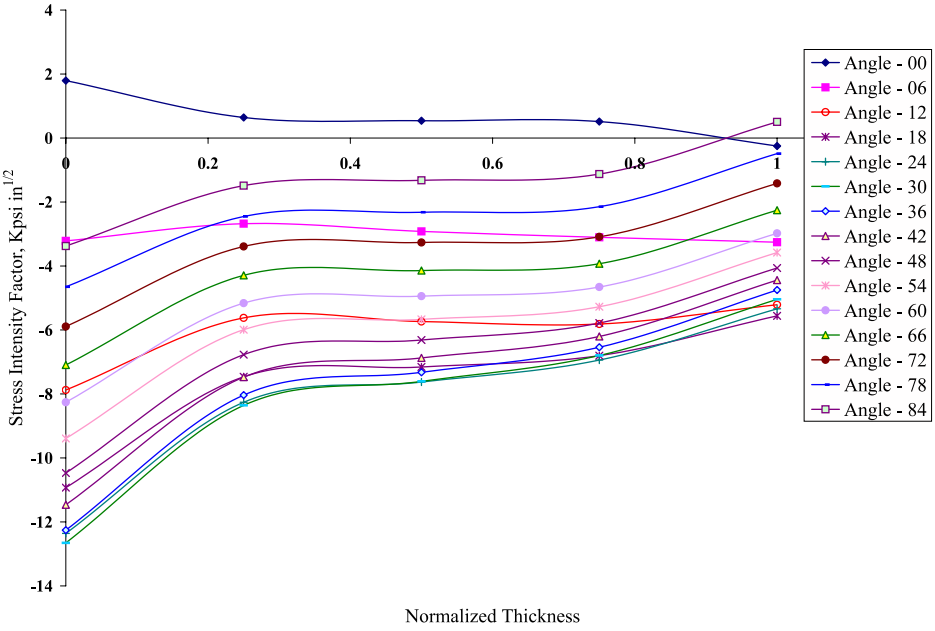

Figure 5–23: Variation of SIF K_{II} along BD specimen thickness at different Crack angle for $[10\bar{1}]$ orientation.

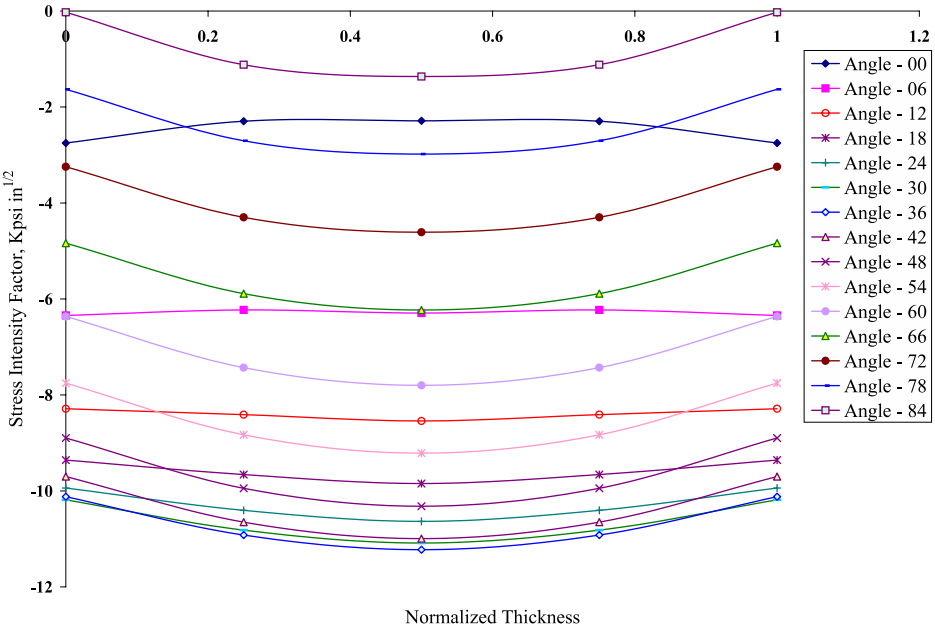

Figure 5–24: Variation of SIF K_{II} along BD specimen thickness at different Crack angle for $[\bar{1}2\bar{1}]$ orientation.

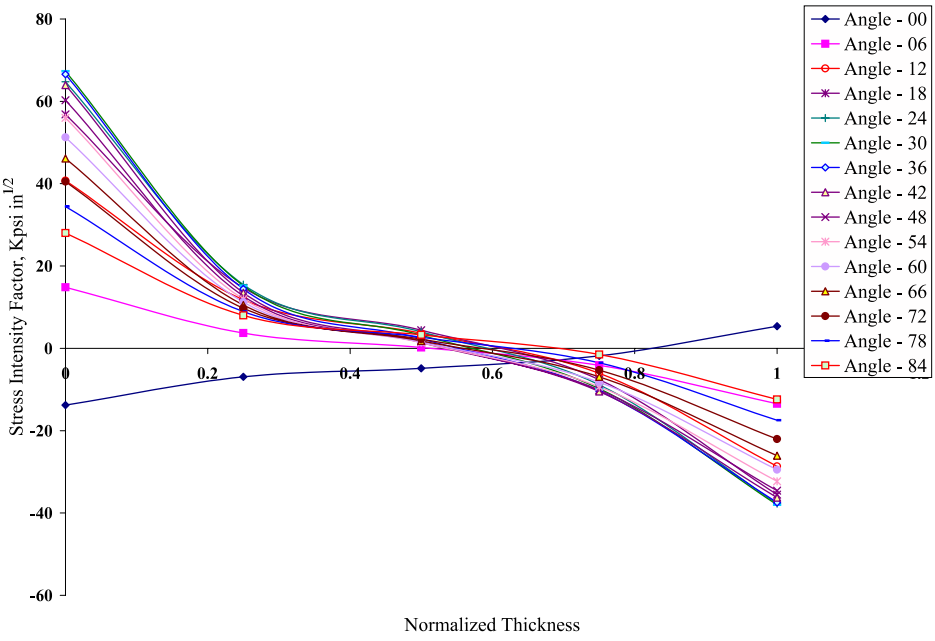

Figure 5–25: Variation of SIF K_{III} along BD specimen thickness at different Crack angle for $[10\bar{1}]$ orientation.

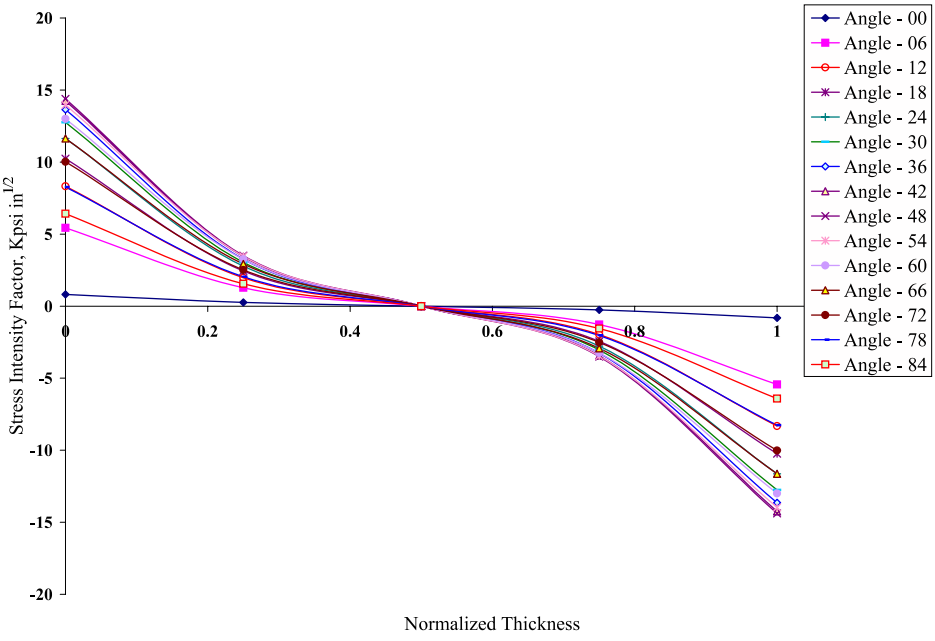

Figure 5–26: Variation of SIF K_{III} along BD specimen thickness at different Crack angle for $[\bar{1}2\bar{1}]$ orientation.

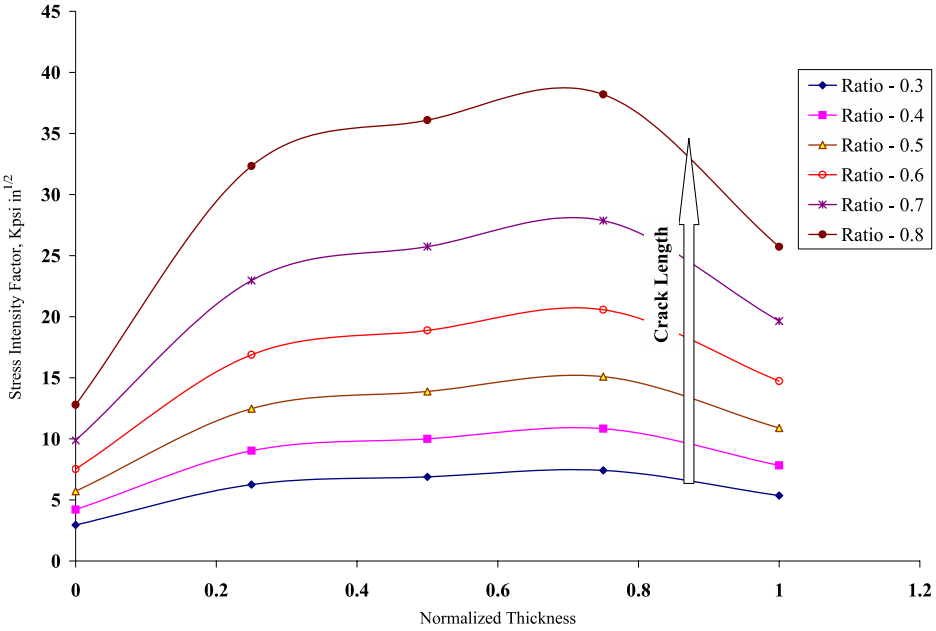

Figure 5–27: Variation of SIF K_I along BD specimen thickness at different Crack Length/Diameter ratio for $[10\bar{1}]$ orientation.

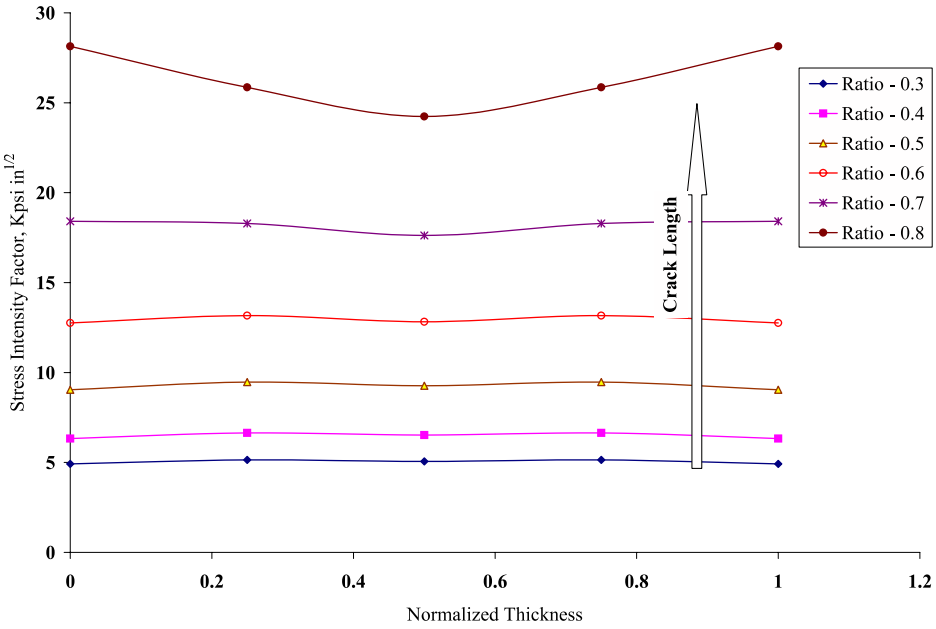

Figure 5–28: Variation of SIF K_I along BD specimen thickness at different Crack Length/Diameter ratio for $[\bar{1}2\bar{1}]$ orientation.

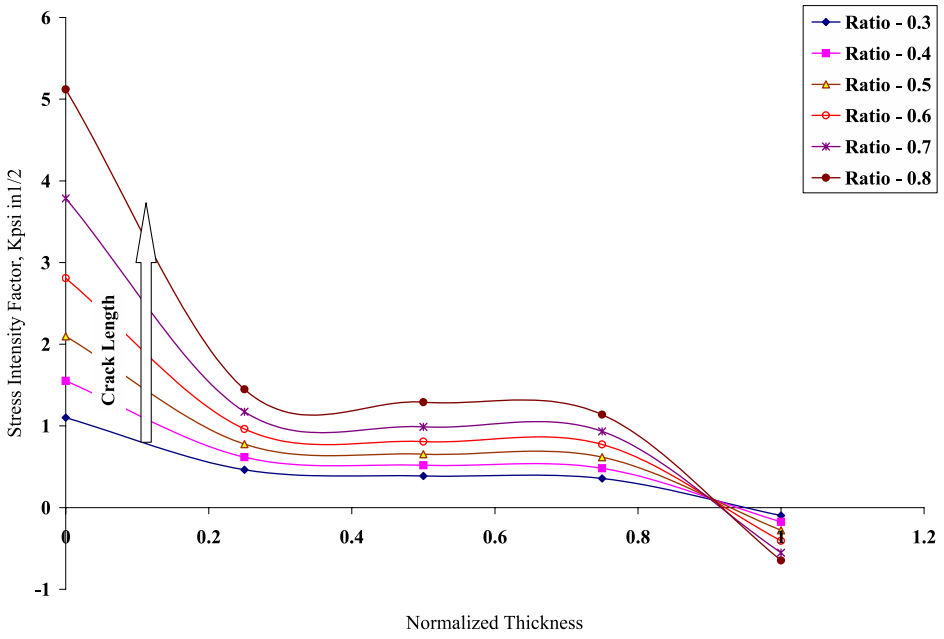

Figure 5–29: Variation of SIF K_{II} along BD specimen thickness at different Crack Length/Diameter ratio for $[10\bar{1}]$ orientation.

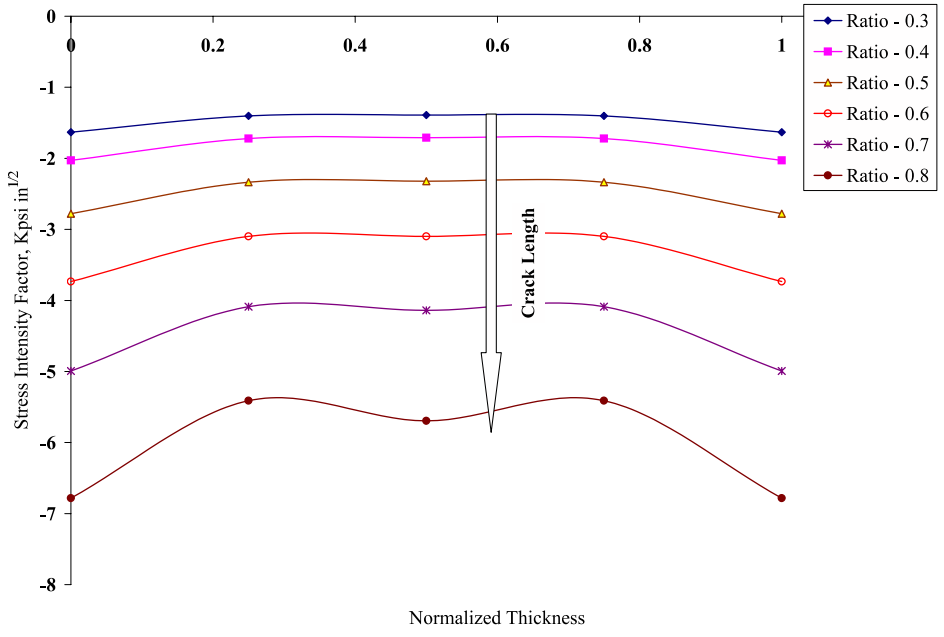

Figure 5–30: Variation of SIF K_{II} along BD specimen thickness at different Crack Length/Diameter ratio for $[\bar{1}2\bar{1}]$ orientation.

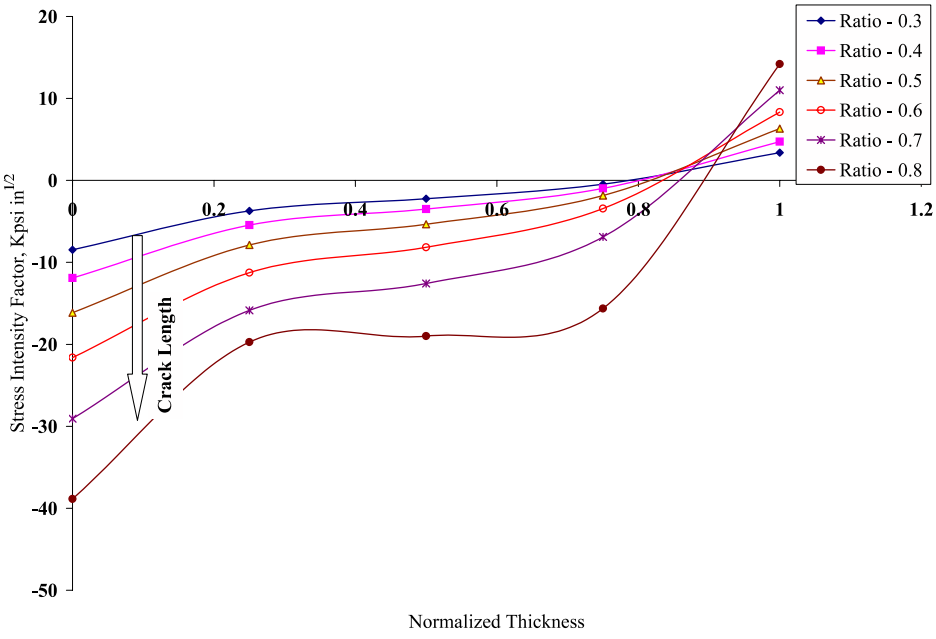

Figure 5–31: Variation of SIF K_{III} along BD specimen thickness at different Crack Length/Diameter ratio for $[10\bar{1}]$ orientation.

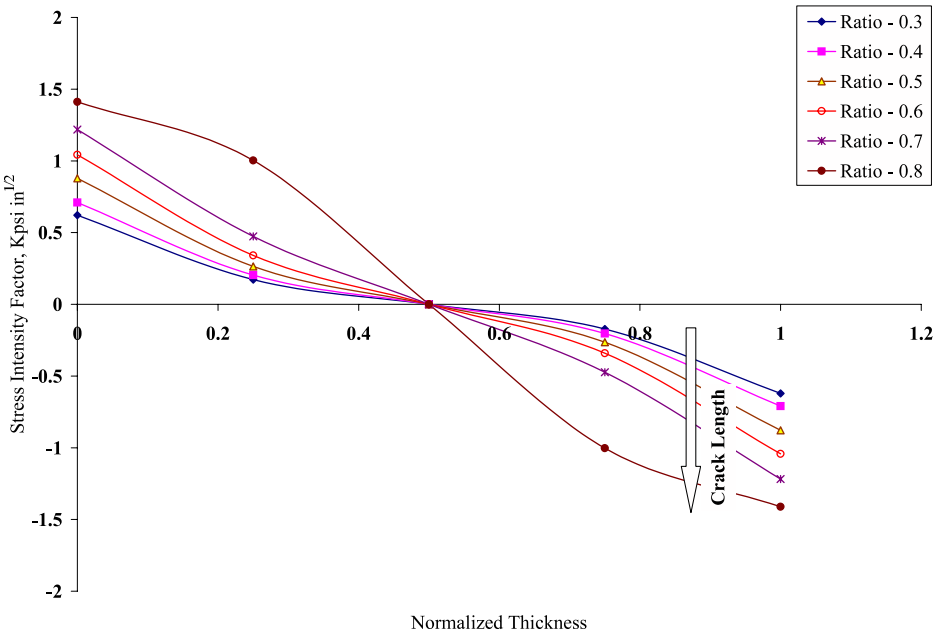

Figure 5–32: Variation of SIF K_{III} along BD specimen thickness at different Crack Length/Diameter ratio for $[\bar{1}2\bar{1}]$ orientation.

CHAPTER 6
FCG GROWTH IN FCC SINGLE CRYSTAL MATERIALS

6.1 Isotropic materials

The fracture mechanics approach considers only the part of the component life after the nucleation of a defect or flaw. In the 1960's, Paris demonstrated the usefulness of linear elastic fracture mechanics (LEFM) in characterizing fatigue crack growth. Paris determined that a relationship existed between the crack extension per load cycle and the range of the applied stress intensity factor, ΔK. The form of this relationship is a power law form and is today widely known as the Paris Law.

$$\frac{da}{dN} = C.\Delta K^m \tag{6.1}$$

where C and m are constants determined from fitting experimental data. Here m is the slope of the region II fatigue crack growth rate (FCGR) curve (Fig. 6–1 on page 59, region II) and C is the coefficient found by extending the straight line to $\Delta K = 1MPa\sqrt{m}$ $\left(\text{or } 1ksi\sqrt{in}\right)$. This law applies only to the linear region (region II) of the fatigue crack growth curve .

In theory, application of this law to a fatigue crack growth problem can be performed, given enough information, to approximately predict the number of cycles until a critical crack size is reached. The Paris Law served as a basis for the construction of more complicated laws which have attempted to account for threshold, crack closure, stress ratio and other effects. A typical (schematic) fatigue crack growth curve is shown in Fig. 6–1 on page 59. This curve indicates the three regions of fatigue crack growth. In region I little or no crack growth occurs due to the low value of stress intensity factor range. Region II indicates a

power law relationship of the Paris Law type. In this region fatigue crack growth corresponds to the stable macroscopic crack growth that is typically controlled by the environment (load, geometry, temp. etc). Region *III* is a region of rapid crack propagation and imminent fracture. This region is controlled primarily by fracture toughness K_c or K_{Ic}, which in turn depends on the microstructure, mean stress, and environment.

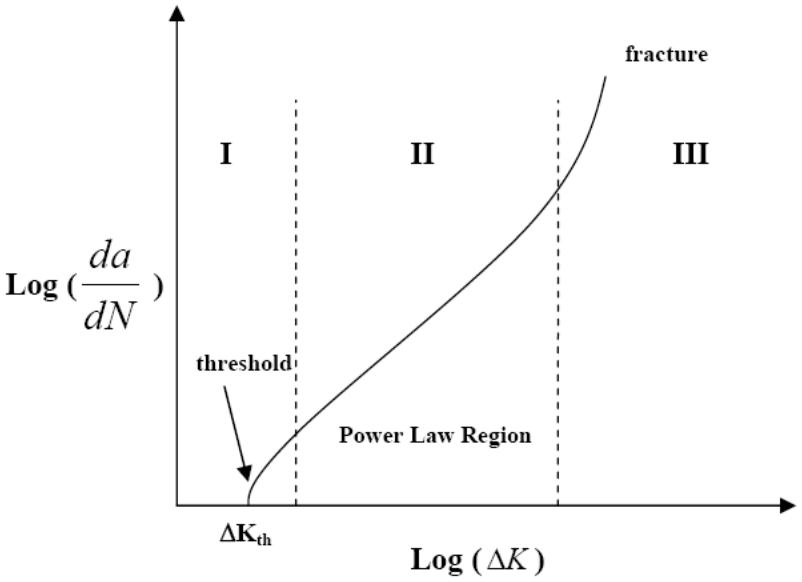

Figure 6–1: Schematic Fatigue Crack Growth Curve

Typically Mode *I* (crack opening mode) FCG is the predominant mode of macroscopic fatigue crack growth while Mode *II* (shearing mode) and Mode *III* (tearing mode) usually have only second order effects on both crack direction and crack growth rates. Under mixed mode loading condition, a crack can change its direction of growth as different combinations of mixed-mode loading can exist from multiaxial loads. In order to obtain the crack growth rate, da/dN, or cycles to failure using Paris equation (6.1), under mixed-mode loading, several forms of equivalent stress intensity factors have been proposed. An equivalent stress intensity factor range, $\Delta K_{q,}$ based on crack tip displacements was proposed by

Tanaka as:

$$\Delta K_q = \left(\Delta K_I^4 + 8\Delta K_{II}^4 + \frac{8\Delta K_{III}^4}{1-\nu} \right)^{0.25} \tag{6.2}$$

Another form of equivalent stress intensity factor based on the equivalence of energy release rate, G, and the stress intensity factor, K, for nominal elastic loading is given as:

$$\Delta K_q = \left[\Delta K_I^2 + \Delta K_{II}^2 + (1+\nu)\, \Delta K_{III}^2 \right]^{0.5} \tag{6.3}$$

Fatigue life for through the thickness cracks is found by integrating Paris in region II as:

$$\int_{a_i}^{a_c} da = \int_0^{N_f} (C.\Delta K^m)\, .dN \tag{6.4}$$

Where ΔK for an isotropic material, under the application of uniform tensile stress range, $\Delta\sigma$, can be computed using the relation,

$$\Delta K = C\Delta\sigma\sqrt{\pi a} \tag{6.5}$$

Where C is geometrical constant.

The equations (6.4) and (6.5) can be used to calculate the fatigue life from an assumed initial crack size α_0 to a critical crack size a_f:

$$N_f = \frac{2}{(m-2)\, C_m C^m\, (\Delta\sigma)^m\, \pi^{m/2}} \left\{ \frac{1}{(a_0)^{(m-2)/2}} - \frac{1}{(a_f)^{(m-2)/2}} \right\}, \qquad for \;\; m \neq 2 \tag{6.6}$$

Fig. 6–2 on page 61 shows schematically three crack length versus applied cycle curves for three identical test specimens subjected to different repeated stress levels with $S_1 > S_2 > S_3$. All test specimens contained the same initial crack length, a_0, and in each test the minimum stress was zero ($R = 0$). It can be observed that with higher stresses the crack growth rates, da/dN, are higher at a given crack length, and the fatigue crack growth life (N_f) is shorter. The crack lengths at fracture are shorter at higher stress levels. This concludes that for a

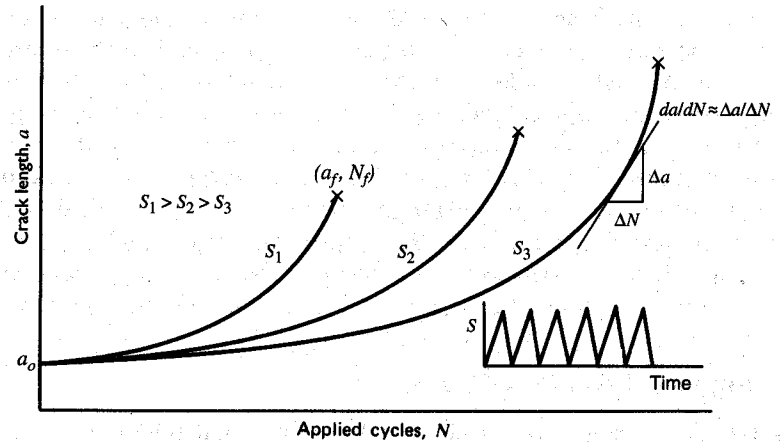

Figure 6–2: Fatigue Crack Length versus Applied Cycles. Fracture is Indicated by the x.[43]

given initial crack size, the life to fracture depends on the magnitude of the applied stress and the fracture resistance of the material.

6.2 FCC single crystal materials

Fatigue crack driving force parameter ΔK, as described in previous section is well suited for isotropic materials, but it may not be the best parameter to use for very large grain or single crystal alloys. Earlier studies have shown that for crack size smaller than the grain size or of the same order of magnitude, threshold stress intensities are lower and FCG rate is accelerated in comparison to long cracks when compared at similar values of ΔK [44–48]. This shows that the parameter ΔK does not incorporate microstructure and the grain orientation and the associated deformation mechanisms in controlling the FCG behavior.

An FCC single crystal alloy offers the best opportunity to study in detail the effect of microstructure and the deformation mechanisms on the FCG behavior. Several Studies have been conducted on FCG of Ni-base single crystals [49–53] and all of these studies have shown that FCG is highly sensitive to the orientation of the crystal and that the crack plane is crystallographic and follows a single slip plane or a combination of slip planes. Since shear decohesion on a slip plane is

caused by dislocation motion, many researchers have suggested that the resolved shear stress acting on the active slip plane ahead of a crack tip must be responsible for the propagation of the fatigue crack [51, 54, 55]. The dislocation motion is controlled by the forces at the crack tip, which is directly related to the resolved shear stress on the slip plane. Therefore the rate of shear decohesion must be related to the resolved shear stress 'intensity' (RSSI) at the crack tip. The active shear decohesion plane or planes must be the slip plane(s) with a high RSSI. If the RSSI on a plane is much higher than all the other slip planes, then the plane must be the primary plane for shear decohesion and the slip plane becomes the crack plane. But if the resolved shear stresses on two or more of the slip systems are comparable, then the shear decohesion will take place on all of those slip planes and the macro crack plane will not follow a single slip plane. This was shown by Telesman and Ghosn [56] as shown in the Fig. 6–3 on page 62. Even though macroscopic crack was observed along (001) plane inclined 7^0 to the starter notch, the microscopic slip was observed on 111 slip planes, inclined 52^0 and -38^0 to the starter notch.

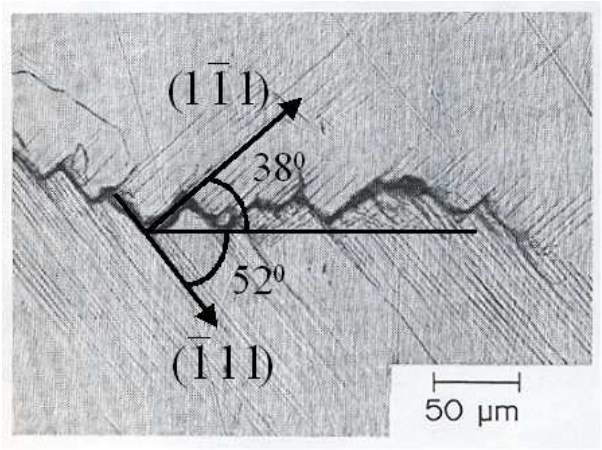

Figure 6–3: Microscopic slip observed on two {111} slip planes inclined 52^0 and -38^0 to the starter notch.[56]

If a crack surface is a slip plane, it is logical that the crack growth rate on that slip plane will correlate with its RSSI.

Chen and Liu [57] proposed a crack driving force parameter for correlating FCG data, which is based on the resolved shear stresses on the active slip plane(s). This parameter may be better than ΔK for the correlation of FCG data since it takes into consideration of the deformation mechanisms, grain orientation and the actual crack path.

The resolved shear stress field of a slip system is defined by its intensity coefficient, which can be calculated once the Mode *I*, *II* and *III* crack tip fields are obtained.

The resolved shear stress is given by [58]

$$\tau_{rss} = \frac{1}{b} b_i \sigma_{ij} n_j \tag{6.7}$$

where b_i and b are the Burgers vector and its magnitude; n_j is the unit normal vector of the slip plane; and σ_{ij} is the crack tip stress tensor field given by [57]

$$[\sigma_{ij}] = \frac{1}{\sqrt{2\pi r}} [K_I f_{ij}^I(\theta) + K_{II} f_{ij}^{II}(\theta) + K_{III} f_{ij}^{III}(\theta)] \tag{6.8}$$

where r and θ are the local polar coordinates at the crack tip as shown in the Fig. (6–4 on page 64); $f_{ij}(\theta)$ are the angular component of the stress field. Substituting equation (6.8) into equation (6.7), the resolved shear stress is

$$\tau_{rss} = \frac{1}{\sqrt{2\pi r}} [b_i^n][K_I f_{ij}^I(\theta) + K_{II} f_{ij}^{II}(\theta) + K_{III} f_{ij}^{III}(\theta)][n_j] \tag{6.9}$$

where b_i^n and n_j are the unit Burgers vectors and unit normal vectors of the slip planes respectively.

The above equation indicates that τ_{rss} preserves the $1/\sqrt{r}$ singularity, and the intensity of τ_{rss} is dependent on the crystal orientation relative to the crack surface. For a given crystal orientation and crack geometry, the angle θ is equal to the angle

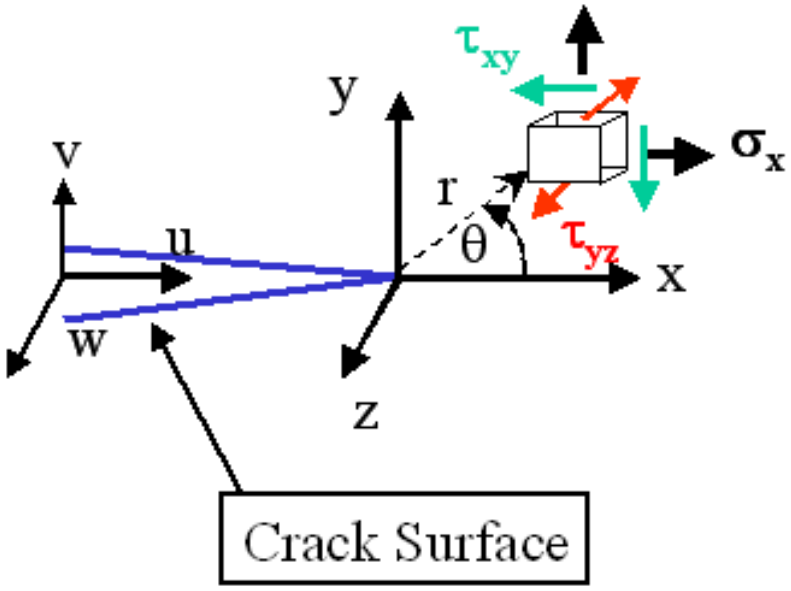

Figure 6–4: Details of crack tip displacements and stresses at a distance r and θ from the crack tip in the crack coordinate system

between the trace of a particular slip plane on the plane normal to the slip plane and the horizontal axis. The intensity of τ_{rss} is linearly proportional to the quantity resolved shear stress intensity coefficient, K_{rss}, which for a given slip system can be defined as the limiting value of the resolved shear stress, τ_{rss}, multiplied by $\sqrt{2\pi r}$, as r approaches zero [56, 57]

$$K_{rss} = \lim_{r \to 0} \tau_{rss} . \sqrt{2\pi r} \tag{6.10}$$

where r is the distance of the crack tip and τ_{rss} is defined as the projection of the stress tensor $[\sigma]$ on a plane whose outward normal is $\overrightarrow{n}$ in the direction of slip $\overrightarrow{b}$ (Fig. 6–5 on page 65). The two distinct advantages in using K_{rss} are: (1) the dependency of τ_{rss} on r is eliminated; (2) the angle θ has a definite physical meaning, which is directly related to the orientation of the slip system.

Telesman and Ghosn [56] used the above model to calculate ΔK_{rss} for 2-D model and checked the validity of this parameter by plotting it against da/dN data (Fig. 6–6 on page 65). Also ΔK for mode I has been plotted against da/dN to

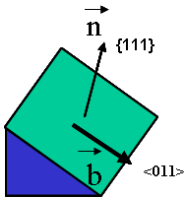

Figure 6–5: Burgers vector $\overrightarrow{b}$ is along slip direction $\langle 011 \rangle$ and slip plane direction is normal vector $\overrightarrow{n}$ along $\langle 111 \rangle$

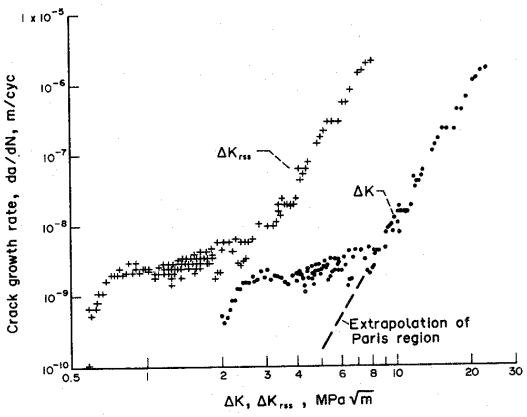

Figure 6–6: Fatigue crack growth rate as a function of ΔK_{rss} and ΔK for 2-D rectangular specimen.[56]

show similarity between both the curves. They look virtually identical and it can be seen that a linear relationship exists between ΔK_{rss} and da/dN, which is in accordance with the Paris law in region *II*. But in this method mode *III* SIF was not considered as the specimen was not tested under complete multiaxial fatigue loading.

State of stress on a slip plane, under mixed mode loading, whose trace on a plane normal to crack plane makes an angle θ with the horizontal axis (Fig. 6–4 on page 64 and Fig. 6–13 on page 71), can be defined as[1]

$$\begin{Bmatrix} \sigma_x \\ \sigma_y \\ \sigma_z \\ \tau_{yz} \\ \tau_{zx} \\ \tau_{xy} \end{Bmatrix} = \frac{1}{\sqrt{2\pi r}} \begin{bmatrix} d_{11} & d_{12} & 0 \\ d_{21} & d_{22} & 0 \\ d_{31} & d_{32} & d_{33} \\ 0 & 0 & d_{43} \\ 0 & 0 & d_{53} \\ d_{61} & d_{62} & 0 \end{bmatrix} \cdot \begin{Bmatrix} K_I \\ K_{II} \\ K_{III} \end{Bmatrix} \tag{6.11}$$

where,

$$d_{11} = \mathrm{Re}\left[\frac{\mu_1\mu_2}{\mu_1 - \mu_2}\left(\frac{\mu_2}{b_2} - \frac{\mu_1}{b_1}\right)\right] \qquad d_{12} = \mathrm{Re}\left[\frac{1}{\mu_1 - \mu_2}\left(\frac{\mu_2^2}{b_2} - \frac{\mu_1^2}{b_1}\right)\right]$$

$$d_{21} = \mathrm{Re}\left[\frac{1}{\mu_1 - \mu_2}\left(\frac{\mu_1}{b_2} - \frac{\mu_2}{b_1}\right)\right] \qquad d_{22} = \mathrm{Re}\left[\frac{1}{\mu_1 - \mu_2}\left(\frac{1}{b_2} - \frac{1}{b_1}\right)\right]$$

$$d_{3j} = \begin{cases} 0 & \text{Plane Stress} \\ -\dfrac{d_{1j}a_{13} + d_{2j}a_{23} + d_{6j}a_{36}}{a_{33}} & \text{Plane Strain} \end{cases} \qquad j = 1, 2$$

[1] The details of the equation derivation can be seen in Appendix B.

$$d_{33} = \begin{cases} 0 & \text{Plane Stress} \\ -\dfrac{d_{43}a_{34} + d_{53}a_{35}}{a_{33}} & \text{Plane Strain} \end{cases}$$

$$d_{43} = \text{Re}\left[\frac{1}{b_3}\right] \qquad d_{53} = -\,\text{Re}\left[\frac{\mu_3}{b_3}\right]$$

$$d_{61} = \text{Re}\left[\frac{\mu_1\mu_2}{\mu_1 - \mu_2}\left(\frac{1}{b_1} - \frac{1}{b_2}\right)\right] \qquad d_{62} = \text{Re}\left[\frac{1}{\mu_1 - \mu_2}\left(\frac{\mu_1}{b1} - \frac{\mu_2}{b2}\right)\right]$$

$$b_i = \sqrt{\cos(\theta) + \mu_i \sin(\theta)} \qquad i = 1, 2, 3$$

μ_1 and μ_2 are the two roots with positive imaginary parts as defined by the equation

$$a_{11}\mu^4 - 2a_{16}\mu^3 + (2a_{12} + a_{66})\mu^2 - 2a_{26}\mu + a_{22} = 0 \tag{6.12}$$

and μ_3 is the root of the characteristic equation [26]

$$a_{55}\mu^2 - 2a_{45}\mu + a_{44} = 0 \tag{6.13}$$

It should be noted that the compliance constants $(a_{i,3}(i = 1, 2, \ldots 6))$ used for the expression $(d_{3,j}(j = 1, 2, 3))$ are the ones as given by equation (3.9).

The above equations, when used in conjunction with equations (6.7) & (6.10) gives K_{rss} on all the 12 slip systems for FCC single crystal superalloy.

$$K_{rss} = [b_i^n][n_j] \begin{bmatrix} d_{11} & d_{12} & 0 \\ d_{21} & d_{22} & 0 \\ d_{31} & d_{32} & d_{33} \\ 0 & 0 & d_{43} \\ 0 & 0 & d_{53} \\ d_{61} & d_{62} & 0 \end{bmatrix} \cdot \begin{Bmatrix} K_I \\ K_{II} \\ K_{III} \end{Bmatrix} \tag{6.14}$$

Three BD specimen of PWA1422 were tested (Table 6–1 on page 68) to correlate the fatigue crack growth data with the calculated ΔK_{rss}. The crack growth of these three specimens with the application of cyclic load has been shown in the Figs. (6–7, 6–8, 6–9 on page 69). As it can be seen that there are numerous points along the path. For the specimen 95830 (Fig. 6–7 on page 69), it can be seen that the crack growth stopped after reaching $\sim 8.8mm$, which was due to crack closure. Whereas a decline in crack growth can be seen for specimen 96842 (Fig. 6–11 on page 69) after crack length reaches $\sim 6.5mm$. Specimen 98C21 has a slow crack growth in the beginning, but later an accelerated growth is observed till crack length reaches $\sim 8.4mm$. The curve fitting was necessary in order to calculate da/dN accurately at any given point. No single curve fit could properly fit for entire path. Therefore a combination of several equations for curve fit was required to get the desired result. The corresponding da/dN obtained from those equations for the three specimens have been shown in Figs. (6–10,6–11,6–12 on page 69). The crack growth rate declines after crack grows to $\sim 6.5mm$ for specimens 95830 and 96842, which is unusual.

Table 6–1: The geometry and loading condition of the three Brazilian Disk specimen tested

Specimen	**Orientation**	**Test Temperature (°C)**	**Test Frequency (Hz)**	**Load Ratio R**
95830	(111) ⟨110⟩	23	40	0.1
96842	(111) ⟨110⟩	23	10	0.1
98C21	(111) ⟨110⟩	23	10	0.1

Specimen	**Diameter W (mm)**	**Thickness t (mm)**	**Initial Crack Length a(mm)**	**Crack angle with load θ**
95830	28.00	2.12	4.16	27.27^0
96842	27.97	2.23	4.16	16^0
98C21	28.03	2.20	2.27	16^0

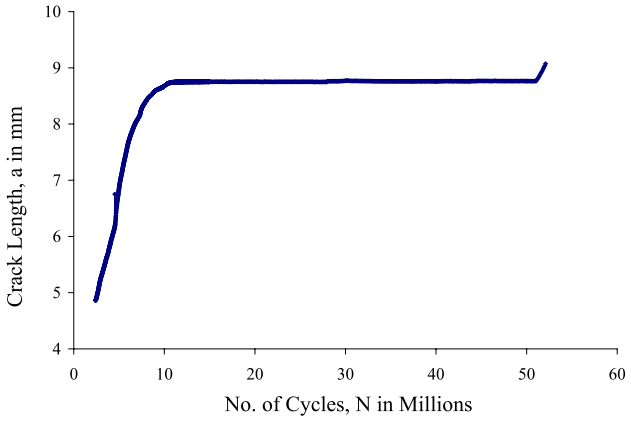

Figure 6–7: Crack growth of BD specimen 95830 with no. of cycles

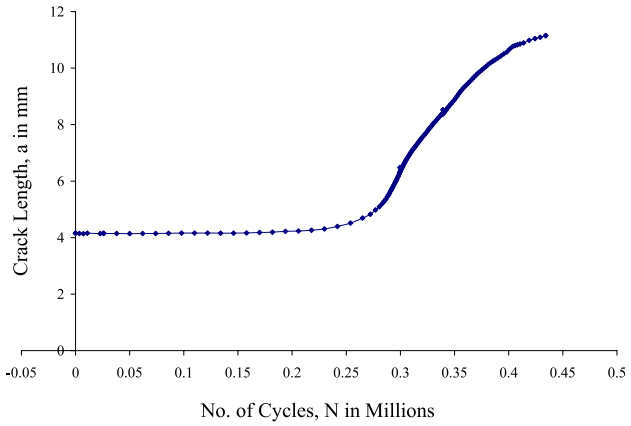

Figure 6–8: Crack growth of BD specimen 96842 with no. of cycles

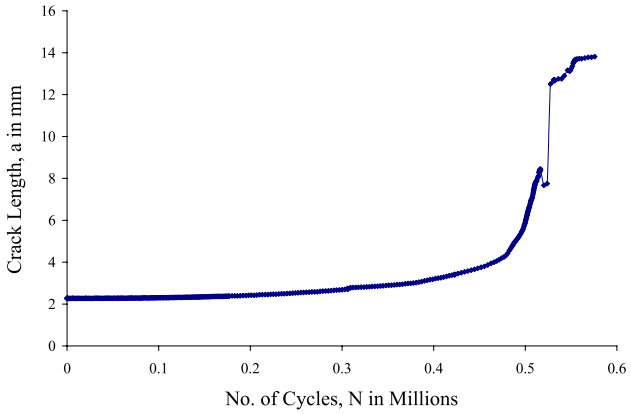

Figure 6–9: Crack growth of BD specimen 98C21 with no. of cycles

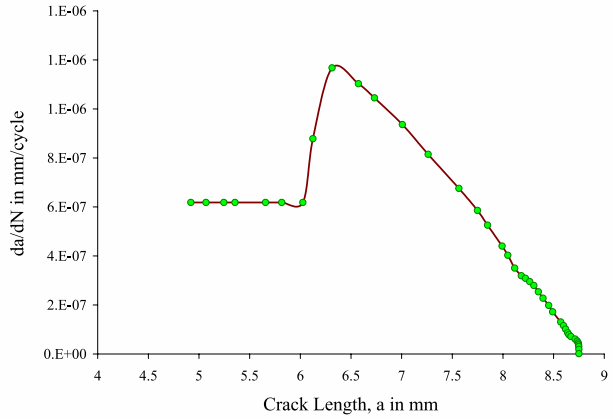

Figure 6–10: Crack growth rate of BD specimen 95830 with increasing crack length

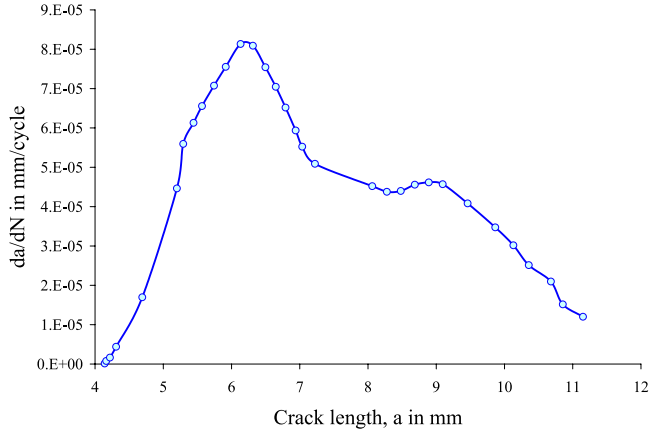

Figure 6–11: Crack growth rate of BD specimen 96842 with increasing crack length

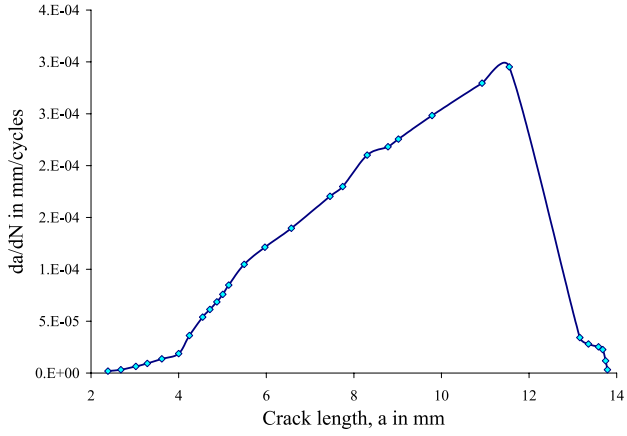

Figure 6–12: Crack growth rate of BD specimen 98C21 with increasing crack length

The mixed mode SIFs were calculated at those points shown in the Figs. (6–10, 6–11, 6–12 on page 69) for all the three specimens on the mid plane of the Brazilian disk specimens, assuming plane strain assumption. ΔK_{rms} was calculated using the following equation in order to compare with ΔK_{rss}.

$$\Delta K_{rms} = \sqrt{\Delta K_I^2 + \Delta K_{II}^2 + \Delta K_{III}^2} \tag{6.15}$$

K_{rss} was calculated using the equation (6.10), where state of stress obtained from equation (6.11) was multiplied by Schmid's factor for FCC single crystal as defined in equation (1.13) to get the resolved shear stress intensity on all the 12 primary slip systems. The trace of the two slip planes $(\bar{1}1\bar{1})$ and $(1\bar{1}\bar{1})$ were found to be making equal angles with the (111) plane (67.78^0), while the trace of the plane $(\bar{1}\bar{1}1)$ was making 0^0 with the crack plane (111) as shown in the Fig. 6–13.

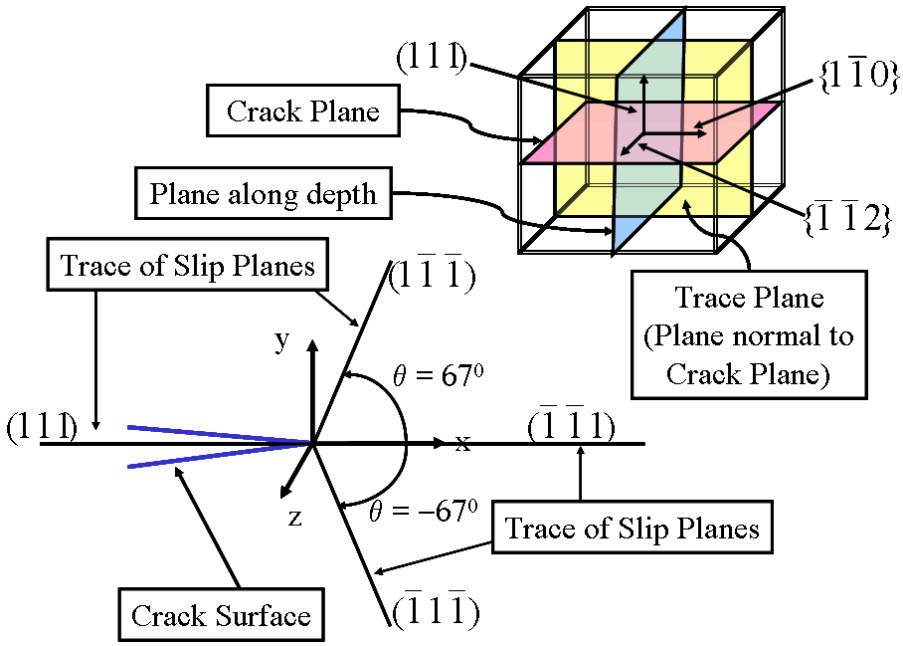

Figure 6–13: Trace of primary slip planes on the plane normal to the crack plane

The load ratio R (min load/max load) was 0.1 (Table 6–1 on page 68), as the load on the BD specimen always compressive. As SIFs are linearly proportional to the load applied, therefore K_{rss} was multiplied with R to get the ΔK_{rss}.

The max K_{rss} was found to be on the (111) slip plane for all the three specimens (First row of Tables 6–2, 6–3 on page 76 and Table 6–4 on page 77), as observed in the experiment test results (Fig. 6–14 on page 73). The calculated ΔK_{rss} was plotted against da/dN on a log-log scale to check the validity of the model (Fig. 6–16 on page 74). After ΔK_{rss} reaches 10 MPa$\sqrt{m}$ a linear plot can be seen, which might correspond to region *II* (Paris region) where the crack growth rate is directly proportional to the the applied ΔK, on a log-log basis. But not enough data is available to support the theory.[2] However below a ΔK_{rss} of 8 MPa$\sqrt{m}$ an accelerated crack growth can be seen between 5 MPa$\sqrt{m}$ and 7 MPa$\sqrt{m}$, in the threshold region; region or stage *I*. The lines drawn through those points yield ΔK_{th} on the ΔK_{rss} axis, which is called fatigue threshold stress intensity factor. The average ΔK_{th} of the three specimens has been taken ($\sim 4.3MPa\sqrt{m}$), at the given load ratio R(=0.1). Below this value ($\Delta K_{rss} < \Delta K_{th}$ crack growth either does not occur by cyclic loading i. e. $da/dN = 0$ and specimen can have infinite life or it grows at undetectable rates. The value of ΔK_{th} can be affected by alterations in the material microstructure, load ratio, environment and crack size [3] . However the cyclic stress intensity factor (ΔK_{rss}) is not the only load parameter to control the FCG rate, because da/dN, at a given ΔK_{rss}, can increase with increase in load ratio 'R' as

$$K_{max} = \frac{\Delta K_{rss}}{(1 - R)}$$

[2] Because of the proprietary nature of specimens, only three specimens' data were made available. But we are expecting some more data in June'05 to verify our work.

[3] The effect of these parameters on cyclic stress intensity factor is beyond the scope of my research. However the detail can be found in 'Fatigue of Materials' by S. Suresh [59]

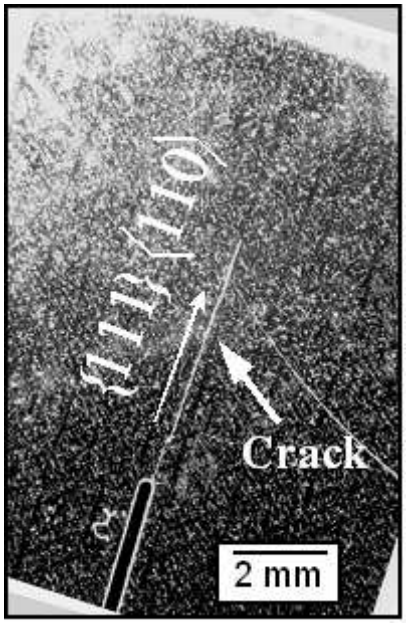

Figure 6–14: Crack growth on {111} slip plane can be observed for 96842 BD specimen

A similar nature of ΔK_{rms} can be seen in Fig. 6–15 on page 74. The advantage of ΔK_{rss} lies in the ability to predict the actual microscopic fatigue fracture mechanisms and also it takes into consideration the orientation of the grain. The ΔK_{rss} also is a multiaxial fatigue stress parameter, incorporating resolved shear stress on primary slip systems.

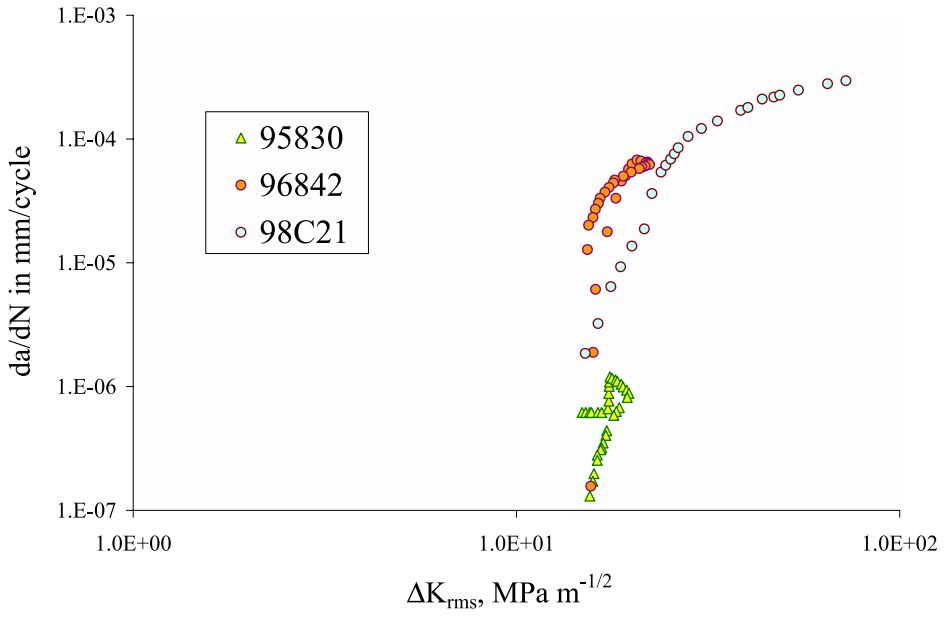

Figure 6–15: Fatigue crack growth rate of 3 specimens 95830, 96842, 98C21, as a function of ΔK_{rms}

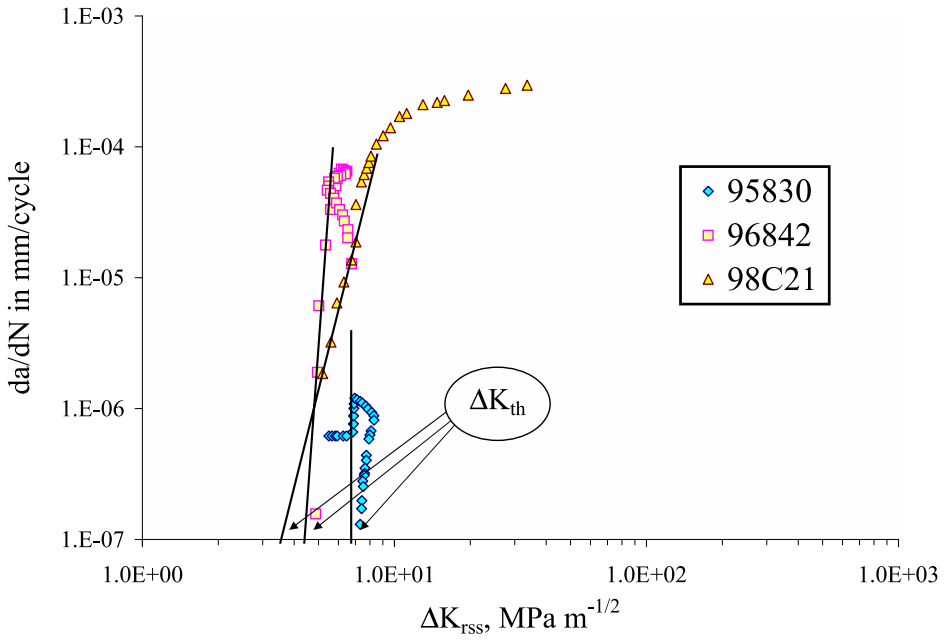

Figure 6–16: Fatigue crack growth rate of 3 specimens 95830, 96842, 98C21, as a function of ΔK_{rss}

Table 6–2: K_{rss} for 12 primary slip systems with increasing crack length for specimen 95830

Slip Plane	Slip Direction	K_{rss} in MPa $\sqrt{m}$ for Specimen 95830 with increasing Crack length a in mm						
		5.25	**5.36**	**5.66**	**5.82**	**6.09**	**6.10**	**6.12**
(111)*	$[10\bar{1}]$	-6.45	-6.59	-6.95	-7.18	-7.58	-7.61	-7.64
(111)	$[0\bar{1}1]$	1.91	1.97	2.13	2.22	2.40	2.42	2.43
(111)	$[1\bar{1}0]$	-4.54	-4.63	-4.83	-4.96	-5.18	-5.19	-5.21
$(\bar{1}1\bar{1})$	$[10\bar{1}]$	-1.17	-1.18	-1.21	-1.23	-1.27	-1.27	-1.27
$(\bar{1}1\bar{1})$	[110]	1.00	0.99	0.95	0.92	0.85	0.85	0.85
$(\bar{1}1\bar{1})$	[011]	2.17	2.17	2.16	2.16	2.12	2.12	2.12
$(1\bar{1}\bar{1})$	[110]	0.83	0.87	0.98	1.05	1.18	1.18	1.19
$(1\bar{1}\bar{1})$	$[0\bar{1}1]$	3.07	3.09	3.10	3.12	3.11	3.11	3.11
$(1\bar{1}\bar{1})$	[101]	3.90	3.96	4.08	4.16	4.28	4.29	4.30
$(\bar{1}\bar{1}1)$	[011]	1.91	1.97	2.13	2.22	2.40	2.42	2.43
$(\bar{1}\bar{1}1)$	[101]	-2.99	-3.02	-3.08	-3.11	-3.15	-3.15	-3.16
$(\bar{1}\bar{1}1)$	$[1\bar{1}0]$	-4.91	-4.99	-5.20	-5.33	-5.55	-5.57	-5.59

* Slip plane (111) is the plane where K_{rss} is maximum through out and it was also experimentally observed to be the crack growth plane.

Table 6–3: K_{rss} for 12 primary slip systems with increasing crack length for specimen 96842

Slip Plane	Slip Direction	K_{rss} in MPa $\sqrt{m}$ for Specimen 96842 with increasing Crack length a in mm						
		8.06	**8.38**	**8.67**	**9.09**	**9.46**	**9.87**	**10.13**
(111)*	$[10\bar{1}]$	-6.11	-5.95	-6.20	-6.39	-6.56	-6.75	-6.91
(111)	$[0\bar{1}1]$	1.03	1.12	1.29	1.51	1.71	1.93	2.10
(111)	$[1\bar{1}0]$	-5.08	-4.83	-4.91	-4.88	-4.85	-4.81	-4.81
$(\bar{1}1\bar{1})$	$[10\bar{1}]$	-1.61	-1.48	-1.46	-1.39	-1.33	-1.25	-1.21
$(\bar{1}1\bar{1})$	[110]	2.59	2.29	2.14	1.84	1.56	1.23	1.02
$(\bar{1}1\bar{1})$	[011]	4.20	3.77	3.60	3.23	2.89	2.49	2.22
$(1\bar{1}\bar{1})$	[110]	-0.17	-0.02	0.13	0.36	0.56	0.79	0.96
$(1\bar{1}\bar{1})$	$[0\bar{1}1]$	5.42	4.90	4.73	4.31	3.92	3.47	3.17
$(1\bar{1}\bar{1})$	[101]	5.25	4.89	4.86	4.67	4.48	4.26	4.13
$(\bar{1}\bar{1}1)$	[011]	1.03	1.12	1.29	1.51	1.71	1.93	2.10
$(\bar{1}\bar{1}1)$	[101]	-4.66	-4.25	-4.15	-3.86	-3.60	-3.29	-3.10
$(\bar{1}\bar{1}1)$	$[1\bar{1}0]$	-5.68	-5.37	-5.44	-5.37	-5.30	-5.22	-5.19

* Slip plane (111) is the plane where K_{rss} is maximum through out and it was also experimentally observed to be the crack growth plane.

Table 6–4: K_{rss} for 12 primary slip systems with increasing crack length for specimen 98C21

Slip Plane	Slip Direction	K_{rss} in MPa $\sqrt{m}$ for Specimen 98C21 with increasing Crack length a in mm						
		7.74	**8.31**	**8.78**	**9.02**	**9.79**	**10.93**	**11.55**
(111)*	$[10\bar{1}]$	-12.42	-14.40	-16.41	-17.54	-21.82	-30.65	-37.37
(111)	$[0\bar{1}1]$	1.82	2.62	3.50	4.02	6.10	10.75	14.46
(111)	$[1\bar{1}0]$	-10.60	-11.78	-12.91	-13.52	-15.72	-19.91	-22.91
$(\bar{1}1\bar{1})$	$[10\bar{1}]$	-3.45	-3.65	-3.82	-3.90	-4.14	-4.41	-4.48
$(\bar{1}1\bar{1})$	[110]	5.80	5.74	5.50	5.32	4.34	1.53	-0.86
$(\bar{1}1\bar{1})$	[011]	9.24	9.39	9.32	9.22	8.48	5.94	3.62
$(1\bar{1}\bar{1})$	[110]	-0.68	-0.16	0.46	0.83	2.38	6.02	9.01
$(1\bar{1}\bar{1})$	$[0\bar{1}1]$	11.85	12.18	12.27	12.24	11.73	9.48	7.33
$(1\bar{1}\bar{1})$	[101]	11.17	12.02	12.72	13.07	14.11	15.50	16.33
$(\bar{1}\bar{1}1)$	[011]	1.82	2.62	3.50	4.02	6.10	10.75	14.46
$(\bar{1}\bar{1}1)$	[101]	-10.09	-10.52	-10.78	-10.88	-10.99	-10.37	-9.50
$(\bar{1}\bar{1}1)$	$[1\bar{1}0]$	-11.91	-13.14	-14.29	-14.90	-17.09	-21.12	-23.96

* Slip plane (111) is the plane where K_{rss} is maximum through out and it was also experimentally observed to be the crack growth plane.

CHAPTER 7
CONCLUSIONS

The goal was to estimate the fatigue life of single crystal nickel-base superalloys, based on fatigue crack driving force parameter, for which a numerical model was developed to compute mixed mode SIFs at the crack tip. The results obtained can be summarized as

1. An analytical method has been developed for the calculation of all the three modes of stress intensity factors as a function of crystallographic orientation for an orthotropic material, which can be applied to any anisotropic material, if all the material constants are known. No prior assumption of plane stress or plane strain was made in developing this theory.
2. Mode *I*, (K_I), was always found to be greater for $[10\overline{1}]$ than for the $[\overline{1}2\overline{1}]$ orientation. For an orthotropic material, K_I was found to be non-zero at crack closure due to the coupling of the nodal displacements, whereas for an isotropic material, it was zero.
3. The magnitude of K_{II} for $[\overline{1}2\overline{1}]$ was found to be always greater than that for $[10\overline{1}]$ orientation, but the difference was not much.
4. Mode *III* SIF (K_{III}) existed because of the coupling of displacements at the crack tip due to anisotropy. K_{III} for $[10\overline{1}]$ was found to be much bigger than that for $[\overline{1}2\overline{1}]$ orientation for the Brazilian disk specimen. This plays an important role in calculation of effective K to predict the lifing of an anisotropic material.
5. The K_I and K_{III} values calculated were much higher for $[10\overline{1}]$ orientation, than those for $[\overline{1}2\overline{1}]$ orientation. Therefore a high value of K_{rss} can be expected for the $[10\overline{1}]$ direction than that for the $[\overline{1}2\overline{1}]$ direction, if we ignore

the difference of K_{II} values. This will result in high ΔK_{rss}, leading to fast crack growth rate for $[10\bar{1}]$ orientation than that for $[\bar{1}2\bar{1}]$ orientation.

6. SIFs calculated for $[\bar{1}2\bar{1}]$ crack orientation was found to be symmetric, which was due to symmetry of $\langle 121 \rangle$ about the mid plane as shown in Fig. 5–20 on page 50. Whereas due to unsymmetrical nature of $\langle 101 \rangle$ orientation, the calculated SIFs varied along the thickness for $[10\bar{1}]$ crack orientation. This variation can very well be used to predict the crack growth profile across the thickness.
7. The crack closure for $[10\bar{1}]$ orientation was found to be 18^0 whereas it was 30^0 for $[\bar{1}2\bar{1}]$ orientation for the Brazilian disk specimen, which shows the importance of knowledge of secondary orientation.
8. As shear decohesion is caused by dislocation motion, it was expected that the orientation of the crack plane must be related to the active slip plane(s). The fatigue damage parameter, K_{rss} was calculated for all the 12 primary slip systems for all the 3 Brazilian disk specimens. The $K_{rss,max}$ was found on the $\{111\}$ plane, which also happened to be the crack growth plane for all the 3 BD specimens. Therefore for a single active slip plane, the maximum resolved shear stress provides the primary driving force for dislocation motion, the shear decohesion process leading to crack growth process.
9. The parameter K_{rss} is well suited in identifying the active crack plane as well as predicting the microscopic crack growth direction. It is also an effective multiaxial crack driving force parameter.
10. The fatigue damage parameter, ΔK_{rss}, was calculated for the three Brazilian disk specimen and was plotted on log-log scale with da/dN and a linear region, region *II* (Paris region) was obtained. But the experimental data used to calculate ΔK_{rss} were not sufficient in number in region *II*. More data is

required to get the accurate value of parameter C and n of the Paris law. The equation obtained can be used to calculate the life of the material.

11. The method developed is not related to any specific geometry. Therefore it can be used for any kind of geometry and for any general anisotropic material, to calculate mixed mode SIFs at the crack tip and therefore crack growth rate and hence life of any material can be predicted.
12. Additional experimental data are required to study FCG on $\{111\}$ plane, $\langle 101 \rangle$ orientation. More data are needed in region *II* to get the accurate result to predict lifing. Also experimental data for crack plane orientations other than slip planes, e.g., $\langle 100 \rangle$, can be used to check the validity of the model.

Possible Directions for Future Work are given below:

- Incorporation of crack tip plasticity.
- FCG testing under mixed mode loading for a wider range of specimen geometries and orientations.
- FCG testing at high temperatures.

APPENDIX A
DISPLACEMENT FIELD EVALUATION FOR AN ANISOTROPIC ELASTIC SOLID UNDER GENERALIZED PLANE STRAIN CONDITION

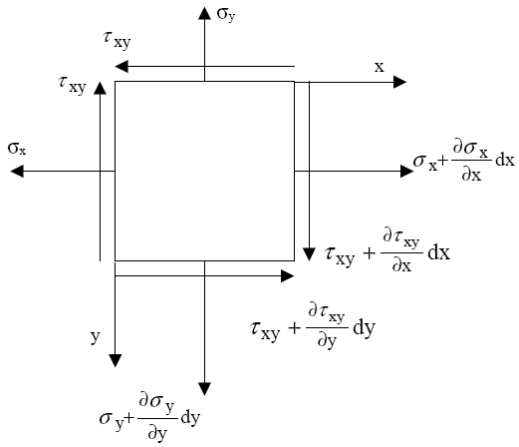

Figure A–1: Forces acting on a rectangular element with dimension $dx \times dy$ in equilibrium condition.

A generalized plane strain condition has been adopted for an anisotropic solid applicable to that of an FCC single crystal.[6] Let us consider a rectangular pipe like element with dimension $dx, dy, 1$. We assume that this body is under equilibrium under various forces. If body forces are X, Y per unit volume, then the equation of equilibrium of force along x and y direction can be written as followed,

Along $x-$axis.

$$\left(\sigma_x + \frac{\partial \sigma_x}{\partial y} dy\right) dx - \sigma_x dy + \left(\tau_{sy} + \frac{\partial \tau_{xy}}{\partial y} dy\right) dx - \tau_{xy} dx + X dx dy = 0 \qquad \text{(A.1)}$$

Along $y-$axis

$$\left(\sigma_x + \frac{\partial \sigma_x}{\partial x} dx\right) dy - \sigma_x dx + \left(\tau_{sy} + \frac{\partial \tau_{xy}}{\partial x} dx\right) dy - \tau_{xy} dy + Y dx dy = 0 \qquad \text{(A.2)}$$

The above two equations result as,

$$\begin{aligned} \frac{\partial \sigma_x}{\partial x} + \frac{\partial \tau_{xy}}{\partial y} + X &= 0 \\ \frac{\partial \tau_{xy}}{\partial x} + \frac{\partial \sigma_y}{\partial y} + Y &= 0 \end{aligned} \qquad \text{(A.3)}$$

Where X and Y are body forces (this force acts on entire body and constant throughout the body. e.g. gravitational force, magnetic force etc.), which can be defined as a derivative of potential function $\overline{U}$ as

$$\begin{aligned} X &= -\frac{\partial \overline{U}}{\partial x} \\ Y &= -\frac{\partial \overline{U}}{\partial y} \end{aligned} \qquad \text{(A.4)}$$

The components of stresses are denoted as X_n and Y_n (per unit area) and only depend on the two coordinates x and y. Now the fundamental system of equations of equilibrium to determine the state of stress and deformation of an elastic body (bounded by cylindrical surface) under the influence of body forces and stresses which are distributed along the surface can be given as:

$$\begin{aligned} \frac{\partial \sigma_x}{\partial x} + \frac{\partial \tau_{xy}}{\partial y} + X &= 0 \\ \frac{\partial \tau_{xy}}{\partial x} + \frac{\partial \sigma_y}{\partial y} + Y &= 0 \\ \frac{\partial \tau_{xz}}{\partial x} + \frac{\partial \tau_{yz}}{\partial y} &= 0 \end{aligned} \qquad \text{(A.5)}$$

The equation (A.4) is a result of summation of forces along X, Y and Z axes respectively.

The generalized Hooke's laws are

$$\begin{aligned}
\epsilon_x &= a_{11}\sigma_x + a_{12}\sigma_y + ... + a_{16}\tau_{xy} \\
\epsilon_y &= a_{21}\sigma_x + a_{22}\sigma_y + ... + a_{26}\tau_{xy} \\
\epsilon_z &= a_{31}\sigma_x + a_{32}\sigma_y + ... + a_{36}\tau_{xy} \\
\gamma_{yz} &= a_{41}\sigma_x + a_{42}\sigma_y + ... + a_{46}\tau_{xy} \\
\gamma_{zx} &= a_{51}\sigma_x + a_{52}\sigma_y + ... + a_{56}\tau_{xy} \\
\gamma_{xy} &= a_{61}\sigma_x + a_{62}\sigma_y + ... + a_{66}\tau_{xy}
\end{aligned} \tag{A.6}$$

The equation (A.6) is a function of x and y only for the given condition.

As

$$\begin{aligned}
\epsilon_z &= \frac{\partial w}{\partial z} \\
\gamma_{yz} &= \frac{\partial v}{\partial z} + \frac{\partial w}{\partial y} \\
\gamma_{zx} &= \frac{\partial w}{\partial x} + \frac{\partial u}{\partial z}
\end{aligned} \tag{A.7}$$

Let's integrate the 3^{rd} equation of Equation (A.6), keeping in mind that these are function of x and y only.

$$w = zD + W_0(x, y) \tag{A.8a}$$

Using the 2^{nd} equation of equation (A.7) in integration of the 4^{th} equation of equation (A.6) we get

$$v = -\frac{z^2}{2}\frac{\partial D}{\partial y} + z\left(a_{41}\sigma_x + a_{42}\sigma_y + ... + a_{46}\tau_{xy} - \frac{\partial W_0}{\partial y}\right) + V_0(x, y) \tag{A.8b}$$

Similarly with the help of the 3^{rd} equation of equation (A.7) and the 5^{th} equation of equation (A.6) we can find

$$u = -\frac{z^2}{2}\frac{\partial D}{\partial x} + z(a_{51}\sigma_x + a_{52}\sigma_y + ... + a_{56}\tau_{xy} - \frac{\partial W_0}{\partial x}) + U_0(x, y) \tag{A.8c}$$

Where

$$D = a_{31}\sigma_x + a_{32}\sigma_y + a_{33}\sigma_z + a_{34}\tau_{yz} + a_{35}\tau_{zx} + a_{36}\tau_{xy} \tag{A.9}$$

and U_0, V_0, W_0 are arbitrary function of x and y only.

As equations (A.8a, A.8b, A.8c) should satisfy the rest of the three equations of equation (A.6), let us substitute them in equation (A.6).

$$\begin{aligned}
\epsilon_x &= \frac{\partial u}{\partial x} = -\frac{z^2}{2}\frac{\partial^2 D}{\partial x^2} + z\frac{\partial}{\partial x}\left(a_{51}\sigma_x + a_{52}\sigma_y + ... + a_{56}\tau_{xy} - \frac{\partial W_0}{\partial x}\right) + \frac{\partial U_0}{\partial x} \\
\epsilon_y &= \frac{\partial v}{\partial y} = -\frac{z^2}{2}\frac{\partial^2 D}{\partial y^2} + z\frac{\partial}{\partial y}\left(a_{41}\sigma_x + a_{42}\sigma_y + ... + a_{46}\tau_{xy} - \frac{\partial W_0}{\partial y}\right) + \frac{\partial V_0}{\partial y} \\
\gamma_{xy} &= \frac{\partial u}{\partial y} + \frac{\partial v}{\partial x} = -z^2\frac{\partial^2 D}{\partial y \partial x} + z[\frac{\partial}{\partial y}\left(a_{51}\sigma_x + a_{52}\sigma_y + ... + a_{56}\tau_{xy} - \frac{\partial W_0}{\partial x}\right) + \\
&\quad ...\frac{\partial}{\partial x}\left(a_{41}\sigma_x + a_{42}\sigma_y + ... + a_{46}\tau_{xy} - \frac{\partial W_0}{\partial y}\right)] + \frac{\partial U_0}{\partial y} + \frac{\partial V_0}{\partial x}
\end{aligned} \tag{A.10}$$

Using equation (A.6) and equation (A.10) to compare the coefficients of z^2, z and z^0, as these are functions of x and y only, therefore at every point of z it must be same for same x and y, hence all the coefficients of z^2, z should be zero; we get

$$\frac{\partial^2 D}{\partial x^2} = 0; \qquad \frac{\partial^2 D}{\partial y^2} = 0; \qquad \frac{\partial^2 D}{\partial y \partial x} = 0 \tag{A.11}$$

$$\begin{aligned}
\frac{\partial}{\partial x}\left(a_{51}\sigma_x + a_{52}\sigma_y + ... + a_{56}\tau_{xy} - \frac{\partial W_0}{\partial x}\right) &= 0 \\
\frac{\partial}{\partial y}\left(a_{41}\sigma_x + a_{42}\sigma_y + ... + a_{46}\tau_{xy} - \frac{\partial W_0}{\partial y}\right) &= 0 \\
\frac{\partial}{\partial y}\left(a_{51}\sigma_x + a_{52}\sigma_y + ... + a_{56}\tau_{xy} - \frac{\partial W_0}{\partial x}\right) ... & \\
+\frac{\partial}{\partial x}\left(a_{41}\sigma_x + a_{42}\sigma_y + ... + a_{46}\tau_{xy} - \frac{\partial W_0}{\partial y}\right) &= 0
\end{aligned} \tag{A.12}$$

$$\begin{aligned} \frac{\partial U_0}{\partial x} &= a_{11}\sigma_x + a_{12}\sigma_y + ... + a_{16}\tau_{xy} \\ \frac{\partial V_0}{\partial y} &= a_{21}\sigma_x + a_{22}\sigma_y + ... + a_{26}\tau_{xy} \\ \frac{\partial U_0}{\partial y} + \frac{\partial V_0}{\partial x} &= a_{61}\sigma_x + a_{62}\sigma_y + ... + a_{66}\tau_{xy} \end{aligned} \tag{A.13}$$

As D is a function of x and y only, from equation (A.11) we can say that it is a linear function of x and y only.

$$D = A_1 x + B_1 y + C_1$$

where A_1, B_1, C_1 are arbitrary constants.

Further without any loss of generality we can write

$$D = a_{33}(Ax + By + C) \tag{A.14}$$

Where A, B, C are new arbitrary constants.

From equation (A.9) and equation (A.14) we can write

$$\sigma_z = Ax + By + C - \frac{1}{a_{33}}\left(a_{31}\sigma_x + a_{32}\sigma_y + a_{34}\tau_{yz} + a_{35}\tau_{zx} + a_{36}\tau_{xy}\right) \tag{A.15}$$

We can write equation (A.12) in the form

$$\frac{\partial M}{\partial x} = 0; \qquad \frac{\partial N}{\partial y} = 0; \qquad \frac{\partial M}{\partial y} + \frac{\partial N}{\partial x} = 0 \tag{A.16}$$

Where

$$\begin{aligned} M &= a_{51}\sigma_x + a_{52}\sigma_y + ... + a_{56}\tau_{xy} - \frac{\partial W_0}{\partial x} \\ N &= a_{41}\sigma_x + a_{42}\sigma_y + ... + a_{46}\tau_{xy} - \frac{\partial W_0}{\partial y} \end{aligned} \tag{A.17}$$

Integrating 1^{st} and 2^{nd}equations of equation (A.16) knowing that they are function of x and y only

$$\begin{aligned} M &= \alpha y + \omega_2 \\ N &= \overline{\theta} x - \omega_1 \end{aligned} \tag{A.18}$$

Where $\alpha, \overline{\theta}, \omega_1, \omega_2$ are the new arbitrary constants.

Using 3^{rd} equation of equation (13) and equation (15) we get

$$\alpha = -\overline{\theta}$$

Substituting α into equation (A.18) and using equation (A.17) we can write

$$\begin{aligned} a_{51}\sigma_x + a_{52}\sigma_y + ... + a_{56}\tau_{xy} - \frac{\partial W_0}{\partial x} &= -\overline{\theta} y + \omega_2 \\ a_{41}\sigma_x + a_{42}\sigma_y + ... + a_{46}\tau_{xy} - \frac{\partial W_0}{\partial y} &= \overline{\theta} x - \omega_1 \end{aligned} \tag{A.19}$$

We can write U_0, V_0, W_0 as a function of x and y without any loss of generality as

$$\begin{aligned} U_0 &= U - \omega_3 y + u_0 \\ V_0 &= V + \omega_3 x + v_0 \\ W_0 &= W + \omega_1 y - \omega_2 x + w_0 \end{aligned} \tag{A.20}$$

Here ω_3, u_0, v_0, w_0 are new arbitrary constants and U, V, W are functions of x and y.

Using equations (A.8a,A.19,A.20) we can write

$$\begin{aligned} u &= -\frac{A a_{33}}{2} z^2 - \overline{\theta} y z + U(x,y) + \omega_2 z - \omega_3 y + u_0 \\ v &= -\frac{B a_{33}}{2} z^2 + \overline{\theta} x z + V(x,y) + \omega_3 x - \omega_1 z + v_0 \\ w &= (Ax + By + C) a_{33} z + W(x,y) + \omega_1 y - \omega_2 x + w_0 \end{aligned} \tag{A.21}$$

Here the constants $\omega_1, \omega_2, \omega_3, u_0, v_0, w_0$ characterize only rigid displacements of the body and $\overline{\theta}$ is the relative angle of rotation about the $z-$axis. Constants A and B characterize the bending of the body in the $x-z$ and $y-z$ planes.

Substituting expression for equation (A.15) into equation (A.13) we can write

$$\begin{aligned}\frac{\partial U}{\partial x} &= a_{11}\sigma_x + a_{12}\sigma_y + a_{13}[Ax + By + C - \frac{1}{a_{33}}(a_{31}\sigma_x + a_{32}\sigma_y + \\ &\quad ...a_{34}\tau_{yz} + a_{35}\tau_{zx} + a_{36}\tau_{xy})] + a_{14}\tau_{yz} + a_{15}\tau_{xz} + a_{16}\tau_{xy}\end{aligned}$$

$$\begin{aligned}\Rightarrow \quad \frac{\partial U}{\partial x} &= \left(a_{11} - \frac{a_{13}}{a_{33}}a_{31}\right)\sigma_x + \left(a_{12} - \frac{a_{13}}{a_{33}}a_{32}\right)\sigma_y + \left(a_{14} - \frac{a_{13}}{a_{33}}a_{34}\right)\tau_{yz} \\ &\quad ... + \left(a_{15} - \frac{a_{13}}{a_{33}}a_{35}\right)\tau_{xz} + \left(a_{16} - \frac{a_{13}}{a_{33}}a_{36}\right)\tau_{xy} + a_{13}\left(Ax + By + C\right)\end{aligned}$$

$$\Rightarrow \frac{\partial U}{\partial x} = \beta_{11}\sigma_x + \beta_{12}\sigma_y + \beta_{14}\tau_{yz} + \beta_{15}\tau_{xz} + \beta_{16}\tau_{xy} + a_{13}\left(Ax + By + C\right) \quad \text{(A.22a)}$$

Similarly

$$\begin{aligned}\frac{\partial U}{\partial x} &= \beta_{21}\sigma_x + \beta_{22}\sigma_y + \beta_{24}\tau_{yz} + \beta_{25}\tau_{xz} + \beta_{26}\tau_{xy} \\ &\quad ... + a_{23}\left(Ax + By + C\right) \\ \frac{\partial U}{\partial y} + \frac{\partial V}{\partial x} &= \beta_{61}\sigma_x + \beta_{62}\sigma_y + \beta_{64}\tau_{yz} + \beta_{65}\tau_{xz} + \beta_{66}\tau_{xy} + ... \\ &\quad a_{63}\left(Ax + By + C\right) \quad \text{(A.22b)}\end{aligned}$$

Where

$$\beta_{ij} = a_{ij} - \frac{a_{i3}a_{j3}}{a_{33}} \qquad (i, j = 1, 2, 4, 5, 6) \quad \text{(A.23)}$$

Similarly substituting equation (A.15) into equation (A.19) we get

$$\begin{aligned}\frac{\partial W}{\partial x} &= \beta_{51}\sigma_x + \beta_{52}\sigma_y + \beta_{54}\tau_{yz} + \beta_{55}\tau_{xz} + \beta_{56}\tau_{xy} + a_{53}\left(Ax + By + C\right) + \overline{\theta}y \\ \frac{\partial W}{\partial y} &= \beta_{41}\sigma_x + \beta_{42}\sigma_y + \beta_{44}\tau_{yz} + \beta_{45}\tau_{xz} + \beta_{46}\tau_{xy} + a_{43}\left(Ax + By + C\right) - \overline{\theta}x\end{aligned}$$

The *strain compatibility relation for plane strain*, which is valid for small strains is given as,

$$\frac{\partial^2 \epsilon_y}{\partial x^2} + \frac{\partial^2 \epsilon_x}{\partial y^2} = \frac{\partial^2 \tau_{xy}}{\partial x \partial y} \tag{A.24}$$

Let us introduce two stress functions $F(x, y)$ and $\Psi(x, y)$, such that

$$\begin{aligned} \sigma_x &= \frac{\partial^2 F}{\partial y^2} + \overline{U}, \qquad \sigma_y = \frac{\partial^2 F}{\partial x^2} + \overline{U}, \\ \tau_{xy} &= -\frac{\partial^2 F}{\partial x \partial y}, \qquad \tau_{xz} = \frac{\partial \Psi}{\partial y}, \qquad \tau_{yz} = -\frac{\partial \Psi}{\partial x} \end{aligned} \tag{A.25}$$

Using equation (A.25) and equation (A.6), we can write

$$\begin{aligned} \frac{\partial^2 \epsilon_x}{\partial y^2} &= \beta_{11}\left(\frac{\partial^4 F}{\partial y^4} + \frac{\partial^2 \bar{U}}{\partial y^2}\right) + \beta_{12}\left(\frac{\partial^4 F}{\partial y^2 \partial x^2} + \frac{\partial^2 \bar{U}}{\partial y^2}\right) - \beta_{14}\frac{\partial^3 \Psi}{\partial y^2 \partial x} + \\ &\quad ...\beta_{15}\frac{\partial^3 \Psi}{\partial y^3} - \beta_{16}\frac{\partial^4 F}{\partial x \partial y^3} \\ \frac{\partial^2 \epsilon_y}{\partial x^2} &= \beta_{12}\left(\frac{\partial^4 F}{\partial x^2 \partial y^2} + \frac{\partial^2 \bar{U}}{\partial x^2}\right) + \beta_{22}\left(\frac{\partial^4 F}{\partial x^4} + \frac{\partial^2 \bar{U}}{\partial x^2}\right) - \beta_{24}\frac{\partial^3 \Psi}{\partial x^3} + \\ &\quad ...\beta_{25}\frac{\partial^3 \Psi}{\partial x^2 \partial y} - \beta_{26}\frac{\partial^4 F}{\partial x^3 \partial y} \\ \frac{\partial^2 \epsilon_{xy}}{\partial y \partial x} &= \beta_{16}\left(\frac{\partial^4 F}{\partial x \partial y^3} + \frac{\partial^2 \overline{U}}{\partial y \partial x}\right) + \beta_{26}\left(\frac{\partial^4 F}{\partial y \partial x^3} + \frac{\partial^2 \overline{U}}{\partial y \partial x}\right) - \beta_{26}\frac{\partial^3 \Psi}{\partial y \partial x^2} \\ &\quad ... + \beta_{56}\frac{\partial^3 \Psi}{\partial x \partial y^2} - \beta_{66}\frac{\partial^4 F}{\partial x^2 \partial y^2} \end{aligned} \tag{A.26}$$

Using Equation (A.24) and equation (A.26), we can further write

$$\begin{aligned} L_4 F + L_3 \Psi &= -(\beta_{12} + \beta_{22})\frac{\partial^2 \bar{U}}{\partial x^2} + (\beta_{16} + \beta_{26})\frac{\partial^2 \bar{U}}{\partial x \partial y} - (\beta_{11} + \beta_{12})\frac{\partial^2 \bar{U}}{\partial y^2} \\ L_3 F + L_2 \Psi &= -2\overline{\theta} + A a_{34} - B a_{35} + (\beta_{14} + \beta_{24})\frac{\partial \overline{U}}{\partial x} - (\beta_{15} + \beta_{25})\frac{\partial \overline{U}}{\partial y} \end{aligned}$$

In the absence of body force i. e. $\overline{U} = 0$,

$$\begin{aligned} L_4 F + L_3 \Psi &= 0 \\ L_3 F + L_2 \Psi &= 0 \end{aligned} \tag{A.27}$$

Where

$$\begin{aligned} L_2 &= \beta_{44}\frac{\partial^2}{\partial x^2} - 2\beta_{45}\frac{\partial^2}{\partial x \partial y} + \beta_{55}\frac{\partial^2}{\partial y^2}, \\ L_3 &= -\beta_{24}\frac{\partial^3}{\partial x^3} + (\beta_{25}+\beta_{46})\frac{\partial^3}{\partial x^2 \partial y} - (\beta_{14}+\beta_{56})\frac{\partial^3}{\partial x \partial y^2} + \beta_{15}\frac{\partial^3}{\partial y^3} \\ L_4 &= \beta_{22}\frac{\partial^4}{\partial x^4} - 2\beta_{26}\frac{\partial^4}{\partial x^3 \partial y} + (2\beta_{12}+\beta_{66})\frac{\partial^4}{\partial x^2 \partial y^2} - \\ & \quad ...2\beta_{16}\frac{\partial^4}{\partial x \partial y^3} + \beta_{11}\frac{\partial^4}{\partial y^4} \end{aligned} \tag{A.28}$$

Now the general solution of the system of equations can be written as

$$\begin{aligned} L_4 F + L_3 \psi &= 0 \\ L_3 F + L_2 \psi &= 0 \end{aligned} \tag{A.29}$$

In the presence of body forces,

$$\begin{aligned} F &= F' + F_0 \\ \psi &= \psi' + \psi_0 \end{aligned} \tag{A.30}$$

From the above two equations,

$$(L_4 L_2 - L_3^2) F' = 0 \tag{A.31}$$

The above sixth order operator can be broken into linear operators as,

$$D_6 D_5 D_4 D_3 D_2 D_1 F' = 0 \tag{A.32}$$

Where

$$D_x = \frac{\delta}{\delta x} - \mu_k \frac{\delta}{\delta x} \tag{A.33}$$

and μ_k are the roots of the equation which corresponds to the differential equation

$$l_4(\mu) l_2(\mu) - l_3^2(\mu) = 0 \tag{A.34}$$

where,

$$\begin{aligned} l_2(\mu) &= \beta_{55}\mu^2 + 2\beta_{45}\mu + \beta_{44} \\ l_3(\mu) &= \beta_{11}\mu^3 - (\beta_{14} + \beta_{56})\mu^2 + (\beta_{25} + \beta_{46})\mu - \beta_{24} \\ l_4(\mu) &= \beta_{11}\mu^4 - 2\beta_{16}\mu^3 + (2\beta_{12} + \beta_{66})\mu^2 - 2\beta_{26}\mu + \beta_{22} \end{aligned} \tag{A.35}$$

Now the integration of the sixth order is separated into six equations of the first order.

Assuming that all the roots(μ_k) are distinct, then

$$\begin{aligned} D_1 F' &= \phi_2, \\ D_2\phi_2 &= \phi_3, \\ D_3\phi_3 &= \phi_4, \\ D_4\phi_4 &= \phi_5, \\ D_5\phi_5 &= \phi_6, \end{aligned} \tag{A.36}$$

for the equation to satisfy,

$$D_6\phi_6 = 0 \tag{A.37}$$

The general integral is equal to an arbitrary function of the argument $x + \mu_6 y$ and is denoted by $f_6^v(x + \mu_6 y)$.

$$\phi_6 = f_6^v(x + \mu_6 y) \tag{A.38}$$

Therefore,

$$d_5\phi_5 = f_6^v(x + \mu_6 y) \tag{A.39}$$

Integrating the above equation, we get

$$\phi_5 = f_5^{iv}(x + \mu_5 y) + \frac{f_6^{iv}(x + \mu_6 y)}{\mu_6 - \mu_5} \tag{A.40}$$

ϕ_4, ϕ_3, ϕ_2 and F' can be defined in the same way.

The arbitrary function can be defined in terms of F' and ψ' in the following manner,

$$\begin{aligned} F' &= \sum_{k=1}^{6} F_k(x+\mu_k y) \\ \psi' &= \sum_{k=1}^{6} \psi_k(x+\mu_k y) \end{aligned} \tag{A.41}$$

Now from equation a and b

$$\psi_k(x+\mu_k y) = -\frac{l_3(\mu_k)}{l_2(\mu_k)} F_k'(x+\mu_k y) + a_k(x+\mu_k y) + b_k \tag{A.42}$$

where a_k and b_k are arbitrary constants.

Now there are four theorems, which are important for the theory of the equilibrium of a body bounded by a cylindrical surface.

Theorem 1: The equation $l_4(\mu) = 0$ cannot have real roots.

Theorem 2: The equation $l_2(\mu) = 0$ cannot have real roots.

Theorem 3: The equation $l_4(\mu)l_2(\mu) - l_3^2 = 0$ cannot have real roots.

Theorem 4: The equation $a_{11}\mu^4 - 2a_{16}\mu^3 + (2a_{12} + a_{66})\mu^2 - 2a_{26}\mu + a_{22} = 0$ cannot have real roots.

Based on the third theorem, we can show that the numbers are always complex or purely imaginary.

The general expression for the stress function can now be shown as,

$$\begin{aligned} F &= 2\,\mathrm{Re}[F_1(z_1) + F_2(z_2) + F_3(z_3)] + F_0 \\ \psi &= 2\,\mathrm{Re}[\lambda_1 F_1'(z_1) + \lambda_2 F_2'(z_2) + \frac{1}{\lambda_3} F_3'(z_3)] + \psi_0 \end{aligned} \tag{A.43}$$

Here $F_k(z_k)$ are analytic functions of the complex variables $z_k = x + \mu_k y$ (k=1,2,3) and $\lambda_1, \lambda_2, \lambda_3$ are the complex numbers equal to

$$\begin{aligned} \lambda_1 &= \frac{l_3(\mu_1)}{l_2(\mu_1)} \\ \lambda_2 &= \frac{l_3(\mu_2)}{l_2(\mu_2)} \\ \lambda_1 &= \frac{l_3(\mu_3)}{l4(\mu_3)} \end{aligned} \tag{A.44}$$

Now we introduce new functions of the complex variable z_k,

$$\phi_k(z_k) = F_k'(z_k) \qquad k = 1, 2$$

$$\phi_3(z_3) = \frac{1}{\lambda_3} F_3'(z_3) \tag{A.45}$$

Taking the derivative of F and ψ with respect to x and y respectively results as ,

$$\begin{aligned} \frac{\delta F}{\delta x} &= 2\,\mathrm{Re}[\phi_1(z_1) + \phi_2(z_2) + \lambda_3\phi_3(z_3)] + \frac{\delta F_0}{\delta x} \\ \frac{\delta F}{\delta y} &= 2\,\mathrm{Re}[\mu_1\phi_1(z_1) + \mu_2\phi_2(z_2) + \mu_3\lambda_3\phi_3(z_3)] + \frac{\delta F_0}{\delta y} \\ \frac{\delta F}{\delta x} &= 2\,\mathrm{Re}[\lambda_1\phi_1(z_1) + \lambda_2\phi_2(z_2) + \phi_3(z_3)] + \psi_0 \end{aligned} \tag{A.46}$$

Based on the above formulas, the general expressions for the components of stresses can be defined as,

$$\begin{aligned}
\sigma_x &= 2\,\mathrm{Re}[\mu_1^2\phi_1'(z_1) + \mu_2^2\phi_2'(z_2) + \mu_3^2\lambda_3\phi_3'(z_3)] + \frac{\delta^2 F_0}{\delta y^2} + \bar{U} \\
\sigma_y &= 2\,\mathrm{Re}[\phi_1'(z_1) + \phi_2'(z_2) + \lambda_3\phi_3'(z_3)] + \frac{\delta^2 F_0}{\delta x^2} + \bar{U} \\
\tau_{xy} &= 2\,\mathrm{Re}[\mu_1\phi_1'(z_1) + \mu_2\phi_2'(z_2) + \mu_3\lambda_3\phi_3'(z_3)] - \frac{\delta^2 F_0}{\delta xy} \\
\tau_{xz} &= 2\,\mathrm{Re}[\mu_1\lambda_1\phi_1'(z_1) + \mu_2\lambda_2\phi_2'(z_2) + \mu_3\phi_3'(z_3)] + \frac{\delta^2\psi_0}{\delta y} \\
\tau_{yz} &= -2\,\mathrm{Re}[\lambda_1\phi_1'(z_1) + \lambda_2\phi_2'(z_2) + \phi_3'(z_3)] - \frac{\delta^2\psi_0}{\delta y} \\
\sigma_z &= Ax + By + C - \frac{1}{a_{33}}(a_{13}\sigma_x + a_{23}\sigma_y + a_{34}\tau_{yz} + a_{35}\tau_{xz} + a_{36}\tau_{xy})
\end{aligned} \tag{A.47}$$

By substituting above equations and integrating the resulting equation, we find the functions U, V, W as

$$\begin{aligned}
U &= 2\,\mathrm{Re}\sum_{k=1}^{3} p_k\phi_k(z_k) + U^0 \\
V &= 2\,\mathrm{Re}\sum_{k=1}^{3} q_k\phi_k(z_k) + V^0 \\
W &= 2\,\mathrm{Re}\sum_{k=1}^{3} r_k\phi_k(z_k) + W^0
\end{aligned} \tag{A.48}$$

There for we can write

$$\begin{aligned}
p_k &= \beta_{12}\mu_k^2 + \beta_{12} - \beta_{16}\mu_k + \lambda_k(\beta_{15}\mu_k - \beta_{14}) \\
q_k &= \beta_{12}\mu_k + \frac{\beta_{22}}{\mu_k} - \beta_{26} + \lambda_k(\beta_{25} - \frac{\beta_{24}}{\mu_k}) \\
r_k &= \beta_{14}\mu_k + \frac{\beta_{24}}{\mu_k} - \beta_{46} + \lambda_k(\beta_{45} - \frac{\beta_{44}}{\mu_k})
\end{aligned} \tag{A.49}$$

k=1,2

$$
\begin{aligned}
p_3 &= \lambda_3(\beta_{11}\mu_3^2 + \beta_{12} - \beta_{16}\mu_3) + \beta_{15}\mu_3 - \beta_{14} \\
q_3 &= \lambda_3(\beta_{12}\mu_3 + \frac{\beta_{22}}{\mu_3} - \beta_{26}) + \beta_{25} - \frac{\beta_{24}}{\mu_3} \\
r_3 &= \lambda_3(\beta_{14}\mu_3 + \frac{\beta_{24}}{\mu_3} - \beta_{46}) + \beta_{45} - \frac{\beta_{44}}{\mu_3}
\end{aligned}
\tag{A.50}
$$

APPENDIX B
DETAILS OF SIF EQUATION FORMULATION

The state of stress and the displacement field near a crack tip is given by [28],

1. Inplane-symmetric loading

$$\begin{aligned}
\sigma_x &= \frac{k_1}{\sqrt{2\pi r}}\mathrm{Re}\left[\frac{\mu_1\mu_2}{\mu_1-\mu_2}\left(\frac{\mu_2}{\sqrt{\cos\theta+\mu_2\sin\theta}}-\frac{\mu_1}{\sqrt{\cos\theta+\mu_1\sin\theta}}\right)\right]\\
\sigma_y &= \frac{k_1}{\sqrt{2\pi r}}\mathrm{Re}\left[\frac{1}{\mu_1-\mu_2}\left(\frac{\mu_1}{\sqrt{\cos\theta+\mu_2\sin\theta}}-\frac{\mu_2}{\sqrt{\cos\theta+\mu_1\sin\theta}}\right)\right]\\
\tau_{yx} &= \frac{k_1}{\sqrt{2\pi r}}\mathrm{Re}\left[\frac{\mu_1\mu_2}{\mu_1-\mu_2}\left(\frac{1}{\sqrt{\cos\theta+\mu_1\sin\theta}}-\frac{1}{\sqrt{\cos\theta+\mu_2\sin\theta}}\right)\right] \qquad \text{(B.1)}\\
u &= k_1\sqrt{\frac{2r}{\pi}}\mathrm{Re}\left[\frac{1}{\mu_1-\mu_2}\left(\mu_1p_2\sqrt{\cos\theta+\mu_2\sin\theta}-\mu_2p_1\sqrt{\cos\theta+\mu_1\sin\theta}\right)\right]\\
v &= k_1\sqrt{\frac{2r}{\pi}}\mathrm{Re}\left[\frac{1}{\mu_1-\mu_2}\left(\mu_1q_2\sqrt{\cos\theta+\mu_2\sin\theta}-\mu_2q_2\sqrt{\cos\theta+\mu_1\sin\theta}\right)\right]\\
w &= 0 \qquad \text{(B.2)}
\end{aligned}$$

2. Inplane-skewsymmetric loading

$$\begin{aligned}
\sigma_x &= \frac{k_2}{\sqrt{2\pi r}}\mathrm{Re}\left[\frac{1}{\mu_1-\mu_2}\left(\frac{\mu_2^2}{\sqrt{\cos\theta+\mu_2\sin\theta}}-\frac{\mu_1^2}{\sqrt{\cos\theta+\mu_1\sin\theta}}\right)\right]\\
\sigma_y &= \frac{k_1}{\sqrt{2\pi r}}\mathrm{Re}\left[\frac{1}{\mu_1-\mu_2}\left(\frac{1}{\sqrt{\cos\theta+\mu_2\sin\theta}}-\frac{1}{\sqrt{\cos\theta+\mu_1\sin\theta}}\right)\right]\\
\tau_{xy} &= \frac{k_2}{\sqrt{2\pi r}}\mathrm{Re}\left[\frac{1}{\mu_1-\mu_2}\left(\frac{\mu_1}{\sqrt{\cos\theta+\mu_1\sin\theta}}-\frac{\mu_2}{\sqrt{\cos\theta+\mu_2\sin\theta}}\right)\right] \qquad \text{(B.3)}\\
u &= k_2\sqrt{\frac{2r}{\pi}}\mathrm{Re}\left[\frac{1}{\mu_1-\mu_2}\left(p_2\sqrt{\cos\theta+\mu_2\sin\theta}-p_1\sqrt{\cos\theta+\mu_1\sin\theta}\right)\right]\\
v &= k_2\sqrt{\frac{2r}{\pi}}\mathrm{Re}\left[\frac{1}{\mu_1-\mu_2}\left(q_2\sqrt{\cos\theta+\mu_2\sin\theta}-q_1\sqrt{\cos\theta+\mu_1\sin\theta}\right)\right]\\
w &= 0 \qquad \text{(B.4)}
\end{aligned}$$

3. Antiplane Shear loading

$$\begin{aligned}
\tau_{xz} &= -\frac{k_3}{\sqrt{2\pi r}}\mathrm{Re}\left[\frac{\mu_3}{\sqrt{\cos\theta+\mu_3\sin\theta}}\right] \\
\tau_{yz} &= k_3\sqrt{2\pi r}\mathrm{Re}\left[\frac{1}{\sqrt{\cos\theta+\mu_3\sin\theta}}\right] \qquad \text{(B.5)} \\
u &= 0 \\
v &= 0 \\
w &= k_3\sqrt{\frac{2r}{\pi}}\mathrm{Re}\left[\frac{\sqrt{\cos\theta+\mu_3\sin\theta}}{c_{45}+\mu_3 c_{44}}\right] \qquad \text{(B.6)}
\end{aligned}$$

where,

$$\begin{aligned}
p_j &= a_{11}\mu_j^2 + a_{12} - a_{16}\mu_j \\
q_j &= a_{12}\mu_j + \frac{a_{22}}{\mu_j} - a_{26}
\end{aligned}$$

μ_1 and μ_2 are the two roots with positive imaginary parts as defined by the equation

$$a_{11}\mu^4 - 2a_{16}\mu^3 + (2a_{12}+a_{66})\mu^2 - 2a_{26}\mu + a_{22} = 0$$

and μ_3 is the root of the characteristic equation [26]

$$\begin{aligned}
a_{55}\mu^2 - 2a_{45}\mu + a_{44} &= 0 \\
\text{or[28]} & \\
c_{44}\mu^2 + 2c_{45}\mu + c_{55} &= 0
\end{aligned}$$

The relative crack face displacement field equation (top face relative to the bottom face, i.e. prime with respect to unprime as shown in Fig. 4–3 on page 34) for the crack tip element is given by Manu and Ingraffea as [29],

- Inplane crack opening displacement for Mode I loading

$$\begin{aligned}
v = {} & [2v_B - v_C + 2v_E - v_F + v_D + \tfrac{1}{2}\eta(-4v_B + v_C + 4v_E - v_F) + \tfrac{1}{2}\eta^2(v_F \\
& + v_C - 2v_D)]\sqrt{\tfrac{r}{L_1}}) + [(\eta-1)(2v_B - v_C) - (1+\eta)(2v_E - v_F)]\tfrac{r}{L_1}
\end{aligned} \qquad \text{(B.7)}$$

- Inplane crack sliding displacement for Mode II loading

$$u = [2u_B - u_C + 2u_E - u_F + u_D + \tfrac{1}{2}\eta(-4u_B + u_C + 4u_E - u_F) + \tfrac{1}{2}\eta^2 \ldots (u_F + u_C - 2u_D)]\sqrt{\tfrac{r}{L_1}}) + [(\eta - 1)(2u_B - u_C) - (1 + \eta)(2u_E - u_F)]\tfrac{r}{L_1} \quad \text{(B.8)}$$

- Antiplane crack tearing displacement for Mode III loading

$$w = [2w_B - w_C + 2w_E - w_F + w_D + \tfrac{1}{2}\eta(-4w_B + w_C + 4w_E - w_F) + \tfrac{1}{2}\eta^2 \ldots (w_F + w_C - 2w_D)]\sqrt{\tfrac{r}{L_1}}) + [(\eta - 1)(2w_B - w_C) - (1 + \eta)(2w_E - w_F)]\tfrac{r}{L_1} \quad \text{(B.9)}$$

The displacement field of the crack faces ($\theta = 180^0$) near the crack tip, due to mixed mode loading, can be given by superposing the displacement equations (B.2, B.4, B.6) as

$$\begin{Bmatrix} u \\ v \\ w \end{Bmatrix} = \begin{bmatrix} Re[\frac{i}{\mu_1 - \mu_2}(\mu_1 p_2 - \mu_2 p_1)] & Re[\frac{i}{\mu_1 - \mu_2}(p_2 - p_1)] & 0 \\ Re[\frac{i}{\mu_1 - \mu_2}(\mu_1 q_2 - \mu_2 q_1)] & Re[\frac{i}{\mu_1 - \mu_2}(q_2 - q_1)] & 0 \\ 0 & 0 & \frac{1}{\sqrt{c_{44}c_{55} - c_{45}^2}} \end{bmatrix} \ldots \times \begin{Bmatrix} K_I \\ K_{II} \\ K_{III} \end{Bmatrix} \sqrt{\frac{2r}{\pi}} \quad \text{(B.10)}$$

Equation based on the like powers of r as above (i.e. $\sqrt{r}$), can be written from equations (B.7,B.8,B.9) as

$$\left\{\begin{array}{c} u \\ v \\ w \end{array}\right\} = \left\{\begin{array}{r} 2u_B - u_C + 2u_E - u_F + u_D + \frac{1}{2}\eta(-4u_B + u_C + 4u_E - \ldots \\ u_F) + \frac{1}{2}\eta^2(u_F + u_C - 2u_D) \\ 2v_B - v_C + 2v_E - v_F + v_D + \frac{1}{2}\eta(-4v_B + v_C + 4v_E - \ldots \\ v_F) + \frac{1}{2}\eta^2(v_F + v_C - 2v_D) \\ 2w_B - w_C + 2w_E - w_F + w_D + \frac{1}{2}\eta(-4w_B + w_C + 4w_E - \ldots \\ w_F) + \frac{1}{2}\eta^2(w_F + w_C - 2w_D) \end{array}\right\} \sqrt{\frac{r}{L_1}} \tag{B.11}$$

Equating equations (B.10) and (B.11), the mixed-mode stress intensity factors can be found as

$$\left\{\begin{array}{c} K_I \\ K_{II} \\ K_{III} \end{array}\right\} = [B]^{-1}\,[A]\sqrt{\frac{\pi}{2L_1}} \tag{B.12}$$

Where $\{A\}$ is given as

$$\{A\} = \left\{\begin{array}{r} 2u_B - u_C + 2u_E - u_F + u_D + \frac{1}{2}\eta(-4u_B + u_C + 4u_E - u_F) + \ldots \\ \frac{1}{2}\eta^2(u_F + u_C - 2u_D) \\ 2v_B - v_C + 2v_E - v_F + v_D + \frac{1}{2}\eta(-4v_B + v_C + 4v_E - v_F) + \ldots \\ \frac{1}{2}\eta^2(v_F + v_C - 2v_D) \\ 2w_B - w_C + 2w_E - w_F + w_D + \frac{1}{2}\eta(-4w_B + w_C + 4w_E - w_F) + \ldots \\ \frac{1}{2}\eta^2(w_F + w_C - 2w_D) \end{array}\right\} \tag{B.13}$$

and $[B]^{-1}$ is defined as

$$[B]^{-1} = \begin{bmatrix} Re[\frac{i}{\mu_1-\mu_2}(q_2-q_1)]\frac{1}{D} & Re[\frac{-i}{\mu_1-\mu_2}(p_2-p_1)]\frac{1}{D} & 0 \\ Re[\frac{-i}{\mu_1-\mu_2}(\mu_1 q_2-\mu_2 q_1)]\frac{1}{D} & Re[\frac{i}{\mu_1-\mu_2}(\mu_1 p_2-\mu_2 p_1)]\frac{1}{D} & 0 \\ 0 & 0 & \sqrt{c_{44}c_{55}-c_{45}^2} \end{bmatrix} \tag{B.14}$$

and D is the determinant of the equation

$$D = \begin{vmatrix} Re[\frac{i}{\mu_1-\mu_2}(\mu_1 p_2-\mu_2 p_1)] & Re[\frac{i}{\mu_1-\mu_2}(p_2-p_1)] \\ Re[\frac{i}{\mu_1-\mu_2}(\mu_1 q_2-\mu_2 q_1)] & Re[\frac{i}{\mu_1-\mu_2}(q_2-q_1)] \end{vmatrix} \tag{B.15}$$

Let,

$$\sigma_z = \frac{1}{\sqrt{2\pi r}}(d_{31}K_I + d_{32}K_{II} + d_{33}K_{III}) \tag{B.16}$$

then superposing the stresses, given in equations (B.1,B.3, B.5, B.16), due to mixed-mode loading, the state of stress at any point around the crack tip can be given as

$$\begin{Bmatrix} \sigma_x \\ \sigma_y \\ \sigma_z \\ \tau_{yz} \\ \tau_{zx} \\ \tau_{xy} \end{Bmatrix} = \frac{1}{\sqrt{2\pi r}} \begin{bmatrix} d_{11} & d_{12} & 0 \\ d_{21} & d_{22} & 0 \\ d_{31} & d_{32} & d_{33} \\ 0 & 0 & d_{43} \\ 0 & 0 & d_{53} \\ d_{61} & d_{62} & 0 \end{bmatrix} \cdot \begin{Bmatrix} K_I \\ K_{II} \\ K_{III} \end{Bmatrix} \tag{B.17}$$

where,

$$d_{11} = \mathrm{Re}\left[\frac{\mu_1\mu_2}{\mu_1-\mu_2}\left(\frac{\mu_2}{b_2}-\frac{\mu_1}{b_1}\right)\right] \qquad d_{12} = \mathrm{Re}\left[\frac{1}{\mu_1-\mu_2}\left(\frac{\mu_2^2}{b_2}-\frac{\mu_1^2}{b_1}\right)\right]$$

$$d_{21} = \mathrm{Re}\left[\frac{1}{\mu_1-\mu_2}\left(\frac{\mu_1}{b_2}-\frac{\mu_2}{b_1}\right)\right] \qquad d_{22} = \mathrm{Re}\left[\frac{1}{\mu_1-\mu_2}\left(\frac{1}{b_2}-\frac{1}{b_1}\right)\right]$$

$$d_{43} = \mathrm{Re}\left[\frac{1}{b_3}\right] \qquad d_{53} = -\mathrm{Re}\left[\frac{\mu_3}{b_3}\right]$$

$$d_{61} = \mathrm{Re}\left[\frac{\mu_1\mu_2}{\mu_1-\mu_2}\left(\frac{1}{b_1}-\frac{1}{b_2}\right)\right] \qquad d_{62} = \mathrm{Re}\left[\frac{1}{\mu_1-\mu_2}\left(\frac{\mu_1}{b1}-\frac{\mu_2}{b2}\right)\right]$$

$$b_i = \sqrt{\cos(\theta)+\mu_i\sin(\theta)} \qquad i = 1,2,3$$

μ_1 and μ_2 are the two roots with positive imaginary parts as defined by the equation

$$a_{11}\mu^4 - 2a_{16}\mu^3 + (2a_{12}+a_{66})\mu^2 - 2a_{26}\mu + a_{22} = 0 \tag{B.18}$$

and μ_3 is the root of the characteristic equation [26]

$$a_{55}\mu^2 - 2a_{45}\mu + a_{44} = 0 \tag{B.19}$$

Also σ_z can be expressed from A.6 based on plane strain assumption ($\epsilon_z = 0$) as

$$\sigma_z = -\frac{1}{a_{33}}\left(a_{31}\sigma_x + a_{32}\sigma_y + a_{34}\tau_{yz} + a_{35}\tau_{zx} + a_{36}\tau_{xy}\right) \tag{B.20}$$

Where,

$$\begin{aligned}
\sigma_x &= \tfrac{1}{\sqrt{2\pi r}}(d_{11}K_I + d_{12}K_{II}) \\
\sigma_y &= \tfrac{1}{\sqrt{2\pi r}}(d_{21}K_I + d_{22}K_{II}) \\
\tau_{yz} &= \tfrac{1}{\sqrt{2\pi r}}d_{43}K_{III} \\
\tau_{xz} &= \tfrac{1}{\sqrt{2\pi r}}d_{53}K_{III} \\
\tau_{xy} &= \tfrac{1}{\sqrt{2\pi r}}(d_{61}K_I + d_{62}K_{II})
\end{aligned} \tag{B.21}$$

From equations (B.20) and (B.21) it can be written,

$$\begin{aligned}
\sigma_z = -\frac{1}{\sqrt{2\pi r}}\Big(&\frac{d_{11}a_{13}+d_{21}a_{23}+d_{61}a_{36}}{a_{33}}K_I + \frac{d_{12}a_{13}+d_{22}a_{23}+d_{62}a_{36}}{a_{33}}K_{II} + \dots \\
&+\frac{d_{43}a_{34}+d_{53}a_{35}}{a_{33}}K_{III}\Big)
\end{aligned} \tag{B.22}$$

Equating the coefficients of K_I, K_{II} and K_{III} in equation (B.16) and (B.22), it can be found

$$d_{3j} = \begin{cases} -\dfrac{d_{1j}a_{13} + d_{2j}a_{23} + d_{6j}a_{36}}{a_{33}} & \text{Plane Strain} \qquad j = 1, 2 \end{cases}$$

$$d_{33} = \begin{cases} -\dfrac{d_{43}a_{34} + d_{53}a_{35}}{a_{33}} & \text{Plane Strain} \end{cases}$$

For plane stress condition ($\sigma_z = 0$).

APPENDIX C
ANSYS PROGRAM

```
!$$$$$$$$$$$$$$$$$$$$$$$$$$$$$$$$$$$$$$$$$$$$$$$$$$$$$$$$$$$$$$$$$$$$$$$
!  File Created by Srikant Ranjan                                      $
!  Date 03/10/2005                                                     $
!  This is for the <-12-1> Orthotropic Brazilian    $
!  Disk for PWA 1422. It has different Crack Lengths$
!  at three different angles. The goal is to find   $
!  the delta_K to plot against da/dN                $
!$$$$$$$$$$$$$$$$$$$$$$$$$$$$$$$$$$$$$$$$$$$$$$$$$$$$$$$$$$$$$$$$$$$$$$$


/clear
/INQUIRE,user,USER
/TLABEL,-.9,-.9,Srikant is running the 4th file, 36 more to go!


/filename,mirror
! Defining parameters in British inch unit system and angle in deg
/units,BIN
*afun,deg
!Disk dimension
R=0.55
thick=0.1
discr=0.55
```

```
!Crack dimension
Crack=R*discr
! Force angle with crack
theta=12

load=1000

!$$$$$$$$$$$$$$$$$$$$$$$$$$$$$$$$$$$$$$$$$$$$$$$$$$$$$$$$$$$$$
! Directional cosines for the x,y axis of the      $
!orthotropic material for <-12-1> orientation      $
!$$$$$$$$$$$$$$$$$$$$$$$$$$$$$$$$$$$$$$$$$$$$$$$$$$$$$$$$$$$$$

*SET,x1,-1/sqrt(6)
*SET,x2,1/sqrt(3)
*SET,x3,1/sqrt(2)
*SET,y1,sqrt(2/3)
*SET,y2,1/sqrt(3)
*SET,y3,0

/prep7

pivcheck,off
!$$$$$$$$$$$$$$$$$$$$$$$$$$$$$$$$$$$$$$$$$$$$$$$$$$$$$$$$$$$$$
!  Defining Orthotropic material properties     $$$$$
!$$$$$$$$$$$$$$$$$$$$$$$$$$$$$$$$$$$$$$$$$$$$$$$$$$$$$$$$$$$$$

mp,ex,1,0.154e8
```

```
mp,ey,1,0.154e8
mp,ez,1,0.154e8
mp,nuxy,1,0.4009
mp,nuyz,1,0.4009
mp,nuxz,1,0.4009
!Defining Shear Modulus 'g' for Orthotropic material
*SET,g,0.157e8
mp,gxy,1,g
mp,gyz,1,g
mp,gxz,1,g

m=0
a=0.1
i=1
k,i
i=i+1

!for first circular arc
k,i,a/5
i=i+1
l,2,1
m=m+1
lesize,m,0.005236/2
k,i,,a/5
l,i-2,i
m=m+1
lesize,m,0.005236/2
```

```
larc,i-1,i,1,a/5
m=m+1
lesize,m,,3
i=i+1
al,m,m-1,m-2

!for second circular arc
k,i,a
l,i-2,i
i=i+1
m=m+1
lesize,m,,,5
k,i,,a
l,i-2,i
m=m+1
lesize,m,,,5
larc,i-1,i,1,a
m=m+1
lesize,m,,3
a=a+0.1
i=i+1
al,m,m-1,m-2,m-3

!for third circular arc
k,i,a
l,i-2,i
i=i+1
```

```
m=m+1
lesize,m,,,5
k,i,,a
l,i-2,i
m=m+1
lesize,m,,,5
larc,i-1,i,1,a
m=m+1
lesize,m,,3
a=a+0.0945
i=i+1
al,m,m-1,m-2,m-3

!for fourth circular arc
k,i,a
l,i-2,i
i=i+1
m=m+1
lesize,m,,,5
k,i,,a
l,i-2,i
m=m+1
lesize,m,,,5
larc,i-1,i,1,a
m=m+1
ldiv,m,1/30,51,,0
m=m+1
```

```
lesize,m,,3
a=a+0.016
i=i+1
al,m,m-1,m-2,m-3,m-4

!for fifth circular arc
k,i,a
l,i-2,i
i=i+1
m=m+1
k,i,,a
l,i-2,i
m=m+1
larc,i-1,i,1,a
m=m+1
ldiv,m,1/30,52,,0
m=m+1
lesize,m,,3
a=a+0.1395
i=i+1

!for sixth circular arc
k,i,a
l,i-2,i
i=i+1
m=m+1
lesize,m,,,6
```

```
k,i,,a
l,i-2,i
m=m+1
lesize,m,,,6
larc,i-1,i,1,a
m=m+1
lesize,m,,3
a=a+0.1
i=i+1
al,m,m-1,m-2,m-3,m-4

!for seventh circular arc
k,i,a
l,i-2,i
i=i+1
m=m+1
lesize,m,,,6
k,i,,a
l,i-2,i
m=m+1
lesize,m,,,6
larc,i-1,i,1,a
m=m+1
lesize,m,,3
al,m,m-1,m-2,m-3

l,51,52
```

```
m=m+1

ldiv,14,1,50,2,0

al,13,15,17,24
al,14,12,24,16,25

kscon,50,crack/80,1

asel,all

!Keypoints 20 and 21 define the matrl coord frame in the crack
!coordinate system
k,100,x1,x2,x3 k,101,y1,y2,y3 cskp,30,0,1,100,101

csys,0

!Select Element%
et,1,plane82,,,3  !6node quad 2d w/thick (keyopt 3) option
r,1,thick
!solid95: 20 nodes, 3d brick element for crack tip singularity
et,2,solid95

!Select element csys
esys,30

!Mesh
```

```
type,1
real,1
mat,1

SMRTSIZE,1
amesh,2,7
smrtsize,off
esize,0.1*3.14159265/150
amesh,1
amesh,8

!Creating symmetric geometry about y-z plane
ARSYM, x , all , , , , 0 , 0

!selecting lines and merging them at common joint
lsel, s , loc , x , 0
nsll, s , 1
nummrg,all

asel, all

!Creating symmetric geometry about x-z plane
ARSYM , y , all , , , , 0 , 0

!selecting lines and merging them at common joint
lsel, s , loc , y , 0
lsel, r , loc , x , crack ,  discr
```

```
nsll, s , 1
nummrg, all

lsel, s , loc , y , 0
lsel, r , loc , x , -crack ,  -discr
nsll, s , 1
nummrg, all

!Defining keypoint for force orientation with crack
k, 200 , discr*cos(theta) , discr*sin(theta)
k, 201 , , discr
asel,all

!======================
!3d meshing
type , 2
mat, 1
esize, , 4

!generating volume surrounded by area
vext, 1 , 32 , , 0 , 0 , thick

esel,all
asel,all
aclear,1,32

eplot,all
```

```
save

!$$$$$$$$$$$$$$$$$$$$$$$$$$$$$$$$$$$$$$$$$$$$$$$$$$$$$$$$$$$$$$$$$$$$$$$
!  Applying Loads on the Model                    $$$$$
!$$$$$$$$$$$$$$$$$$$$$$$$$$$$$$$$$$$$$$$$$$$$$$$$$$$$$$$$$$$$$$$$$$$$$$$

c*** Creating the load coordinate frame
cskp,40,0,1,200,201

nsel,all
! Rotating all the nodes to apply the b.cs
nrotat,all

nsel,s,loc,x,discr,discr+discr/100
nsle,u,mid
cm,node1,node
nsel,s,loc,x,-discr,-2*discr
nsle,u,mid
cm,node2,node
!selecting the component made up of the top nodes
cmsel,s,node1
!Applying load to the right most nodes
f,all,fx,-load/5
!Applying b.c. (uy=0) to the right most nodes
d,all,uy,0
!Applying b.c. (uz=0) to the right most center node
nsel,r,loc,z,thick/2
```

```
d,all,uz,0

!selecting the component made up of the bottom nodes
cmsel,s,node2
!Applying load to the left most nodes
f,all,fx,load/5
!Applying b.c. (uy=0) to the left most nodes
d,all,uy,0
!Applying b.c. (uz=0) to the left most center node
nsel,r,loc,z,thick/2
d,all,uz,0

!begin setup for running
csys,0
esel,all
nsel,all
save

/solu
solve
save
finish

!$$$$$$$$$$$$$$$$$$$$$$$$$$$$$$$$$$$$$$$$$$$$$$$$$$$$$$$$
!Running Post Processor and obtaining the       $$$$$
!Relative Crack Plane Nodal Displacements       $$$$$
!$$$$$$$$$$$$$$$$$$$$$$$$$$$$$$$$$$$$$$$$$$$$$$$$$$$$$$$$
```

```
/post1
set,last
csys,0
rsys,0

!$$$$$$$$$$$$$$$$$$$$$$$$$$$$$$$$$$$$$$$$$$$$$$$$$$$$
!Running Post Processor and obtaining the       $$$$$
!Relative Crack Plane Nodal Displacements       $$$$$
!$$$$$$$$$$$$$$$$$$$$$$$$$$$$$$$$$$$$$$$$$$$$$$$$$$$$
/post1
set,last
csys,0
rsys,0

nsel,s,loc,y,0
nsel,r,loc,z
nsel,r,loc,x,crack-(crack/320),crack-(crack/321)
*GET,Nb1,NODE,0,NUM,Min
*GET,Nb1p,NODE,0,NUM,Max

nsel,s,loc,y,0
nsel,r,loc,z
nsel,r,loc,x,crack-(crack/80),crack-(crack/81)
*GET,Nc1,NODE,0,NUM,Min
*GET,Nc1p,NODE,0,NUM,Max

nsel,s,loc,y,0
```

```
nsel,r,loc,z,thick/8
nsel,r,loc,x,crack-(crack/80),crack-(crack/81)
*GET,Nd1,NODE,0,NUM,Min
*GET,Nd1p,NODE,0,NUM,Max

nsel,s,loc,y,0
nsel,r,loc,z,2*thick/8
nsel,r,loc,x,crack-(crack/320),crack-(crack/321)
*GET,Ne1,NODE,0,NUM,Min
*GET,Ne1p,NODE,0,NUM,Max

nsel,s,loc,y,0
nsel,r,loc,z,2*thick/8
nsel,r,loc,x,crack-(crack/80),crack-(crack/81)
*GET,Nf1,NODE,0,NUM,Min
*GET,Nf1p,NODE,0,NUM,Max

!==================================

nsel,s,loc,y,0
nsel,r,loc,z,3*thick/8
nsel,r,loc,x,crack-(crack/80),crack-(crack/81)
*GET,Nd4,NODE,0,NUM,Min
*GET,Nd4p,NODE,0,NUM,Max

!====================================
```

```
nsel,s,loc,y,0
nsel,r,loc,z,4*thick/8
nsel,r,loc,x,crack-(crack/320),crack-(crack/321)
*GET,Nb2,NODE,0,NUM,Min
*GET,Nb2p,NODE,0,NUM,Max

nsel,s,loc,y,0
nsel,r,loc,z,4*thick/8
nsel,r,loc,x,crack-(crack/80),crack-(crack/81)
*GET,Nc2,NODE,0,NUM,Min
*GET,Nc2p,NODE,0,NUM,Max

nsel,s,loc,y,0
nsel,r,loc,z,5*thick/8
nsel,r,loc,x,crack-(crack/80),crack-(crack/81)
*GET,Nd2,NODE,0,NUM,Min
*GET,Nd2p,NODE,0,NUM,Max

nsel,s,loc,y,0
nsel,r,loc,z,6*thick/8
nsel,r,loc,x,crack-(crack/320),crack-(crack/321)
*GET,Ne2,NODE,0,NUM,Min
*GET,Ne2p,NODE,0,NUM,Max

nsel,s,loc,y,0
nsel,r,loc,z,6*thick/8
nsel,r,loc,x,crack-(crack/80),crack-(crack/81)
```

```
*GET,Nf2,NODE,0,NUM,Min
*GET,Nf2p,NODE,0,NUM,Max

!====================================

nsel,s,loc,y,0
nsel,r,loc,z,7*thick/8
nsel,r,loc,x,crack-(crack/80),crack-(crack/81)
*GET,Nd3,NODE,0,NUM,Min
*GET,Nd3p,NODE,0,NUM,Max

!==================================

nsel,s,loc,y,0
nsel,r,loc,z,8*thick/8
nsel,r,loc,x,crack-(crack/320),crack-(crack/321)
*GET,Nb3,NODE,0,NUM,Min
*GET,Nb3p,NODE,0,NUM,Max

nsel,s,loc,y,0
nsel,r,loc,z,8*thick/8
nsel,r,loc,x,crack-(crack/80),crack-(crack/81)
*GET,Nc3,NODE,0,NUM,Min
*GET,Nc3p,NODE,0,NUM,Max

!====================================
```

```
!$$$$$$$$$$$$$$$$$$$$$$$$$$$$$$$$$$$$$$$$$$$$$$$$$$$$$$$$$$$$$$$$$$$$$$$
c***  Defining parameters for relative distance   $$$
C***  between nodes at crack face near crack tip  $$$
c***  in all directions                           $$$
!$$$$$$$$$$$$$$$$$$$$$$$$$$$$$$$$$$$$$$$$$$$$$$$$$$$$$$$$$$$$$$$$$$$$$$$



c***  Relative displacement of Nodes at location z=0
Bx1=ux(Nb1)-ux(Nb1p)
By1=uy(Nb1)-uy(Nb1p)
Bz1=uz(Nb1)-uz(Nb1p)

Cx1=ux(Nc1)-ux(Nc1p)
Cy1=uy(Nc1)-uy(Nc1p)
Cz1=uz(Nc1)-uz(Nc1p)

c***  Relative displacement of Nodes at location z=thick/10
Dx1=ux(Nd1)-ux(Nd1p)
Dy1=uy(Nd1)-uy(Nd1p)
Dz1=uz(Nd1)-uz(Nd1p)

c***  Relative displacement of Nodes at location z=2*thick/10
Ex1=ux(Ne1)-ux(Ne1p)
Ey1=uy(Ne1)-uy(Ne1p)
Ez1=uz(Ne1)-uz(Ne1p)

Fx1=ux(Nf1)-ux(Nf1p)
```

```
Fy1=uy(Nf1)-uy(Nf1p)
Fz1=uz(Nf1)-uz(Nf1p)

c***  Relative displacement of Nodes at location z=3*thick/10
Dx4=ux(Nd4)-ux(Nd4p)
Dy4=uy(Nd4)-uy(Nd4p)
Dz4=uz(Nd4)-uz(Nd4p)

c***  Relative displacement of Nodes at location z=4*thick/10
Bx2=ux(Nb2)-ux(Nb2p)
By2=uy(Nb2)-uy(Nb2p)
Bz2=uz(Nb2)-uz(Nb2p)

Cx2=ux(Nc2)-ux(Nc2p)
Cy2=uy(Nc2)-uy(Nc2p)
Cz2=uz(Nc2)-uz(Nc2p)

c***  Relative displacement of Nodes at location z=5*thick/10
Dx2=ux(Nd2)-ux(Nd2p)
Dy2=uy(Nd2)-uy(Nd2p)
Dz2=uz(Nd2)-uz(Nd2p)

c***  Relative displacement of Nodes at location z=6*thick/10
Ex2=ux(Ne2)-ux(Ne2p)
Ey2=uy(Ne2)-uy(Ne2p)
Ez2=uz(Ne2)-uz(Ne2p)
```

```
Fx2=ux(Nf2)-ux(Nf2p)

Fy2=uy(Nf2)-uy(Nf2p)

Fz2=uz(Nf2)-uz(Nf2p)


c***  Relative displacement of Nodes at location z=7*thick/10

Dx3=ux(Nd3)-ux(Nd3p)

Dy3=uy(Nd3)-uy(Nd3p)

Dz3=uz(Nd3)-uz(Nd3p)


c***  Relative displacement of Nodes at location z=8*thick/10

Bx3=ux(Nb3)-ux(Nb3p)

By3=uy(Nb3)-uy(Nb3p)

Bz3=uz(Nb3)-uz(Nb3p)


Cx3=ux(Nc3)-ux(Nc3p)

Cy3=uy(Nc3)-uy(Nc3p)

Cz3=uz(Nc3)-uz(Nc3p)


parsav,scalar,parameters,txt


save

finish
```

REFERENCES

[1] J. Moroso. Effect of secondary crystal orientation on fatigue crack growth in single crystal nickel turbine blade superalloys. Master's thesis, University of Florida, May 1999.

[2] Daniel P. Deluca and C. Annis. Fatigue in single crystal nickel superalloys. Technical Report FR23800, Office of Naval Research, Department of the Navy, August 1995.

[3] J. R. Davis. *ASM Specialty Handbook: Heat-Resistant Materials*. ASM International, Materials Park, Ohio, 1997.

[4] D. C. Stouffer and L. T. Dame. *Inelastic Deformation of Metals: Models, Mechanical properties, and Metallurgy*. John Wiley & Sons, New York, 1996.

[5] S. Gunturi. High temperature alloys. http://www.msm.cam.ac.uk/mech-prop/sats.html, University of Cambridge, May 2002.

[6] S. G. Lekhnitskii. *Theory of Elasticity of an Anisotropic Elastic Body*. Holden-Day Inc., 1963.

[7] G. Dieter. *Mechanical Metallurgy*. McGraw-Hill Science/Engineering, 3rd edition, 1986.

[8] F. Ebrahimi and L. Forero. The effect of microstructure on strain rate sensitivity of nickel. In *Symposium on Fatigue of High Temperature Materials*, pages 17–22, Seattle, February 2002. TMS Annual Meeting.

[9] G. R. Swanson and N. K. Arakere. Effect of crystal orientation on analysis of single-crystal, Nickel-based turbine blade superalloys. Technical Publication NASA/TP–2000-210074, NASA, Marshall Space Flight Center, February 2000.

[10] Masayuki Kamaya and Takayuki Kitamura. Stress intensity factors of microstructurally small crack. *International Journal of Fracture*, 0:113, 2003.

[11] J. R. Rice. A path independent integral and the approximate analysis of strain concentration by notches and cracks. *Journal of Applied Mechanics*, 35:379–386, 1968.

[12] H. A. Sosa and J. W. Eischen. Computation of stress intensity factors for plate bending via a path-independent integral. *Engineering Fracture Mechanics*, 25(4):451–462, 1986.

[13] D. M. Parks. A stiffness derivative finite element technique for the determination of crack tip stress intensity factors. *International Journal of Fracture*, 10(4), 1974.

[14] H. Ishikava. A finite element analysis of stress intensity factors for combined tensile and shear loading by only a virtual crack extension. *International Journal of Fracture*, 16:243–246, 1980.

[15] I. S. Raju. Calculation of strain-energy release rates with higher order and singular finite finite elements. *Engineering Fracture Mechanics*, 28(3):251–274, 1987.

[16] C. Atkinson, R. E. Smelser, and J. Sanchez. Combined mode fracture via the cracked Brazilian disk test. *International Journal of Fracture*, 18(4):279–291, 1982.

[17] H. Awaji and S. Sato. Combined mode fracture toughness measurement by the disk test. *Journal of Engineering Materials and Technology*, 100:175–182, 1978.

[18] R. K. L. Su and H. Y. Sun. Numerical solutions of two-dimensional anisotropic crack problems. *International Journal of Solids and Structures*, 40:46154635, 2003.

[19] R. K. L. Su and H. Y. Sun. A brief note on elastic T-stress for centred crack in anisotropic plate. *International Journal of Fracture*, 131:53–58, 2005.

[20] Chyanbin Hwu and Y.C. Liang. Evaluation of stress concentration factors and stress intensity factors from remote boundary data. *International Journal of Solids and Structures*, 37:5957–5972, 2000.

[21] M. Denda and M. E. Marante. Mixed mode BEM analysis of multiple curvilinear cracks in the general anisotropic solids by the crack tip singular element. *International Journal of Solids and Structures*, 41:1473–1489, 2004.

[22] G. Heppler and J. S. Hansen. Mixed mode fracture analysis of rectilinear anisotropic plates by high order finite elements. *International Journal for Numerical Methods in Engineering*, 17:445–464, 1981.

[23] H. Mews and G. Kuhn. An effective numerical stress intensity factor calculation with no crack discretization. *International Journal of Fracture*, 38:61–76, 1988.

[24] C. F. Shih, H. G. DeLorenzi, and M. D. German. Crack extension modeling with singular quadratic isoparametric elements. *International Journal of Fracture*, 12(3):647–650, 1976.

[25] Haiying Huang and George A Kardomateas. Stress intensity factors for a mixed mode center crack in an anisotropic strip. *International Journal of Fracture*, 108:367–381, 2001.

[26] H. Tada, P. C. Paris, and G. R. Irwin. The stress analysis of cracks handbook. Handbook, Paris Productions Inc., St. Louis, 1985.

[27] Yu-Zhou Sun, Shu-Shen Yang, and Yin-Bang Wang. A new formulation of boundary element method for cracked anisotropic bodies under anti-plane shear. *Comput. Methods Appl. Mech. Engrg.*, 192:2633–2648, 2003.

[28] G. C. Sih, P. C. Paris, and G. R. Irwin. On cracks in rectilinearly anisotropic bodies. *International Journal of Fracture Mechanics*, 1:189–203, March 1965.

[29] A.R. Ingraffea and C. Manu. Stress-intensity factor computation in three dimensions with quarter-point elements. *International Journal for Numerical Methods in Engineering*, 15:1427–1445, 1980.

[30] R. S. Barsoum. On the use of isoparametric finite elements in linear fracture mechanics. *International Journal for Numerical Methods in Engineering*, 10:25–37, 1976.

[31] V. E. Saouma and E. S. Sikiotis. Stress intensity factors in anisotropic bodies using singular isoparametric elements. *Engineering Fracture Mechanics*, 25(1):115–121, 1986.

[32] G. Dhondt. 3-D mixed mode K-calculations with the interaction integral method and the quarter point element stress method. *Communications in Numerical Methods in Engineering*, 17:303–307, 2001.

[33] G. Dhondt. Mixed-mode K-calculations in anisotropic materials. *Engineering Fracture Mechanics*, 69:909–922, 2002.

[34] J. Tweed, G. Melrose, and G. Kerr. Stress intensification due to an edge crack in an anisotropic elastic solid. *International Journal of Fracture*, 106:47–56, 2000.

[35] Ernian Pan and F. G. Yuan. Boundary element analysis of three-dimensional cracks in anisotropic solids. *International Journal for Numerical Methods in Engineering*, 48:211–237, 2000.

[36] M. Denda. Mixed mode I, II and III analysis of multiple cracks in plane anisotropic solids by the BEM: a dislocation and point force approach. *Engineering Analysis with Boundary Elements*, 25:267–278, 2001.

[37] R. John, Daniel P. Deluca, T. Nicholas, and J. Porter. Near threshold crack growth behavior of a single crystal Ni-base superalloy subjected to mixed mode loading. *Mixed-Mode Crack Behavior, American Society for Testing and Materials*, pages 312–328, November 1999.

[38] A. R. Ingraffea. On discrete fracture propagation in rock loaded in compression. In A. R. Luxmoore and D. R. J. Owen, editors, *Proceedings of Numerical Methods and Engineering in Fracture Mechanics*, pages 235–248, 1978.

[39] Daniel P. Deluca. Private Communication.

[40] J. M. Bloom. An evaluation of a new crack tip element - the distorted 8-node isoparametric element. *International Journal of Fracture*, 11:705–707, 1975.

[41] P. P. Lynn and A.R. Ingraffea. Transition elements to be used with quarter-point crack-tip elements. *International Journal for Numerical Methods in Engineering*, 12(6):1031–1036, 1978.

[42] S. Tarasovs. Numerical evaluation of quarter point crack tip singular element. *Tenth Nordic Seminar on Computational Mechanics*, 1997.

[43] R. I. Stephens, A. Fatemi, R. R. Stephens, and H. O. Fuchs. *Metal Fatigue in Engineering*. John Wiley & Sons Inc., New York, 2nd edition, 2001.

[44] S. Pearson. Initiation of fatigue cracks in commercial aluminum alloys and the subsequent propagation of very short cracks. *Engineering Fracture Mechanics*, 7:235–247, 1975.

[45] W. L. Morris. The noncontinuum crack tip deformation behavior of surface microcracks. *Metallurgical & Materials Transactions A*, 11:1117–1123, 1980.

[46] J. Lankford. The growth of small fatigue cracks in 7075-T6 aluminum. *Fatigue & Fracture of Engineering Materials & Structure*, pages 233–248, 1982.

[47] P. Newman and C. J. Beevers. Growth of short fatigue cracks in high strength Ni-base superalloys. In R. O. Ritchie and J. Lankford, editors, *Small Fatigue Cracks*, pages 97–116, Santa Barbara, California, January 1986. The American Institute of Mining, Metallurgical, and Petroleum Engineers.

[48] J. Telesman, D. N. Fisher, and D. Holka. Variables controlling fatigue crack growth of short cracks. In *Proc. Int. Conf. on Fatigue Corrosion Cracking Fracture Mechanics and Failure Analysis*, pages 53–69, Salt Lake City, 1986.

[49] M. Gell and G. R. Liverant. The characteristics of stage I fatigue fracture in a highstrength nickel alloy. *Acta Metallurgica*, 16(4):553–561, April 1968.

[50] M. Gell and G. R. Liverant. The fatigue of the nickel-base superalloy, MAR-M200, in single crystal and columnar-grained forms at room temperature. *Trans. AIME*, 242:1869–1879, September 1968.

[51] D. J. Duquette, M. Gell, and J. W. Piteo. A fractographic study of stage I fatigue cracking in a nickel-base superalloy single crystal. *Metallurgical Transactions*, 1:3107–3115, November 1970.

[52] O. Y. Chen. *Crystallographic fatigue crack propagation in single crystal nickel-base superalloy*. Phd dissertation, University of Connecticut, 1985.

[53] K. S. Chan, J. E. Hack, and G. R. Liverant. Fatigue crack growth in MAR-M200 single crystals. *Metallurgical & Materials Transactions A*, 18A:581–591, 1987.

[54] M. Nageswararao and V. Gerold. Fatigue crack propagation in stage I in an Aluminum-Zinc-Magnesium alloy: General characteristics. *Metallurgical & Materials Transactions A*, 7A:1847–1855, December 1976.

[55] Jr. A. J. McEvily and R. G. Boettner. On fatigue crack propagation in F.C.C. metals. *Acta Metallurgica*, 11(7):725–743, July 1963.

[56] J. Telesman and L. Ghosn. The unusual near-threshold FCG behavior of a single crystal superalloy and the resolved shear stress as the crack driving force. *Engineering Fracture Mechanics*, 34(5/6):1183–1196, 1989.

[57] Q. Chen and H. W. Liu. Resolved shear stress intensity coefficient and fatigue crack growth in large crystals. Contractor Report CR-182137, NASA, Syracuse University, June 1988.

[58] M. Peach and J. S. Koehler. The forces exerted on dislocations and the stress fields produced by them. *Physical Review*, 80(3):436–439, November 1950.

[59] S. Suresh. *Fatigue of Materials*. Cambridge University Press, 2nd edition, 1998.

BIOGRAPHICAL SKETCH

Srikant Ranjan was born in Daltongunj town in Bihar, India, in 1977. Always a topper during his schooling, he actively participated and bagged several accolades at various levels of extracurricular activities (elocution, essay writing, science exhibition, quiz competition, drama competition etc.). After his schooling he joined the premier engineering institute of India, Indian Institute of Technology, Kharagpur (IIT-KGP) in 1995. There he actively participated in, and organized various sports and cultural events, and was Inter-IIT athletics captain in his final year. He was awarded IIT-Blue, a highest honor, given for outstanding performance in sports activities. He got his B. Tech (Honors) degree in 1999 in Manufacturing Science and Engineering and joined Mechanical Engineering Department at University of Florida in May, 2000, on a project, then funded by NASA, to pursue Master of Science. Under the tutelage of Dr. Nagaraj K. Arakere, he continued his master's program towards PhD and wishes to continue his research work for industrial applications.